DEPARTAMENTO DE ASTROFÍSICA

Universidad de La Laguna

Study of fullerene-based molecular nanostructures in planetary nebulae

Memoria que presenta
D. José Jairo Díaz Luis
para optar al grado de
Doctor en Ciencias Físicas.

Trabajo dirigido por el
Dr. Domingo Aníbal García Hernández
y co-dirigido por el
Dr. Arturo Manchado Torres.

INSTITUTO Đ ASTROFISICA Đ CANARIAS
junio de 2017

Examination date: September, 2017
Thesis supervisor: Dr. Domingo Aníbal García Hernández
Thesis co-supervisor: Dr. Arturo Manchado Torres

A mi abuela,
a mi madre,
a mi hermano

Agradecimientos

"Demos gracias a los hombres y a las mujeres que nos hacen felices, ellos son los encantadores jardineros que hacen florecer a nuestros espíritus"

Will Rogers

Siempre nos ha costado mucho dar nuestros agradecimientos a las personas que han contribuido de alguna forma en nuestro ser y nos han dado tanto a lo largo de nuestras vidas. Es por esta razón por la que me siento inspirado y con unas ganas terribles de dar un salto en el tiempo para encontrarme con ellas. Y mira que es difícil reunir a tantas personas en una hoja de papel, pero la ocasión lo requiere y mi agradecimiento también.

Todo comenzó al llegar allí, a aquella institución extraña a la que debo tanto. Con sus jardines verdes y florecidos, el Instituto de Astrofísica de Canarias me daba la mejor de sus bienvenidas y abría sus puertas para comenzar el ansiado viaje. Allí me encontré con Aníbal, el director de mi viaje por esos andares. Sin él todo hubiese sido muy diferente. No solo por su apoyo incondicional, sino por llevar a cabo un trabajo magnífico y profesional digno de admiración. No había problema alguno que él no supiese resolver. Siempre había una respuesta, negativa o positiva, pero era una respuesta. Poco después conocí a Arturo, mi segundo director. A su lado, pasé largas tardes intentando resolver diferentes problemas de nuestro campo de estudio, que aunque a veces nos dieran un horrible dolor de cabeza, terminaban siendo de lo más ameno. Nuestros viajes a Hong Kong o Pekín fueron muy divertidos, sobre todo los pequeños paseos en carrito por la antigua ciudad de Xi'an. No puedo olvidarme tampoco de Kameswara Rao, con su ayuda en la búsqueda de Bandas Difusas en Nebulosas

Planetarias, de Franco Cataldo, que nos ha prestado su conocimiento sobre la química orgánica para su uso en nuestro campo, y de Omaira González Martín, que nos ha ayudado en la reducción de imágenes de CanariCam. Muchas gracias.

Este viaje no hubiese tenido ningún sentido sin apoyos incondicionales como son los de nuestra familia. A mi abuela, aquella mujer fuerte tanto física como mentalmente que ha sabido escucharme de una forma diferente al resto. Su conocimiento sobre la vida y su forma de hablar son únicas. Una cosa es escribirlo y otra muy diferente es sentirlo en carne viva. Una conexión muy particular que es digna de mención y, por supuesto, de agradecer. A mi madre, aquella cocinera del colegio que trabaja día tras día por el bienestar de los niños y que conoce bastante bien lo necesario que es el apoyo a los tuyos para llegar a conseguir diferentes metas en la vida. No hay viaje en la vida que no vaya acompañado de una madre. Y a mi hermano, que aunque todavía le queda un largo camino por recorrer, puede hacerte sacar una sonrisa en tus peores momentos.

Este viaje, tan lindo y a la vez tedioso, requiere la compañía de otras personitas que vamos escogiendo en el camino. Por ejemplo, Marina y Fran, a los que encontré por casualidad en los distintos ciclos que realizamos en nuestro proceso formativo. Una simple llamada o un WhatsApp son suficientes para escucharlos y tenerlos aquí. Del mismo modo, encontré espangarrada entre las flores a mi Alicia, la de Wonderland. Siempre aparece en el momento justo, y lo mejor de todo, es que podría reconocerla en cualquier parte. Salvarme es su labor. Cristinita no podía faltar, siempre animándome desde lejos y apostando por mí incluso hasta en mis búsquedas más espantosas sobre nuestro camino y deber en la vida. Y de caminos va la cosa. Eso pensarían Fran y Carmita Rosa al cruzarse en mi vida de aquella forma tan especial y necesaria. Sin ellos quizá no hubiese podido ponerme a escribir hoy estas líneas. Son ese tipo de personas que ayuda sin pedir nada a cambio. Algo semejante ocurre con Carol, una muchacha de lo más extraño que siempre en las nubes suele estar. Me ha sabido escuchar y entender en momentos en los que nadie lo hacía. Es muy probable que Tomás me encontrase también algo decaído algunas mañanas al salir de casa con rumbo a la aventura. Sus limones anaranjados fueron un gran aliciente para continuar. De igual manera, aparecieron en mi vida Stefania (mi churri), Enrique y mi cuchura, quienes ayudaron a desconectar de la rutina con viajes extraordinarios a Las Palmas, Sevilla, Madrid, Roma y Granada. Siempre

estaré agradecido.

Quiero expresar también mi más sincero agradecimiento al que posiblemente será mi tribunal de tesis. A Jorge García Rojas, Pedro García Lario, Eva Villaver, Pablo Rodríguez Gil y César Esteban, muchas gracias a todos por vuestro interés en el proyecto.

Finalmente, debo agradecer a otras personas su grata compañía durante todo este viaje. Personas como Yolanda, Cristina, Raquel, Guaci, Guille, Jonay, Álex, Aarón, Alba, María, Luis, Melania, Rafa, Efζan, Denis, Rui, etc. Muchas gracias a todos. Es hora de ponerse el sombrero.

Resumen

El objetivo principal de esta tesis es desvelar algunas cuestiones relacionadas con la formación de moléculas complejas basadas en fullerenos, con el objetivo de resolver algunos problemas clave en Astrofísica. La inesperada detección de fullerenos y grafeno (posible C_{24}, un fragmento) en entornos circunestelares ricos en hidrógeno de estrellas evolucionadas, indica que estas moléculas complejas no son tan raras y plantea la idea de que otras formas de carbono, como son los fullerenos hidrogenados (fulleranes), cebollas de carbono y nanotubos de carbono, podrían ser comunes en el Universo, jugando un papel importante en muchos aspectos de la física y química interestelar/circunestelar. Exploramos este nuevo y fértil campo de la Astroquímica centrándonos en el estudio de estas moléculas orgánicas complejas en Nebulosas Planetarias (NPs) de nuestra galaxia.

En primer lugar, presentamos una búsqueda completa de bandas difusas interestelares (DIBs) y un análisis detallado de sus velocidades radiales en tres NPs (Tc 1, M 1-20 e IC 418) que contienen fullerenos. En particular, encontramos que algunos DIBs son inusualmente intensos en estas fuentes; por ejemplo, una banda de absorción inusualmente intensa en 4428 Å es una característica común en NPs con fullerenos. Un resultado interesante de esta tesis es la posible detección, por primera vez, de dos bandas difusas circunestelares (DCBs) en 4428 y 5780 Å en la envoltura circunestelar rica en fullerenos de la NP Tc 1.

Seguidamente, presentamos espectros VLT/ISAAC en la región espectral entre 2.9 y 4.1 μm para las NPs Tc 1 y M 1-20. Presentamos la no detección de las bandas infrarrojas más intensas de moléculas relacionadas con fullerenos

como son los fulleranes (como $C_{60}H_{36}$ y $C_{60}H_{18}$), en torno a $\sim$3.4-3.6 μm en ambas NPs. Esta no detección junto a la detección tentativa de fulleranes en la proto-NP IRAS 01005+7910, sugiere que los fulleranes podrían formarse en la corta fase de transición de proto-NP, pero son rápidamente destruidos por el campo de radiación UV de la estrella central.

Finalmente, presentamos imágenes de banda estrecha (en el infrarrojo medio) de GTC/CanariCam en la NP extensa IC 418. Estudiamos la distribución espacial relativa de compuestos fullerénicos (tipo C_{60}), aromáticos (tipo hidrocarburos policíclicos aromáticos, HPAs) y alifáticos (por ej., el compuesto orgánico aún no identificado responsable de la emisión ancha en 9-13 μm), con el objetivo de esclarecer el mecanismo de formación de fullerenos en ambientes circunestelares ricos en hidrógeno. La emisión residual de C_{60} obtenida al sustraer la emisión continua de polvo podría tener varias interpretaciones; la más interesante sugiere que otras moléculas basadas en fullerenos (por ej., fulleranes) podrían contribuir a la emisión observada en 17.4 μm.

Abstract

The main goal of this thesis is to unveil some questions related to the formation of complex fullerene-based molecules in space, with the aim of resolving some key problems in Astrophysics. The unexpected detections of fullerenes and graphene (possible C_{24}) in the H-rich circumstellar environments of evolved stars indicate that these complex molecules are not so rare and have raised the idea that other forms of carbon such as hydrogenated fullerenes (fulleranes), buckyonions, and carbon nanotubes may be widespread in the Universe, playing an important role in many aspects of circumstellar/interstellar Chemistry and Physics. We explore this new and fertile field of research by focusing our study on Galactic planetary nebulae (PNe).

First, we present a detailed diffuse interstellar band (DIB) radial velocity analysis and a complete search of diffuse bands towards three PNe (Tc 1, M 1-20, and IC 418) containing fullerenes. In particular, some DIBs are found to be unusually intense towards these sources; for example, an unusually strong 4428 Å absorption feature is a common characteristic of fullerene PNe. Interestingly, we report the first possible detection of two diffuse circumstellar bands (DCBs) at 4428 and 5780 Å in the fullerene-rich circumstellar environment around PN Tc 1.

Second, we present VLT/ISAAC spectra in the 2.9-4.1 μm spectral region for the PNe Tc 1 and M 1-20. We report the non-detection of the most intense infrared bands of fullerene-related molecules such as fulleranes (like $C_{60}H_{36}$ and $C_{60}H_{18}$), around $\sim$3.4-3.6 μm in both PNe. These non-detections, together with the tentative detection of fulleranes in the proto-PN IRAS 01005+7910, suggest that fulleranes may be formed in the short transition phase between AGB stars

and PNe, but they are quickly destroyed by the UV radiation field from the central star.

Finally, we present narrow-band mid-IR GTC/CanariCam images of the extended fullerene-containing PN IC 418. We study the relative spatial distribution of C_{60}- and PAH-like species as well as the 9-13 μm carrier, with the aim of getting some observational constraints to the formation process of fullerenes in H-rich circumstellar environments. The residual C_{60} emission seen when subtracting the dust continuum emission might have several interpretations; the most interesting being that other fullerene-based species (e.g., fulleranes) may contribute to the observed 17.4 μm emission.

Contents

1

Introduction

1.1 A brief history of organic chemistry

Carl Wilhelm Scheele in 1769 isolated the first organic compounds from living organisms and some methods to determine elemental composition were developed by Antoine Lavoisier in 1784. Subsequently, Gevela Jacob Berzelius was the first to use the term "organic chemistry" in 1806 for the study of compounds derived from biological sources. Scientists of that epoch believed that there was a special "vital force" in organic chemicals that directed their natural synthesis and did not exist in any inorganic materials. Fortunately, Friedrich Wöhler in 1828 synthesized the biological compound urea (a component of urine in many animals) by heating ammonium cyanate, what meant that the natural force was not required to produce organic compounds. Nowadays it is well known that organic chemicals get their diversity from the many different ways that carbon is bonded to other atoms and many new organic compounds have been synthesized in the laboratory. The atoms of carbon can also bond together in different ways, in the same physical state, known as allotropes. Among them, we can find diamond, graphite, amorphous carbon, fullerenes, or carbon nanotubes (cylindrical nanostructure). Thus, organic molecules, by definition, are those which are based on the element carbon, but may also contain other elements such as H, O, N, S, and P. Figure 1.1 shows some carbon allotropes present in space.

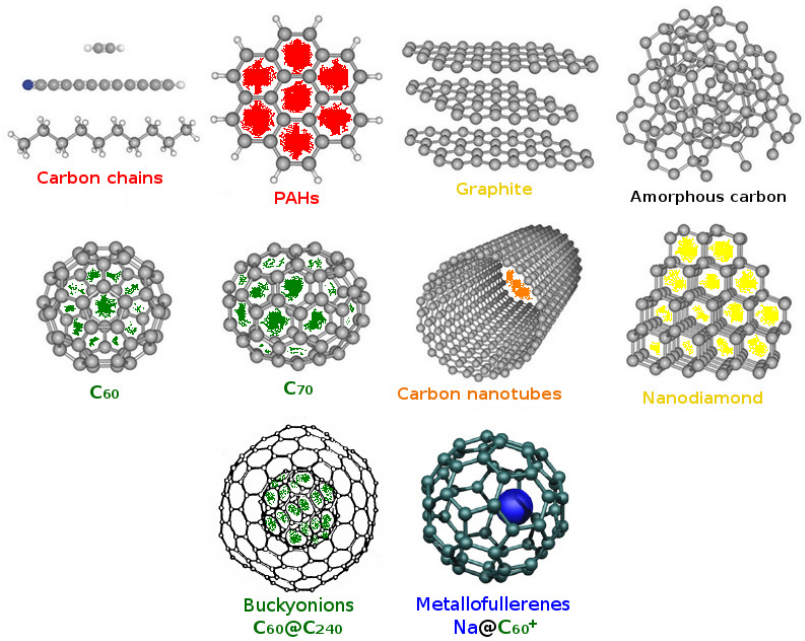

Figure 1.1: Carbon allotropes present in space (adapted from Ehrenfreund & Foing 2010, Iglesias Groth 2004, and Dunk et al. 2013). C_{60} and C_{70} fullerenes have been first detected in the planetary nebula Tc 1 (Cami et al. 2010). Nanodiamonds and graphite have been found in meteorites (Amari et al. 1990; Lewis et al. 1987). Amorphous carbon may be the main component of carbon in low-density interstellar regions (Bussoletti et al. 1987). Moreover, polyynes (carbon chains) and polycyclic aromatic hydrocarbons (PAHs) are supposed to be ubiquitous in space (Leger & Puget 1984; Turner 1971). Future observations and laboratory data may lead to the identification of other fullerene compounds, such as carbon nanotubes (Cataldo 2005), buckyonions (Iglesias Groth 2004), or metallofullerenes (Dunk et al. 2013).

Interestingly, the role of molecules in Astronomy (Astrochemistry) has become increasingly important in recent years. The first interstellar molecules

detected were cyanide (CN), methylidyne radical (CH), and methylidynium (CH^+) through their electronic transitions (McKellar 1940) and, up to now, approximately more than 200 gas-phase molecules have been detected in the interstellar medium (e.g., Kwok 2016). Complex organic matter is widely present in the Solar System, in the circumstellar environment of stars, in interstellar clouds, in the diffuse interstellar medium, and in distant galaxies (e.g., Kwok 2016). In fact, due to the extremely high sensitivities of modern millimeter (mm) and submm-wave telescopes and the large number of molecules present in the interstellar medium, we can detect some molecular lines in practically every spectral region of the mm/submm spectrum.

1.2 Fullerenes and molecular-related species in space

Fullerenes are highly resistant and stable tridimensional molecules formed exclusively by 60 or more carbon atoms. Fullerenes and fullerene-related molecules have attracted much attention since their discovery at laboratory (Kroto et al. 1985) due to their potential applications in technology research. In the astrophysical context, these complex molecules may explain certain unidentified astronomical features such as the so-called "UV bump" at 217 nm (e.g., Cataldo & Iglesias-Groth 2009) and the so-called diffuse interstellar bands (DIBs) that may be associated with large carbon-based molecules (e.g., García-Hernández & Díaz-Luis 2013). Fullerenes were found on Earth and on meteorites, but the presence of fullerenes in astrophysical environments has been a matter of debate until *Spitzer Space Telescope* observations provided the first evidence for the presence of C_{60} and C_{70} fullerenes - the largest and more complex molecules ever detected in space - in Planetary Nebulae (PNe; Cami et al. 2010; García-Hernández et al. 2010, 2011b), reflection nebulae (Sellgren et al. 2010), the two least H-deficient R Coronae Borealis stars (García-Hernández et al. 2011a) and a proto-PN (Zhang & Kwok 2011), among other astronomical sources. Figure 1.2 shows the *Spitzer* IRS spectrum of the planetary nebula (PN) Tc 1 between 5 and 23 μm. The spectrum is dominated by the prominent C_{60} bands at 7.0, 8.5, 17.4, and 18.9 μm, and other weaker features that are due to C_{70}. Cami et al. (2010) claimed that fullerenes flourish in the H-deficient and carbon-rich inner regions of Tc 1, in agreement with the original laboratory studies on the formation of fullerenes (de Vries et al. 1993; Kroto et al. 1985) that show that fullerenes at laboratory are efficiently produced under H-poor conditions. How-

ever, it was soon demonstrated that fullerenes are efficiently formed in H-rich circumstellar environments (García-Hernández et al. 2011a, 2010, 2011b). In particular, the C_{60} IR transitions are present in the spectra of DY Cen and V854 Cen, which are the two least H-deficient R Coronae Borealis (RCB) stars known. The other highly H-deficient RCB stars do not show fullerene features (see García-Hernández et al. 2011a for more details). Moreover, all known fullerene-containing PNe are H-rich and C_{60} only represents a very small percentage of the total carbon in these stars (see García-Hernández et al. 2010, 2011b for more details), though we cannot discard the formation of fullerenes in other H-poor astrophysical environments.

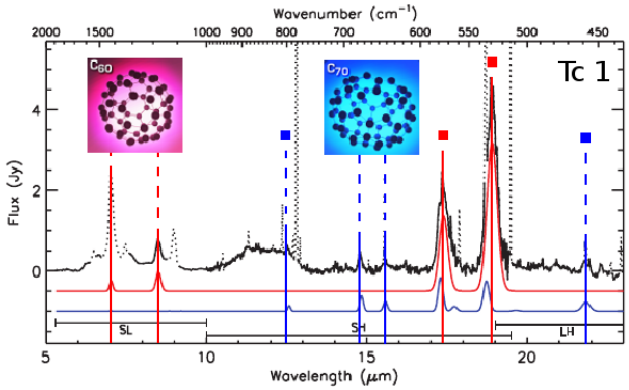

Figure 1.2: Continuum-subtracted *Spitzer* IRS spectrum of the PN Tc 1 between 5 and 23 μm (adapted from Cami et al. 2010). A cubic spline was fitted to spectral ranges devoid of features to determine the dust continuum. Red vertical lines mark the wavelengths of all infrared C_{60} bands; blue vertical lines denote those of the four strongest, isolated C_{70} bands. The red and blue curves are thermal emission models for all infrared active bands of C_{60} and C_{70} at temperatures of 330 and 180 K, respectively.

Interestingly, the first evidence of the possible detection of planar C_{24} (a piece of graphene) in some fullerene-containing sources has been reported by García-Hernández et al. (2011b). The 2010 Nobel Prize in Physics was awarded

to A. Geim and K. Novoselov, who synthesized graphene in the laboratory. Graphene has promising technological applications (Novoselov et al. 2004). The detection of fullerenes and graphene (possible C_{24}) around evolved stars (e.g., PNe) raises the idea that other forms of carbon such as hydrogenated fullerenes (fulleranes such as $C_{60}H_{36}$ and $C_{60}H_{18}$; see Chapter 3 for more details), bucky-onions (multishell fullerenes), carbon nanotubes, or metallofullerenes (a metal atom trapped inside a fullerene cage; see Figure 1.1), may be widespread in the Universe, playing an important role in many aspects of circumstellar/interstellar Chemistry and Physics.

Finally, we must also mention the polycyclic aromatic[1] hydrocarbons (PAHs), which are organic compounds (containing only carbon and hydrogen) that are composed of multiple aromatic rings. The broad and strong emission bands observed in the mid-IR spectra of different sources are commonly linked to PAHs (see Section 1.4 and Chapter 3 for more details; Allamandola et al. 1985; Leger & Puget 1984; Sellgren 1984). Moreover, these molecules exhibit a wide variety of spectral shapes and strengths (Peeters et al. 2002; van Diedenhoven et al. 2004), and may play an important role in the formation of fullerenes in space (see Chapter 4 for more details; Berné & Tielens 2012; García-Hernández et al. 2010).

1.3 Diffuse interstellar bands

The diffuse interstellar bands (DIBs) are absorption features that are observed in the spectra of astronomical objects in our galaxy and other galaxies (e.g., Cox et al. 2005; Cox 2015; Cox & Cordiner 2008). They have remained a mystery for astronomers since their discovery about ninety years ago (Heger 1922); they are one of the long-standing problems in the interstellar medium (ISM). Nowadays, more than 400 DIBs have been identified in the ISM (e.g., Hobbs et al. 2008; Geballe et al. 2011), mostly in the 4000-10000 Å spectral range, with different strengths, widths and shapes. Moreover, their strengths show a positive relationship with the observed extinction (Merrill & Wilson 1936), as well as to the neutral sodium column density (see Chapter 2 for more details; Herbig 1993). An illustrative example of very well known DIBs in the

[1]Aromatic hydrocarbons have aromatic ring system or benzene rings (6 carbon atoms joined in a ring with 1 hydrogen atom attached to each) in their structure.

~5760-5800 Å spectral region is displayed in Figure 1.3.

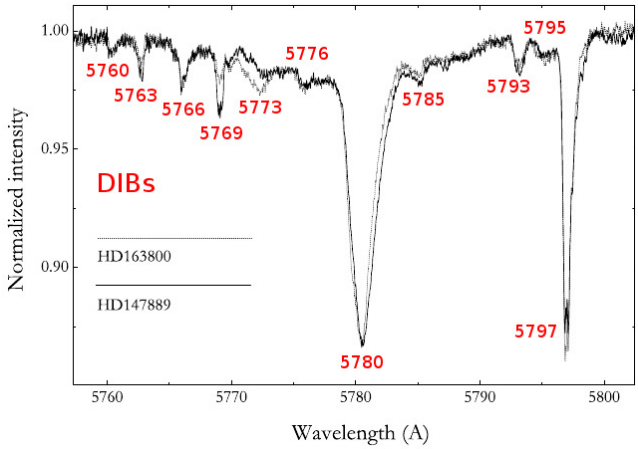

Figure 1.3: Profiles of some DIBs in HARPS spectra of HD 147889 and HD 163800 (adapted from Galazutdinov et al. 2008).

Astronomers believe that DIBs represent the largest reservoir of organic material in the galaxy (Snow 2014). PAHs (e.g., Salama et al. 1999), fullerenes (e.g., Foing & Ehrenfreund 1994; Herbig 2000; Iglesias-Groth 2007), and polyatomic organic molecules (e.g., Maier et al. 2011) are among the proposed DIB carriers. The identification of C_{60}^+ as the carrier (the only DIB carrier known to date) of the two DIBs at 9632.7 and 9577.5 Å has been recently confirmed by Campbell et al. (2015). This identification was based on measurements of the FWHM and relative intensities of these bands in the gas-phase laboratory spectra of C_{60}^+ at 6 K. It is clear that there is a direct fullerenes-DIB connection. In Figure 1.4, we show the gas-phase laboratory spectra of C_{60}^+, showing the two bands (marked with vertical blue lines) that confirm their identification. We note that Walker et al. (2015) have identified other three weaker DIBs as due to C_{60}^+, while similar laboratory experiments for C_{70}^+ (Campbell et al. 2016) show that its individual absorption bands are intrinsically too weak to be detected in astronomical spectra.

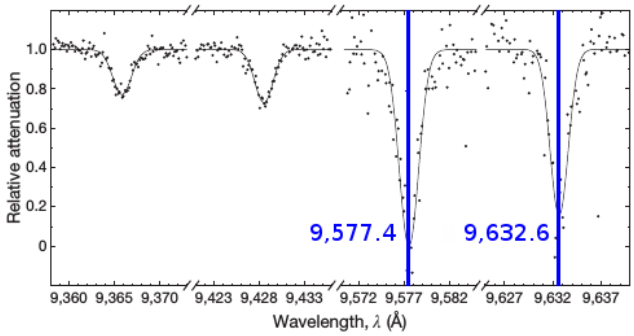

Figure 1.4: Gas-phase laboratory spectra of C_{60}^+ at 5.8 K (adapted from Campbell et al. 2015). The vertical blue lines are the corresponding central wavelengths of two reported DIBs.

On the other hand, the possible link between PAHs and DIBs was made by Crawford et al. (1985), Leger & D'Hendecourt (1985), and van der Zwet & Allamandola (1985). Apart from having (electronic) transitions in the UV, optical, and near-infrared, PAHs are also very resistant to UV radiation. Thus, the expected high abundance of PAHs in space, their optical absorption spectrum, and the presence of substructure in the DIB profiles, seem to give support for the PAH-DIB hypothesis (see, e.g., Cox 2011; Salama et al. 1999). However, a potential problem with the PAH-DIB hypothesis is the lack of interstellar bands in the UV part of the astronomical spectra (Snow & Destree 2011; Snow & McCall 2006), where strong PAH transitions are expected (see, e.g., Tielens 2008).

1.4 Unidentified infrared emission bands

Ubiquitous and yet unidentified infrared emission bands (UIRs at ∼3.3, 6.2, 7.7, 8.6, 11.3, and 12.7 μm) or aromatic infrared bands (AIBs), are detected in a wide range of interstellar, circumstellar, and extragalactic sources. These include (proto-) PNe, star formation regions, H II regions, reflection nebulae, novae, and the diffuse interstellar medium. Moreover, these bands may be accompanied by

aliphatic[2] bands at 3.4, 6.9, and 7.3 μm, and unassigned features at 15.8, 16.4, 17.4, 17.8, and 18.9 μm (Chiar et al. 2000; Jourdain de Muizon et al. 1990; Kwok et al. 1999; Sellgren et al. 2007; Sturm et al. 2000)[3], and the broad emission features at ∼6-9, 9-13, 15-20, and 25-35 μm. Figure 1.5 shows the astronomical UIR bands seen in the PN IRAS 21282+5050.

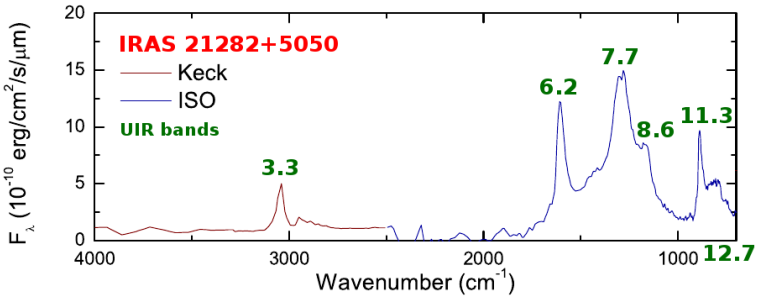

Figure 1.5: Astronomical spectrum of the PN IRAS 21282+5050 (adapted from Kwok 2013). The UIR bands are labeled by their wavelengths in green.

The UIRs, after being discovered by Gillett et al. (1973) in the 8-13 μm range, were proposed by Duley & Williams (1981) as originating from the vibrations of chemical functional groups attached to small carbon grains. Later, Sellgren (1984) suggested a model in which the near infrared continuum emission in reflection nebulae is due to non-equilibrium thermal emission from very small grains (size ∼10 Å), which are stochastically heated to high temperatures by the absorption of UV photons. Leger & Puget (1984) and Allamandola et al. (1985) independently identified the infrared emission features with the vibrational relaxation of PAH molecules excited by UV photon absorption. Thus, PAH molecules have been widely accepted by astronomers as the carriers of the UIRs and "free-flying[4]" gas-phase PAHs have been assumed to be a major reser-

[2]Aliphatic hydrocarbons are those which do not contain ring system or benzene rings in their structure.

[3]It is now known that the 17.4 and 18.9 μm features are due to fullerenes (Cami et al. 2010; García-Hernández et al. 2010).

[4]Free-flying molecules are not influenced by any of their neighbor molecules.

voir for carbon in the Universe. However, no single gas-phase PAH molecule has been identified in space and the exact molecular form of the aromatic (PAH-like) component has not been successfully confirmed (see, e.g., Bauschlicher et al. 2010; Boersma et al. 2014; Maltseva et al. 2015; Sadjadi et al. 2015).

More recently, Duley & Williams (2011) propose a model in which the feature at 3.3 μm can be explained by the heating of hydrogenated amorphous carbon (HAC) dust via the release of stored chemical energy. This alternative to the PAH hypothesis involves a solid material with a mix of aliphatic and aromatic structures commonly found in hydrogenated amorphous carbon grains (HACs) or similar carbonaceous materials (e.g., coal, petroleum fractions, etc.). Interestingly, detection of additional emission at 3.4 μm, characteristic of aliphatic hydrocarbons (sp^3-bonded carbon), in proto-PNe (Kwok et al. 2001) and in the diffuse ISM, demonstrates that the PAH-like component (aromatic) is mixed with aliphatic compounds. The broad emission features at ∼6-9, 9-13, 15-20, and 25-35 μm, could also be produced by a carbonaceous mixture of aromatic and aliphatic structures (García-Hernández et al. 2010, 2012b; Kwok & Zhang 2011).

Kwok & Zhang (2011) propose a more general model (the MAON model) to explain the aliphatic-like bands and broad "plateaus" observed in different types of astronomical objects. The mixed aromatic/aliphatic organic nanoparticles (MAON) model incorporates an aliphatic component to aromatic molecules like PAHs (Kwok & Zhang 2011). Figure 1.6 shows the chemical structure of a MAON. These 3-D particles are amorphous solids with no fixed structure, containing rings, chains, and impurities. This idea is some kind connected with the detection of C_{60} in the PN Tc 1 and the possible link between C_{60} and the UIR phenomenon. Tc 1 has no UIR features and shows the broad 6-9 and 9-13 μm features. However, the PPN IRAS 01005+7910 shows C_{60} features, UIR bands, and the 6-9, 9-13, and 25-35 μm unidentified emission features (Zhang et al. 2010). This coincidence between C_{60} and the 6-9 and 9-13 μm features (e.g., García-Hernández et al. 2010; Otsuka et al. 2014; Zhang & Kwok 2013) may suggest that this kind of material (MAON or HAC-like) could be a precursor of fullerenes (e.g., Bernard-Salas et al. 2012; García-Hernández et al. 2010, 2012b). In Figure 1.7, we can see the infrared bands of C_{60} and C_{70}, and the 6-9, 9-13, and 25-35 μm emission plateau features in the *Spitzer* IRS spectrum of the PN Tc 1.

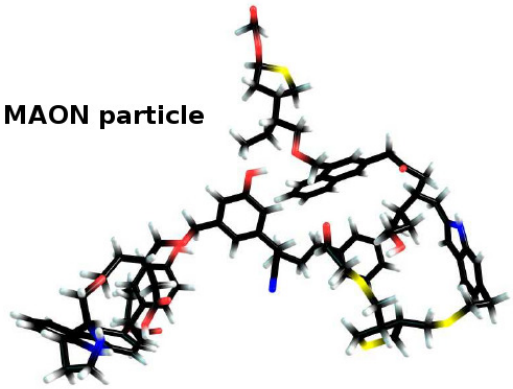

Figure 1.6: 3-D ilustration of a possible mixed aromatic-aliphatic organic nanoparticle (MAON) (adapted from Kwok 2013). Carbon atoms (101) are represented in black, hydrogen (120) in light grey, sulphur (4) in yellow, oxygen (14) in red, and nitrogen (4) in blue.

1.5 Planetary nebulae as an astrochemistry laboratory

The first PN was discovered by Charles Messier in 1764 and the name planetary nebula was given by William Herschel, since their appearances seemed like the greenish disk of a planet. With better telescope spatial resolution, it has been seen that PNe have definite structures and are often associated with a central star. This distinction was verified by doing spectroscopy some years later, when William Huggins took the first spectrum of a PN (NGC 6543) in 1864. By that time, it was thought that PNe were very young stars because of their high temperatures. However, Curtis (1918) found that PNe are more similar to late-type stars.

The first study that involved a theoretical understanding of the origin of PNe was made by Shklovskii (1956), who suggested that PNe are progenitors of white dwarfs (WDs) and descendants of red giants. Shklovsky recognized that these stars must evolve rapidly. Moreover, Abell & Goldreich (1966) supported this idea by using the expansion velocities of PNe and the escape velocities

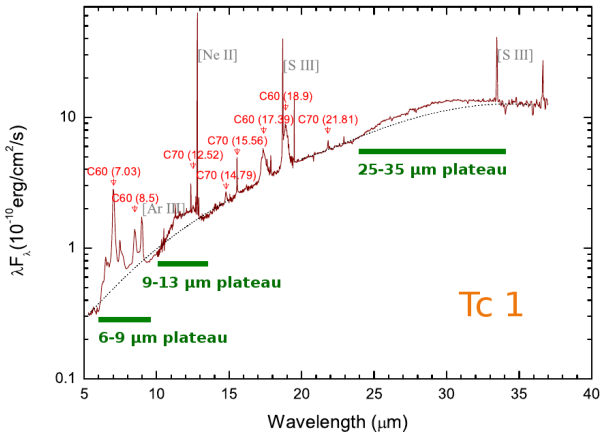

Figure 1.7: The *Spitzer* IRS spectrum of the PN Tc 1 shows C_{60} and C_{70} emission bands (in red) and the 6-9, 9-13, and 25-35 μm emission plateau features (in green) (adapted from Kwok 2013).

of red giants to declare that PNe are the ejected atmospheres of red giants. They suggested that practically all low-mass stars ($\sim$1-8 $M_\odot$) will go through the PN stage, what established the importance of PNe in the scheme of stellar evolution. In Figure 1.8, we can see the evolution of a star from the zero age main sequence (ZAMS) to the white dwarf stage. At present, we know that PNe are an evolutionary phase between the asymptotic giant branch (AGB; see, e.g., Herwig 2005 for a review) and the white dwarf phase. After the AGB phase, the star ejects most of its envelope through a dense and slow stellar wind. Subsequently, the stellar core photoionizes the circumstellar envelope, forming a PN.

Interestingly, the aromatic (C-rich) and crystalline[5] (O-rich) compounds are synthesized during the short transition phase between AGB stars and PNe, so-called the post-AGB or proto-PNe phase (García-Lario & Perea Calderón 2003; Kwok 2004), which lasts between $\sim 10^2$ and 10^4 years. This short transition

[5] A crystalline structure is any structure of atoms that are held together in a specific order.

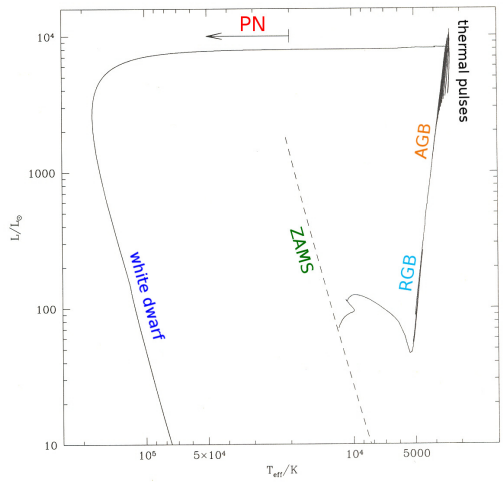

Figure 1.8: The evolution of a low-mass (∼1-8 $M_\odot$) star on the H-R diagram beginning from the zero age main sequence (ZAMS), through the red giant branch (RGB) and AGB to PN and ending as a white dwarf (adapted from Kwok 2000).

phase provides us with crucial information about the formation pathways of complex organic (and inorganic) molecules and solid-state compounds. Complex fullerene molecules are mostly detected in young PNe (e.g., García-Hernández et al. 2012b) and the early PN stages provide the ideal laboratory in space to study such complex organic species. Also, the PN stage is an ideal environment for the study of the interaction between radiation and matter. The energy is derived from the central star and is absorbed and processed by the nebula, which contains ionized, atomic, molecular, and solid-state matter. Figure 1.9 shows the Spirograph Nebula IC 418 as observed by the Hubble Space Telescope.

Here, we focus our study on some Galactic PNe that contain fullerenes. In order to do this, we make use of laboratory spectra of several fullerene-related compounds and compare them with astronomical data. This thesis is a first step to open up a new field of interdisciplinary research, crossing the

boundaries between astronomers, chemists, and physicists, to unveil the role of fullerene structures in circumstellar/interstellar environments.

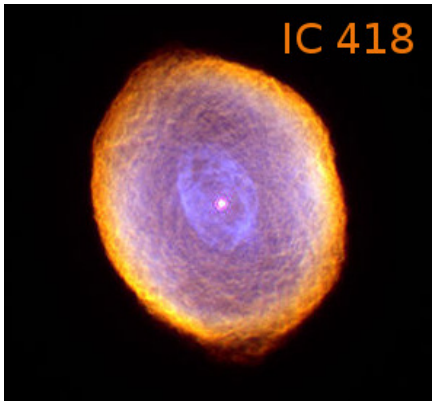

Figure 1.9: The spirograph Nebula IC 418 taken by the Hubble Space Telescope. The central star is surrounded by an extended circumstellar envelope. Red shows emission from ionized nitrogen, green shows emission from hydrogen, and blue traces the emission from ionized oxygen.

1.6 Outline of the thesis

The thesis is mainly composed by three articles, two of them already published and the third one submitted for publication. The manuscript is organized as follows:

- In Chapter 2, we present a detailed DIB radial velocity analysis and a complete search of diffuse bands (both interstellar and circumstellar) towards three PNe (Tc 1, M 1-20, and IC 418) containing fullerenes.
- Chapter 3 describes our search of fullerene-related molecules such as hydrogenated fullerenes (fulleranes like $C_{60}H_{36}$ and $C_{60}H_{18}$) in the 3-5 μm spectral range in the C_{60}-rich PNe Tc 1 and M 1-20.

- In Chapter 4, we present narrow-band mid-IR GTC/CanariCam images of the extended fullerene-containing PN IC 418. We study the relative spatial distribution of C_{60}- and PAH-like species as well as the 9-13 μm carrier, with the aim of getting some observational constraints to the formation process of fullerenes in H-rich circumstellar environments.
- Finally, we give a summary of the conclusions reached in this thesis in Chapter 5 and list allusions for future work in Chapter 6.

2

Diffuse bands in fullerene planetary nebulae: evidence of diffuse circumstellar bands

Based on

J. J. Díaz-Luis et al. 2015, A&A, 573, A97

ABSTRACT - Large fullerenes and fullerene-based molecules have been proposed as carriers of diffuse interstellar bands (DIBs). The recent detection of the most common fullerenes (C_{60} and C_{70}) around some planetary nebulae (PNe) now enable us to study the DIBs towards fullerene-rich space environments. We search DIBs in the optical spectra towards three fullerene-containing PNe (Tc 1, M 1-20, and IC 418). Special attention is given to DIBs which are found to be unusually intense towards these fullerene sources. In particular, an unusually strong 4428 Å absorption feature is a common charateristic of fullerene PNe. Similar to Tc 1, the strongest optical bands of neutral C_{60} are not detected towards IC 418. Our high-quality (S/N > 300) spectra for PN Tc 1, together with its large radial velocity, permit us to search for the presence of diffuse bands of circumstellar origin, which we refer to as diffuse circumstellar bands (DCBs). We report the first tentative detection of two DCBs at 4428 and 5780 Å in the fullerene-rich circumstellar environment around the PN Tc 1. Laboratory and theoretical studies of fullerenes in their multifarious manifestations (carbon onions, fullerene clusters, or even complex species formed by fullerenes and other molecules like PAHs or metals) may help solve the mystery of some of the diffuse band carriers.

2.1 Introduction

Identification of the carriers of the diffuse interstellar bands (DIBs) has been very elusive since they were first discovered by Heger (1922), who first noted their stationary nature as observed towards a spectroscopic binary, indicating that their origin was not stellar but rather interstellar. Different complex carbon-based molecules - e.g., carbon chains, polycyclic aromatic hydrocarbons (PAHs), and fullerenes - have been proposed as DIB's carriers (see, e.g., Cox & Cami 2014 for a review).

At present, very little is known about the presence of the DIB carriers in other astrophysical environments (e.g., Cox 2011). If the DIBs arise from large gas phase molecules, such as PAHs and fullerenes, then they are also expected to be present in other carbon-rich space environments like circumstellar shells around stars. Diffuse circumstellar bands (DCBs) in absorption have been unsuccessfully studied for more than 40 years (Seab 1995)[1]. DCBs are absent in the dusty circumstellar envelopes (with or without PAH-like features) of AGB/post-AGB stars, as well as in the atmospheres of cool stars and Herbig Ae/Be stars (Cox 2011; Luna et al. 2008; Seab 1995). Thus, the conventional wisdom is that there are no diffuse bands in circumstellar environments. The unambiguous detection of DCBs would have a strong impact on diffuse bands theories; for example, they can be compared to the presence of the proposed diffuse band carriers mentioned above. The main difficulty to detect DCBs is to distinguish them from the DIBs (Cox 2011; Seab 1995). This distinction can only be made by measuring the radial velocities of the circumstellar and interstellar components. Here we search for the possible presence of DCBs in a selected sample of three fullerene-containing PNe.

In García-Hernández & Díaz-Luis (2013), we presented some of the new results for DIBs towards the fullerene PNe Tc 1 and M 1-20, and the very broad 4428 Å DIB was found to be unusually intense (based on the measured equivalent widths) towards both Tc 1 and M 1-20. The speculation was offered that the unusually strong 4428 Å DIB towards fullerene PNe may be related to the presence of larger fullerenes and buckyonions in their circumstellar envelopes.

[1]We note that some diffuse bands in emission have been previously seen in a proto-PN (the Red Rectangle) and in the R Coronae Borealis star V854 Cen (see, e.g., Kameswara-Rao & Lambert 1993; Scarrott et al. 1992).

However, García-Hernández & Díaz-Luis (2013) did not carry out any radial velocity analysis, something that is mandatory for confirming a circumstellar origin.

In this chapter we present a detailed DIB radial velocity analysis and a complete search of diffuse bands towards three PNe (Tc 1, M 1-20, and IC 418) containing fullerenes and accompanied (or not) by PAH molecules. A summary of the optical spectroscopic observations is presented in Section 2.2. Section 2.3 gives a complete analysis of the DIBs towards fullerene PNe, including the normal DIBs most commonly found in the ISM and a few unusually strong DIBs. Section 2.4 presents our search for DCBs in fullerene PNe and their detection in PN Tc 1. Sections 2.5 and 2.6 discuss the non-detection of the electronic C_{60} transitions in the IC 418 optical spectrum and the possible connection between fullerenes and diffuse bands, respectively. The conclusions are given in Section 2.7.

2.2 Optical spectroscopic observations

We acquired optical spectra of the fullerene PNe Tc 1 (B=11.1, E(B-V)=0.23; Williams et al. 2008), M 1-20 (B=13.7, E(B-V)=0.80; Wang & Liu 2007), and IC 418 (B=9.8, E(B-V)=0.23; Pottasch et al. 2004). The detection of fullerene-like features in the IC 418 *Spitzer* spectrum has recently been reported by Morisset et al. (2012). Tc 1 displays a fullerene-dominated spectrum with no clear signs of PAHs, while M 1-20 and IC 418 also show weak PAH-like features (see, e.g., García-Hernández et al. 2010; Meixner et al. 1996). All PNe in our sample also show unidentified broad dust emission features centred at $\sim$9$-$13 and 25$-$35 μm (see, e.g., García-Hernández et al. 2012b). The effective temperature of the central star of PN IC 418 (T_{eff}=36700 K; Morisset & Georgiev 2009) is very similar to that of the central star of Tc 1 (T_{eff}=34060 K; Otsuka et al. 2014), while M 1-20 (T_{eff}=45880 K; Otsuka et al. 2014) is among the fullerene PNe with the hottest central stars. Our sample PNe display round (Tc 1) or elliptical (M 1-20, IC 418) morphologies (see Figure 1 in Otsuka et al. 2014).

The observations of Tc 1 and M 1-20 were carried out at the ESO VLT (Paranal, Chile) with the ultraviolet and visual echelle spectrograph (UVES; D'Odorico et al. 2000) in service mode between May and September 2011 (see García-Hernández & Díaz-Luis 2013 for more observational details). We used

the 2.4" slit centred at the central stars of the two PNe (see Figure 1 in Otsuka et al. 2014) and following the parallactic angle. This configuration should give a resolving power of ∼15000 from ∼3300 to 9400 Å. However, from the O_2 telluric lines at ∼6970 Å, we measure a much higher resolving power of about 23000. The signal-to-noise ratio (S/N) (in the final combined spectrum) in Tc 1 is very high (∼300 at 4000 Å and >300 at longer wavelengths), which permitted us to search for the expected electronic transitions of neutral C_{60} and both strong and weak DIBs (García-Hernández & Díaz-Luis 2013). In M 1-20, however, the final S/N (∼20 at 4000 Å and >30 at wavelengths longer than 6000 Å) was not high enough to search the relatively broad (and weak) C_{60} features around 4000 Å or the weakest DIBs.

The optical spectroscopic observations of IC 418 (the brightest fullerene PN in our sample) were carried out at the Nordic Optical Telescope (NOT; Roque de los Muchachos, La Palma) in March 2013 with the FIES spectrograph (under service time). The optical spectra were taken in the wavelength range ∼3600-7200 Å by using the FIES low-resolution mode (3630-7170 Å; orders 157-80) with the 2.5" fibre (centred at the IC 418 central star), which translates into a resolving power of ∼25,000. Three exposures of 1200 s each were obtained in order to reach a S/N of ∼60 at 4000 Å (and in excess of ∼150 at wavelengths longer than 5000 Å) in the final combined IC 418 spectrum.

As comparison stars, for Tc 1 and M 1-20 we selected the nearby B-type stars HR 6334 (B=5.1; E(B-V)=0.42; Wegner 2003) and HR 6716 (B=5.7; E(B-V)=0.22; Wegner 2003), respectively, while HR 1890 (B=6.4; E(B-V)=0.08; Wegner 2003) was selected for IC 418. These comparison stars were observed on the same dates as the PNe and with the same VLT/UVES and FIES set-ups. Two exposures of 300 s were enough to obtain a final S/N in excess of ∼300 in the final combined spectra of the comparison stars. The observed UVES and FIES spectra - processed with the UVES data reduction pipeline (Ballester et al. 2000) and with the FIES reduction software (FIEStool[2]), respectively - were corrected for heliocentric motion and combined, and the stellar continuum

[2]See http://www.not.iac.es/instruments/fies/fiestool/FIEStool-manual-1.0.pdf

for the three PNe was fitted by using standard astronomical tasks in IRAF[3]. We had to take into consideration the fact that we may sometimes find artifacts in the merged spectrum. These artifacts are due to bleeding from adjacent orders owing to bright emission lines or to internal reflexions in the optics of the instrument. The net effect is that as they appear as emissions in the inter-order regions, they are transformed into fake absorptions in the extracted spectrum when correcting from background scattered light in the reduction procedure. We have carefully checked all our spectra to be sure that these artifacts are not affecting our DIB detections. Moreover, FIEStool merges the individual spectral orders into one long 1-dimensional spectrum and special attention is needed in the regions where consecutive spectral orders overlap in wavelength and have been averaged. Table 2.1 lists some observational parameters, such as galactic coordinates, colour excess, and radial velocity for the three fullerene PNe in our sample and their corresponding comparison stars.

Table 2.1: Observational parameters of fullerene PNe and their comparison stars.

Object	l	b	E(B-V)	V_r	Ref [a]	Comparison star	l	b	E(B-V)	V_r	Ref [a]
Tc 1	345.2375	−08.8350	0.23	−94.0	1, 2, 7	HR 6334	350.829	4.285	0.42	7.0	6, 9
M 1-20	6.187	8.362	0.80	75.0	3, 4, 7	HR 6716	7.162	−0.034	0.22	4.2	6, 10
IC 418	215.212	−24.284	0.23	62.0	4, 5, 8	HR 1890	208.177	−18.957	0.08	29.5	6, 10
HD 204827 [b]	99.167	5.552	1.06	20.0	6, 11						

[a] References. (1) Williams et al. (2008); (2) Frew et al. (2013) ; (3) Wang & Liu (2007); (4) McNabb et al. (2013); (5) Pottasch et al. (2004); (6) Wegner (2003); (7) Beaulieu et al. (1999); (8) Wilson (1953); (9) Kharchenko et al. (2007); (10) Pourbaix et al. (2004); (11) Petrie & Pearce (1961).
[b] The Hobbs et al. (2008) reddened star used as a reference for DIBs (see Section 2.3).

2.3 DIBs towards PNe with fullerenes

We followed the list of DIBs measured in the high-S/N HD 204287 spectrum (Hobbs et al. 2008) to search for them in the VLT/UVES spectra of Tc 1 and M 1-20, as well as in the NOT/FIES spectrum of IC 418.

Our list of DIBs in Tc 1, M 1-20, and IC 418 are displayed in Tables 2.2, 2.3, and 2.4, respectively, where we give the measured central wavelength (λ_c),

[3]Image Reduction and Analysis Facility (IRAF) software is distributed by the National Optical Astronomy Observatories, which is operated by the Association of Universities for Research in Astronomy, Inc., under cooperative agreement with the National Science Foundation.

Table 2.2: Diffuse interstellar bands in Tc 1 and HR 6334.

Tc 1						HR 6334					
λ_c (Å)	Components (Å)	FWHM (Å)	EQW (mÅ)	S/N	EQW/E_{B-V} (Å/mag)	λ_c (Å)	Components (Å)	FWHM (Å)	EQW (mÅ)	S/N	EQW/E_{B-V} (Å/mag)
4427.51 [a,b]	...	19.35	860.0	403	3.74	4429.71	...	23.42	470.2	391	1.12
5776.22	...	1.14	7.2	402	0.03	5776.11	...	1.21	5.3	535	0.01
5780.65 [b]	...	2.02	112.1	420	0.49	5780.59	...	2.17	119.0	586	0.28
5797.21	...	0.82	25.7	536	0.11	5797.19	...	1.15	45.7	590	0.11
5849.74	...	0.89	2.2	437	0.01	5849.74	...	0.76	12.7	536	0.03
6196	6196.06 [c]	1.11	10.7	525	0.05	6196	6196.05 [c]	0.96	16.0	692	0.04
	6195.88	0.48	6.0		0.03		6195.89	0.40	10.4		0.02
	6196.54	0.39	2.6		0.01		6196.56	0.36	4.3		0.01
6203.33	...	2.03	36.7	560	0.16	6203.17	...	1.28	29.1	758	0.07
6250.36	...	1.74	8.7	610	0.04	6250.62	...	2.45	14.7	727	0.03
6270.08	...	1.66	15.0	618	0.06	6270	6269.98	1.47	25.8	494	0.06
6284.18	...	4.41	630	380	1.66	6284.15	...	4.55	309.8	693	0.74
6376	6376.22 [c]	1.38	2.6	559	0.01	6376	6376.40 [c]	1.36	12.7	612	0.03
	6376.05	0.57	1.7		0.01		6375.92	0.41	3.6		0.01
	6376.76	0.48	1.6		0.01		6376.65	0.76	6.4		0.01
6379	6379.41 [c]	1.13	8.7	625	0.04	6379	6379.47 [c]	1.26	56.4	812	0.13
	6379.14	0.56	4.9		0.02		6379.14	0.46	21.0		0.05
	6379.82	0.93	4.7		0.02		6379.78	1.08	35.4		0.08
6597.18	...	0.48	4.1	529	0.02	6597.14	...	0.45	5.0	338	0.01
6613.77	...	1.47	32.5	432	0.14	6613.74	...	1.40	91.8	464	0.22
6661	6661.09 [c]	1.12	3.5	341	0.01	6661	6660.81 [c]	1.09	22.8	337	0.05
	6660.64	0.64	2.5		0.01		6660.61	0.54	14.4		0.03
	6661.40	0.24	1.9		0.01		6661.35	0.30	5.4		0.01
6792.22	...	1.16	12.6	360	0.05	6792.07	...	1.10	15.2	329	0.04
7828.75	...	1.49	8.8	382	0.04	7828.45	...	1.07	6.1	572	0.01
7832.50	...	1.76	10.3	475	0.04	7832.63	...	2.11	14.5	636	0.03
8038.14	...	0.96	5.4	396	0.02	8038.01	...	0.81	7.0	460	0.02
8621.12	...	4.52	63.4	348	0.28	8621.15	...	4.50	51.7	626	0.12

The 3-σ errors in the EQWs scale as $\sim 3 \times$ FWHM/(S/N), while we estimate that the FHWMs in Tc 1 are precise to the 0.03 Å level (less for M 1-20 and IC 418).

[a] The parameters of this DIB are estimated by adopting a Lorentzian profile (see, e.g., Snow et al. 2002).

[b] Circumstellar absorption features (or diffuse circumstellar bands) may be possibly detected at these wavelengths (see Section 2.4).

[c] Undeblended DIB.

Table 2.3: Diffuse interstellar bands in M 1-20 and HR 6716.

M 1-20					HR 6716				
λ_c (Å)	FWHM (Å)	EQW (mÅ)	S/N	EQW/E_{B-V} (Å/mag)	λ_c (Å)	FWHM (Å)	EQW (mÅ)	S/N	EQW/E_{B-V} (Å/mag)
4426.56 [a]	19.94 [b]	2579.0 [b]	20 [c]	3.22	4429.27	22.25	595.8	233	2.71
5780.44	1.93	361.1	36	0.45	5780.41	2.01	164.5	792	0.75
5796.97	0.78	153.4	39	0.19	5796.95	0.74	37.2	661	0.17
5849.69	0.95	70.7	52	0.09	5849.69	0.84	9.3	639	0.04
6195.83	0.43	44.3	71	0.05	6195.82	0.41	13.2	612	0.06
6203.00	1.39	97.7	77	0.12	6203.02	1.25	28.9	688	0.13
6269.89	1.51	89.2	67	0.11	6269.70	1.02	12.4	684	0.06
6283.60	4.06	573.0	73	0.72	6283.51	4.29	474.4	641	2.16
6375.94	0.51	26.3	75	0.03	6375.89	0.65	6.3	656	0.03
6379.14	0.59	80.6	100	0.10	6379.12	0.63	22.5	687	0.10
6613.48	1.01	177.0	79	0.22	6613.41	0.86	37.5	581	0.17
6660.52	0.59	27.5	74	0.03	6660.55	0.41	5.0	531	0.02

The 3-σ errors in the EQWs scale as $\sim$3 $\times$ FWHM/(S/N), while the FHWMs are less precise than 0.03 Å.

[a] The parameters of this DIB are estimated by adopting a Lorentzian profile (see, e.g., Snow et al. 2002). The central wavelength in M 1-20 is very uncertain.

[b] Best estimates found by clipping out the narrow emission lines and smoothing the spectrum with boxcar 15. The error in the quoted EQW is estimated to be $\sim$786 mÅ.

[c] S/N in the original spectrum.

Table 2.4: Diffuse interstellar bands in IC 418 and HR 1890.

IC 418						HR 1890						Hobbs et al. (2008)	Luna et al. (2008)
λ_c (Å)	FWHM (Å)	EQW (mÅ)	S/N	EQW/E_{B-V} (Å/mag)		λ_c (Å)	FWHM (Å)	EQW (mÅ)	S/N	EQW/E_{B-V} (Å/mag)		EQW/E_{B-V} (Å/mag)	EQW/E_{B-V} (Å/mag)
4426.20 [a]	21.45	1001.0	116	4.35		...	...	...	...	...		1.10	...
5780.94	2.02	99.8	195	0.43		5780.97	1.68	25.5	344	0.32		0.23	0.46
5797.51	0.85	34.8	184	0.15		5797.46	1.07	8.4	336	0.10		0.18	0.17
5850.55	1.15	30.9	175	0.13		5850.44	1.03	7.1	351	0.09		0.09	0.061
6196.47	0.31	10.0	166	0.04		6196.27	0.29	2.9	343	0.04		0.03	0.053
6203.37	0.80	15.3	171	0.07		...	...	...	...	...		0.05	...
6270.24	1.08	15.7	183	0.07		...	...	...	...	...		0.07	...
6284.30	4.88	218.8	183	0.95		...	...	...	...	...		0.41	0.90
6376.41	0.35	2.9	137	0.01		...	...	...	...	...		0.04	...
6379.94	0.43	5.2	132	0.02		...	...	...	...	...		0.08	0.088
6614.11	1.04	30.8	146	0.13		6614.20	0.91	6.6	364	0.08		0.15	0.21

The 3-σ errors in the EQWs scale as $\sim 3 \times$ FWHM/(S/N), while the FHWMs are less precise than 0.03 Å.
[a] The parameters of this DIB are estimated by adopting a Lorentzian profile (see, e.g., Snow et al. 2002). The quoted central wavelength in IC 418 is quite uncertain.

the full width at half maximum (FWHM) as defined in Hobbs et al. (2008), the equivalent width (EQW[4]), the S/N in the neighbouring continuum, and the normalized equivalent widths (EQW/E(B-V)). For comparison, we also list in Table 2.4 the EQW/E(B-V) values measured in HD 204827 and field-reddened stars by Hobbs et al. (2008) and Luna et al. (2008), respectively. The DIB parameters were measured using standard tasks in IRAF with no assumption on the DIB profiles; the equivalent width is measured by marking two continuum points around the DIB of interest. This is because many DIBs show irregular profiles and precise definitions of central wavelengths and bandwidths are necessary. The only exception was the 4428 Å DIB for which we assumed a Lorentzian profile (this profile provides a perfect match to this strong band; see, e.g., Snow et al. 2002). We also list these parameters for the various interstellar components in those DIBs that are clearly resolved (e.g., the 6196 and 6379 Å DIBs; Table 2.2).

The Tc 1 optical spectrum displays two interstellar clouds at -6.80 km s^{-1} and $+25.00$ km s^{-1}, as indicated by the two absorption components for the atomic (Na I, Ca I) and molecular (CH^+) lines (see Figures 2.1 and 2.2, Table 2.5). Even the narrower DIBs towards Tc 1 (as 6379 Å) show this behaviour (see Figure 2.2 and Table 2.5). The same behaviour is shown by the comparison star HR 6334, which also shows the two interstellar components at the same radial velocities as Tc 1, confirming that both stars map similar ISM conditions.

The M 1-20 optical spectrum, however, displays one Na I interstellar component (i.e., at -6.54 km s^{-1}) with a blue assymetry that corresponds to a weaker non-resolved Na I interstellar component. Both components for the atomic Na I (e.g., at -6.12, and -26.43 km s^{-1}) interstellar lines are clearly resolved in the comparison star HR 6716 (see Figure 2.3 and Table 2.6), with the peculiarity that the Na I lines are broader in M 1-20. Only the strongest Na I interstellar component seems to be resolved in the DIBs (see Figure 2.3). The presence of two clear (and narrower) interstellar components in the comparison star suggests that both stars could map slightly different ISM conditions. For M 1-20 and its comparison star, we list the DIB parameters for the entire interstellar absorption (with no assumption on the DIB profile; Table 2.3).

[4]One-sigma detection limits for the EQWs in our spectra scale as ∼1.064 x FWHM / (S/N) (see, e.g., Hobbs et al. 2008).

Table 2.5: Radial velocities (in $\mathrm{km\,s^{-1}}$) for the atomic and molecular lines as well as DIB features with two interstellar components in Tc 1 and HR 6334.

Feature	Tc 1				HR 6334	
	CS		IS		IS	
Na I	−116.10	−83.00	−4.67	26.36	−4.67	26.36
Ca I			−7.16	22.98		
CH^+			−6.87	25.50	−2.83	31.24
CH					−5.86	27.96
CN (R1)					−5.34	(42)
CN (R0)					−4.57	29.25
CN (P1)					−4.18	31.02
DIB 6196Å			−8.03	25.11	−5.42	27.68
DIB 6376Å			−3.86	30.00	−7.05	33.34
DIB 6379Å			−6.58	23.97	−5.78	29.18

Typical uncertainty of $\sim \pm 1\ \mathrm{km\,s^{-1}}$.

Table 2.6: Radial velocities (in $\mathrm{km\,s^{-1}}$) for the atomic lines as well as DIB features in M 1-20 and HR 6716.

Feature	M 1-20		HR 6716	
	CS	IS	IS	
Na I	60.95	−6.54	−26.43	−6.12
DIB 5797Å		−5.19		−5.33
DIB 6196Å		−7.85		−7.88
DIB 6379Å		−8.63		−9.04

Typical uncertainty of $\sim \pm 1\ \mathrm{km\,s^{-1}}$.

The PN IC 418 seems to show also a main Na I interstellar component at a radial velocity of $+22.22\ \mathrm{km\,s^{-1}}$ and a much weaker, not completely resolved component at $\sim +5\ \mathrm{km\,s^{-1}}$ (see Figure 2.4 and Table 2.7). Thus, the DIB parameters for IC 418 are representative of the most prominent interstellar component (Table 2.4). In the comparison star HR 1890, two interstellar components for the atomic Na I (e.g., at +5.42 and $+23.75\ \mathrm{km\,s^{-1}}$) are clearly resolved, suggesting that both stars could map slightly different ISM conditions. Anyway,

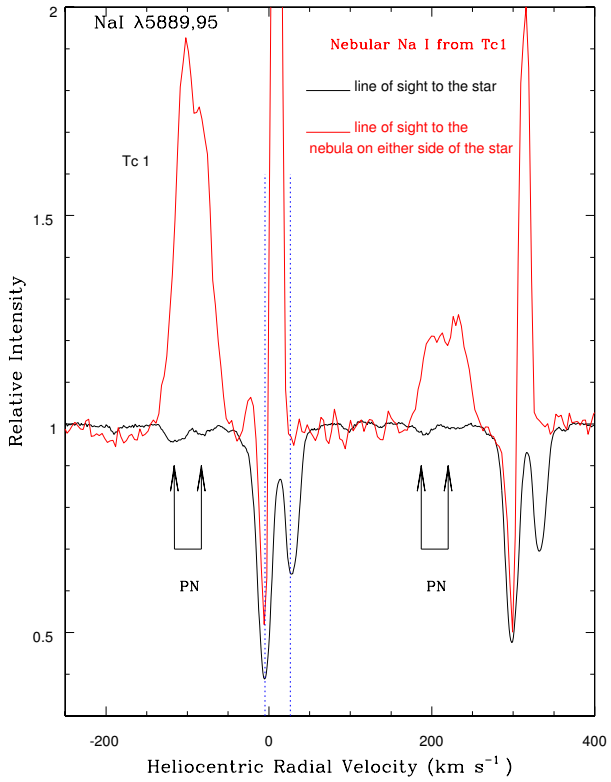

Figure 2.1: Na I D lines observed towards PN Tc 1 central star (black) and average of two positions in the nebula 2.7 arcsec away from the central star on either side (red) (from Williams et al. 2008). The dashed blue lines indicate the interstellar Na I D components at -6.8 and $+25$ km s^{-1}. The black arrows indicate the corresponding nebular components at -116.1 and -83 km s^{-1}. The sharp emission close to 0 km s^{-1} radial velocity is earth's airglow. The absorption spectrum is in the stellar continuum units, while the emission spectrum is in the nebular continuum units.

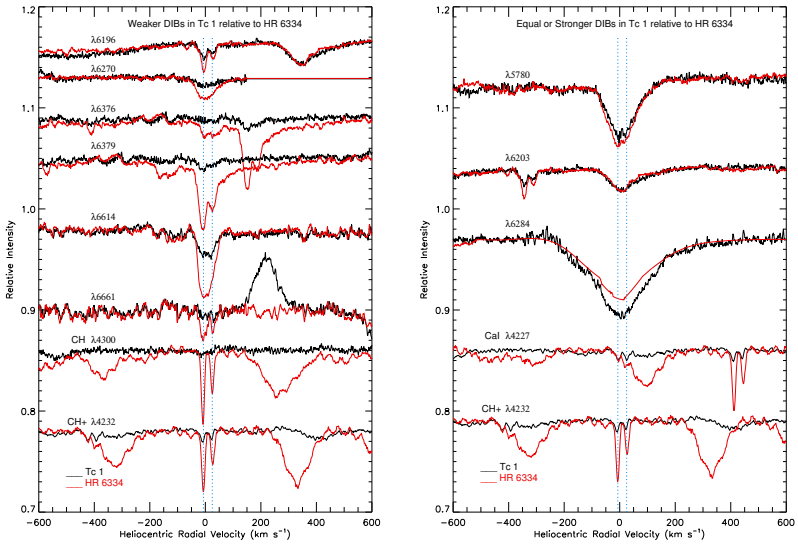

Figure 2.2: Profiles of a selection of DIBs with various strengths and widths are displayed with respect to the heliocentric radial velocity. Weaker (or nearly equal) and stronger DIBs in Tc 1 (in black) relative to HR 6334 (in red) are displayed in the left and right panels, respectively. The profiles are shifted vertically for clarity. The CH, CH^+, and Ca I profiles at the bottom show the two interstellar components at -6.8 and $+25$ km s^{-1} (marked with blue vertical dotted lines) seen in both sources. The sharper DIBs in both Tc 1 and HR 6334 also show these two components. The DIBs displayed in the left panel are consistent with the lower reddening of E(B-V)= 0.23 for Tc 1 as compared to E(B-V)=0.42 for HR 6334. The right panel, however, shows that the carrier(s) of these DIBs are enhanced (for the given E(B-V)) in the sight line to Tc 1.

we list the DIB parameters for the entire interstellar absorption in both stars. We note that HR 1890 displays a very low reddening of E(B-V)=0.08, and only the strongest DIBs are clearly detected.

We identified 20, 12, and 11 DIBs in Tc 1, M 1-20, and IC 418, respectively.

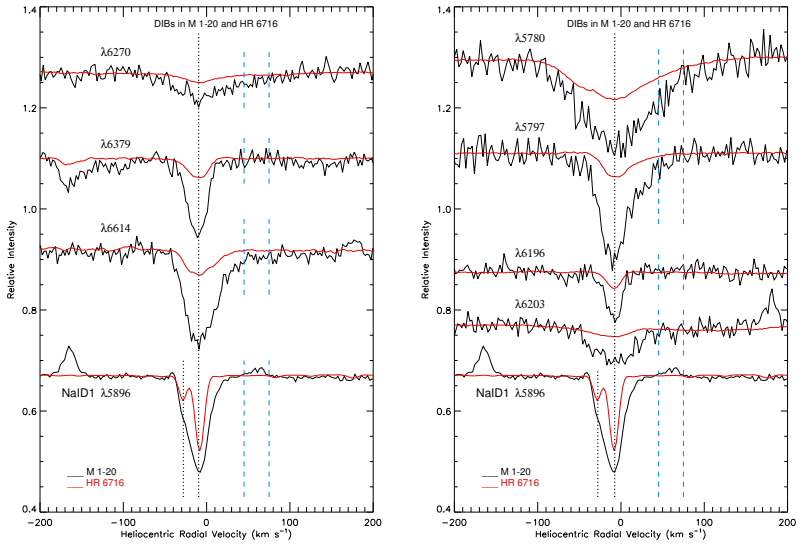

Figure 2.3: Profiles of a selection of DIBs with various strengths and widths with respect to the heliocentric radial velocity. DIBs with similar and different profiles in M 1-20 (in black) relative to HR 6716 (in red) are displayed in the left and right panels, respectively. The profiles are shifted vertically for clarity. The Na I profiles at the bottom show the interstellar components (marked with black vertical lines) seen in M 1-20 and HR 6716. The DIBs displayed in the two panels are consistent with the higher reddening of E(B-V)= 0.80 for M 1-20 as compared to E(B-V)=0.22 for HR 6716. The nebular radial velocity range for M 1-20 is denoted by blue vertical lines ($\sim$+61 km s^{-1}).

All of these absorption bands are known DIBs, as previously reported by Hobbs et al. (2008). It should be noted here that we could not estimate the total absorption of the well studied 6993 and 7223 Å DIBs in our three PNe because of the strong meddling from the telluric lines. We also note that our radial velocity analysis in Tc 1 shows that the $\sim$6309 and 6525 Å absorption features reported by García-Hernández & Díaz-Luis (2013) should be identified as stellar

Table 2.7: Radial velocities (in km s^{-1}) for the atomic and molecular lines, as well as DIB features in IC 418 and HR 1890.

Feature	IC 418		HR 1890	
	CS	IS	IS	
Na I	58.36	22.22	5.42	23.75
CH		22.67		
DIB 5780Å		25.34		23.33
DIB 5797Å		22.16		22.15
DIB 5850Å		25.60		30.97

Typical uncertainty of $\sim \pm 1$ km s^{-1}.

He II absorption lines[5]. Their relative strengths (and widths) are consistent with the series of He II features that are clearly seen in our Tc 1 optical spectrum (e.g., at 6171, 6234, 6406, 6683, 6891, 7178, 8237, and 9345 Å).

2.3.1 Normal DIBs

We concentrate here on those DIBs that seem to be normal for their reddening, the so-called "normal" DIBs. In Tc 1, the PN with the highest quality spectrum and a proper comparison star, their strengths are consistent with the E(B-V) value, and both PN and its comparison star display similar normalized equivalent widths (see Table 2.2 and Figure 2.2). There are fifteen normal DIBs in Tc 1: six of them are among the strongest DIBs most commonly found in the ISM (5797, 5850, 6196, 6270, 6379, and 6614 Å)[6], while the other nine DIBs (5776, 6250, 6376, 6597, 6661, 6792, 7828, 7833, and 8038 Å) are weaker interstellar features already reported by Hobbs et al. (2008). The situation is less clear for the fullerene PNe M 1-20 and IC 418. This is because the comparison stars for both PNe seem to map slightly different ISM conditions (see above). The comparison star of IC 418 also displays a very low reddening that prevents

[5]These are the ∼6310 and ∼6527 Å stellar He II absorption lines, which are blue-shifted by ∼90 km s^{-1} (the central's star velocity) in Tc 1.

[6]The parameters for the 5797 and 5850 Å DIBs are more uncertain in Tc 1 because of their low intrinsic intensity and some contamination by nearby spectral features. For example, there is a strong stellar absorption line of C IV at 5799.84 Å and a nebular emission feature in the proximity of the 5850 Å DIB.

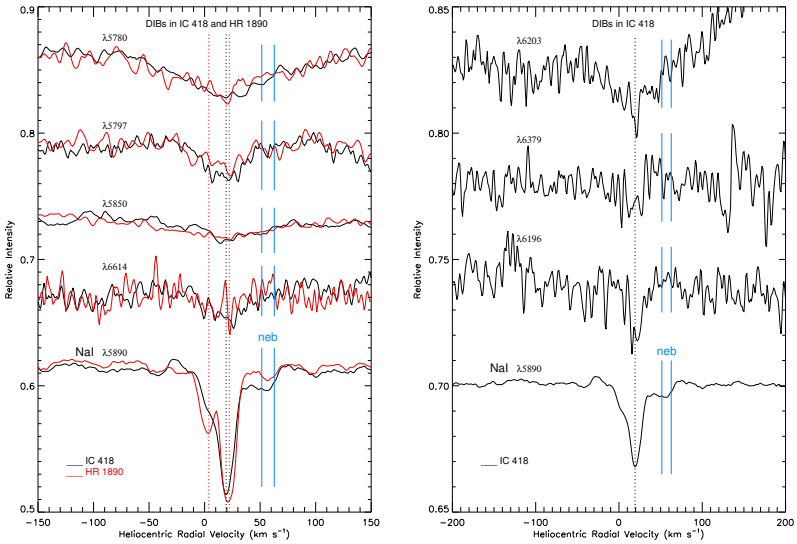

Figure 2.4: Profiles of a selection of DIBs with various strengths and widths are displayed with respect to the heliocentric radial velocity. Some normal and unusually strong DIBs in IC 418 are displayed (not in HR 1890 due to the low reddening of 0.08). The Na I profiles show the prominent interstellar component at 22.22 km s^{-1} (marked with a black vertical dotted line) in IC 418. The nebular radial velocity range for IC 418 is denoted by blue vertical lines ($\sim$+58 km s^{-1}).

detection of a significant number of DIBs. Despite this, the classification of the latter DIBs (if detected in our spectra) as "normal" DIBs holds here for M 1-20 and IC 418 (see below).

The strengths of the sextet of common DIBs (5797, 5850, 6196, 6270, 6379, and 6614 Å) are roughly consistent with the interstellar reddening in our three PNe. The EQW/E(B-V) ratio of these DIBs for the three PNe agree reasonably well with the values measured in their corresponding comparison stars (Tables 2.2, 2.3, and 2.4) or with the EQW/E(B-V) values observed in HD 204827

(Hobbs et al. 2008) and/or field-reddened stars (Luna et al. 2008). The 6196, 6376, 6379, and 6661 Å DIBs towards Tc 1 (and its comparison star HR 6334) display the two interstellar components at the same radial velocities in both objects (Table 2.2 and Figure 2.2). In M 1-20 and its comparison star HR 6716, we could measure only one main interstellar component for all DIBs (Table 2.3 and Figure 2.3). As in the case of M 1-20, all common DIBs towards IC 418 (and its comparison star HR 1890) only display one main interstellar component (Table 2.4 and Figure 2.4). We note, however, that only a few DIBs (five) are detected towards HR 1890 (Table 2.4), and all DIBs are intrinsically very weak due to the very low reddening (E(B-V)=0.08) in the HR 1890 line of sight. Thus, Table 2.4 also lists the EQW/E(B-V) values of HD 204827 (Hobbs et al. 2008) and field-reddened stars (Luna et al. 2008) for comparison with IC 418. The EQW/E(B-V) values of the sextet of common DIBs in IC 418 are similar to those in HD 204827 and field-reddened stars.

The measured intensities of the nine other "normal" DIBs (at ∼5776, 6250, 6376, 6597, 6661, 6792, 7828, 7833, and 8038 Å)[7] are also roughly consistent with the E(B-V) values in our three fullerene PNe. All these DIBs are detected in Tc 1. For the narrower 6196, 6376, 6379, and 6661 Å DIBs in Tc 1 and its comparison star, we also give the parameters for each one of the interstellar components mentioned above (Table 2.2). In M 1-20, however, only two of these weak DIBs (6376 and 6661 Å) are detected in our spectrum (Table 2.3). In IC 418, we only detect the weak DIB at 6376 Å because the other weak DIBs are below our 1-σ detection limits.

In short, the carriers of the so-called "normal" DIBs do not seem to be particularly over-abundant towards fullerene PNe, since they are consistent with those expected for the general diffuse ISM.

2.3.2 Unusually strong DIBs

Interestingly, some DIBs are found to be unusually strong in fullerene PNe. The five DIBs at ∼4428, 5780, 6203, 6284, and 8621 Å are unusually strong towards Tc 1. Their strengths in Tc 1 are higher than expected for the E(B-V) of 0.23; Tc 1 displays EQW/E(B-V) values higher than those in the comparison

[7]The parameters for the 5776 Å DIB are uncertain in Tc 1 because of its low intrinsic intensity and contamination by a nearby nebular emission feature.

star HR 6334 (Table 2.2 and Figure 2.2). This is clearly shown in Figure 2.5, where we plot the EQW/E(B-V) values of DIBs in Tc 1 versus HR 6334 (left panel) and those in the reference star HD 204827 versus HR 6334 (right panel). The EQW/E(B-V) values of DIBs in HR 6334 scale nicely with those in HD 204827 (the only exception is the 6284[8] Å DIB, which is affected by telluric absorption lines; see Figure 2.6), suggesting similar ISM properties towards both stars. In Tc 1, however, the five unusually strong DIBs mentioned above clearly deviate from the linear relation followed by most of the DIBs that also scale well with those in HR 6334 (and HD 204827). The central radial velocity of these unusually strong interstellar features is the same in both Tc 1 and the comparison star (with the apparent exception of the 4428 Å feature; see Section 2.4), confirming their interstellar origin. In addition, the neutral molecular lines (CH, CN[9]) are much weaker or absent towards Tc 1 (Figure 2.2), indicating a higher degree of ionization. This may indicate that carriers of these DIBs (enhanced towards Tc 1) may be ionized species.

The situation is again less clear for the fullerene PNe M 1-20 and IC 418. It seems clear, however, that at least the ∼4428 Å DIB is unusually strong in both PNe (see below), showing EQWs that are much higher than expected for their E(B-V) values.

For the well-studied 4428 Å DB we adopted a Lorentzian profile (Snow et al. 2002), obtaining EQWs of ∼860, 2579, and 1001 mÅ for Tc 1, M 1-20, and IC 418, respectively. The 4428 Å DB in Tc 1 and IC 418 is at least a factor of two higher than expected for their low reddening of E(B-V)=0.23 (see e.g., Figure 6 and 15 in Snow et al. 2002 and van Loon et al. 2013, respectively), while this DB is ∼1.5 times more intense than expected in M 1-20.

The DIB at 5780 Å is another intereresting feature that also could be an unusually strong DIB towards IC 418 (Table 2.4). In IC 418, it is stronger (EQW/E(B-V)=0.43) than in the comparison star HR 1890 (with EQW/E(B-V)=0.32) and in the Hobbs et al. (2008) reference star HD 294827. However, it has a similar strength to field-reddened stars (Luna et al. 2008). Unfortunately, the DIBs at ∼6203 and 6284 Å are not present in the low-reddening star HR

[8]This band was measured after applying a perfect telluric correction with IRAF. HR 6334 was used as divisor to remove these lines.

[9]Interstellar CN lines at ∼3874 Å.

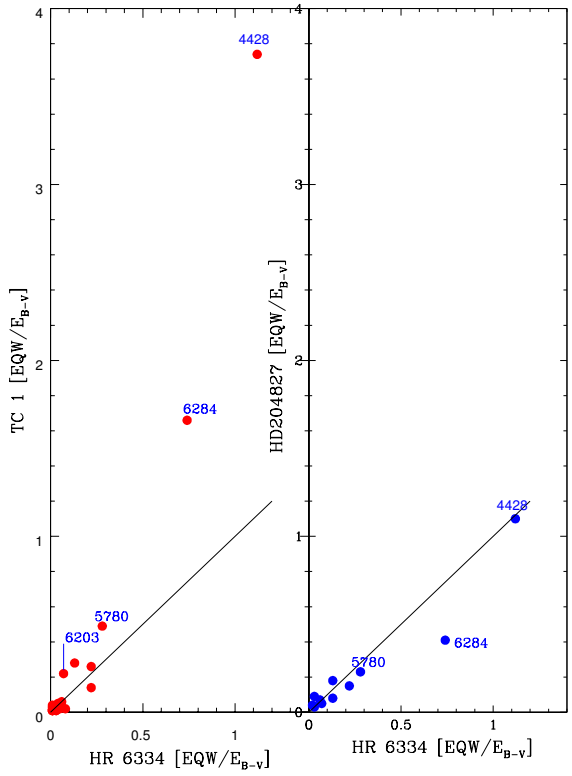

Figure 2.5: Plots of EQW/E(B-V) of Tc 1 with respect to (w.r.t.) HR 6334 (left panel) and HD 204827 w.r.t. HR 6334 (right panel). The EQW/E(B-V) values of HR 6334 scale nicely w.r.t. HD 204827. For Tc 1, most of the DIBs also scale well w.r.t. HR 6334 (and HD 204827) with the exception of the five unusually strong DIBs (those at ∼4428, 5780, 6203, 6284, and 8621 Å; see text), which deviate from the linear relation.

1890. Similar to the 5780 Å DIB, these DIBs in IC 418 are stronger than in the star HD 294827 but of similar strenght to those seen in the sample of field-

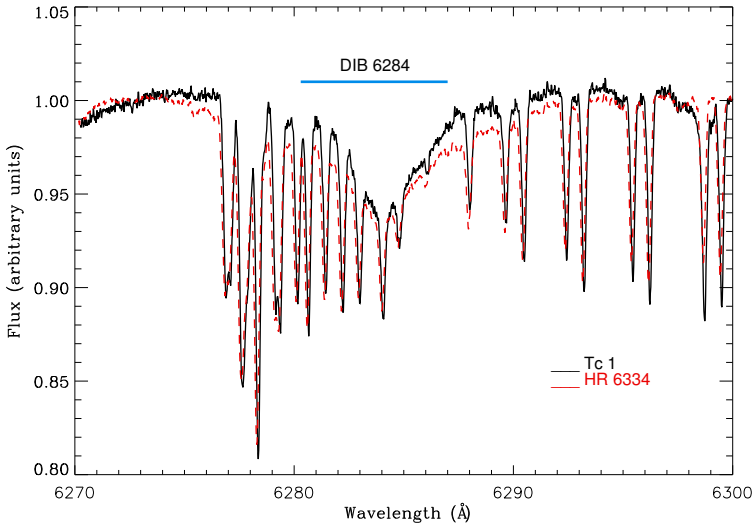

Figure 2.6: Profiles of the 6284 Å DIB in Tc 1 (black) and in the comparison star HR 6334 (red). This spectral range is strongly contaminated by telluric molecular oxygen lines.

reddened stars by Luna et al. (2008). Finally, our IC 418 optical spectra do not cover the spectral region around the 8621 Å feature.

As mentioned above, the situation is also less clear for M 1-20. Indeed, the 5780 and 6284 Å DIBs in M 1-20 are weaker than in HR 6716, while the 6203 Å DIB is of equal strength in both sources. Apparently, the bands at 5780, 6203, and 6284 Å seem to be unusually strong towards both M 1-20 and HR 6716 (see Table 2.3). As in the case of IC 418, these DIBs are stronger than in the reference star HD 294827 but similar to field-reddened stars. The most remarkable outcome is the complete lack of the 8621 Å DIB towards M 1-20, which otherwise is very intense in the Tc 1 line of sight.

Finally, it is worth mentioning here that the DIB at ∼6203 Å varies among the fullerene PNe in our sample. This DIB and the other band at 6205 Å are usually measured as two distinct interstellar absorptions (e.g., corresponding to

different carriers; see, e.g., Porceddu et al. 1991). The complex band at ∼6203 Å is especially noteworthy, in which the EQW/E(B-V) ratio is two to three times higher for Tc 1 than for the comparison star HR 6334 and the reddened star HD 204827 (Hobbs et al. 2008). Towards IC 418, the 6203 Å DIB is not very strong, although is not detected in the line of sight of the low-reddening comparison star HR 1890. The 6203 Å DIB towards M 1-20 and its comparison star HR 6716 displays a similar EQW/E(B-V) ratio. Curiously, the secondary DIB at ∼6205 Å is not clearly detected towards any of our sample PNe. This DIB is not easily recognized (resolved) from the dominant 6203 Å DIB. Furthermore, we can find no evidence for the presence of the 6205 Å interstellar absorption in IC 418 because it coincides with a strong nebular emission line (see Figure 2.4).

2.4 Diffuse circumstellar bands

The detection of diffuse circumstellar bands (DCBs) is very difficult because high S/N spectra are mandatory for detecting the presumably much weaker circumstellar features. Also, the DCBs have to be distinguished from the DIBs, and this distinction can only be made by measuring the radial velocities of the circumstellar and interstellar components in the line of sight to our PNe. The S/N is too low in PN M 1-20, preventing any search for DCBs towards this object. A higher quality (S/N∼100-200) optical spectrum was obtained for IC 418, but its relatively low radial velocity (∼58 $\mathrm{km\,s^{-1}}$; Dinerstein et al. 1995) makes it difficult to distinguish possible DCBs from the DIBs. However, our high-quality (S/N > 300) spectra for PN Tc 1, together with its higher radial velocity (in the range from -83 to -130 $\mathrm{km\,s^{-1}}$; Williams et al. 2008), may permit us to search for the possible presence of DCBs.

The nebular absorption lines in the line of sight to Tc 1 show heliocentric radial velocities in the range of -83 to -130 $\mathrm{km\,s^{-1}}$ (Williams et al. 2008), while the star's heliocentric radial velocity is measured as -90 ± 12 $\mathrm{km\,s^{-1}}$. Any absorption/emission feature in the radial velocity range from -80 to -130 $\mathrm{km\,s^{-1}}$ is then expected to be related to the Tc 1's expanding circumstellar (nebular) gas. Indeed, the Na I D lines show two distinct absorption components at -83 and -116 $\mathrm{km\,s^{-1}}$ apart from the ISM components (see Figure 2.1 and Table 2.5). The 5780 Å DIB towards Tc 1 matches the velocity of the ISM, as expected (see Figure 2.2). However, we find a (blue-shifted) very weak absorption

feature (at the ∼3-sigma level; EQW∼6.8 mÅ and FWHM∼0.99 Å) at the Tc 1 nebular velocity (centred at ∼−125 km s^{-1} and indicated in Figure 2.7), which is not present in the comparison star HR 6334 (see Figure 2.2). There is no known DIB at this wavelength, and it does not correspond to any stellar line (too narrow) or telluric feature (not present in HR 6334). In addition, the velocity separation is not in the right direction for another ISM cloud. This circumstellar absorption feature is narrower than the interstellar one, and the primary interstellar feature is broader owing to the contribution of at least two interstellar clouds (see above). The physical/chemical conditions in the Tc 1's circumstellar envelope are also expected to be different from those in the ISM, and the widths may not be necesarily the same. We note that there is a nebular emission counterpart (Figure 2.7) of the very weak DCB around 5780 Å, and the presence of this nebular emission at the radial velocity of Tc 1 furthermore suggests its circumstellar origin (see below).

Curiously, the 4428 Å feature in Tc 1 seems to be blue-shifted (by ∼126 km s^{-1}) relative to the one in HR 6334 (marked by a red line in Figure 2.8). At the top of Figure 2.8, the profiles of Tc 1 have been shifted by 126 km s^{-1} redwards and superposed on the HR 6334 profile to make the minima coincide and show the apparent difference. It also aligns the photospheric lines of both stars, suggesting that the velocity of the 4428 Å absorption feature is close to the Tc 1's nebular velocity. In Figure 2.9, the profiles (normalized on the EQW of the 4428 Å band) of Tc 1 (left panel) and HR 6334 (right panel) have been superposed on the profile of an O6.5 star (HD 148937). This O6.5 star has been displaced (in velocity) in both panels to match the 4428 Å profiles observed in both Tc 1 and HR 6334. The 4428 Å profiles both in Tc 1 and HR 6334 match the one in the O6.5 star (HD 148937) as well as our polynomial fits (the green profiles in Figure 2.9)[10] This indicates that the minima of the 4428 Å feature in Tc 1 and HR 6334 are well determined. The minimum of the 4428 Å feature in HR 6334 occurs around 0.0 km s^{-1}, while it is blue-shifted by ∼126 km s^{-1} in Tc 1. The blue shift could either be a result of vibrational-rotational structure of the carrier molecule or could be due to radial motions of the carriers. The velocity shift is about the same amount as the radial velocity of the circumstellar gas of Tc 1 (also the Na I D absorption components). A nebular emission feature is present at the wavelength corresponding to the blue

[10]Despite the pollution by many lines in HR 6334, Figure 2.9 shows that the 4428 Å profile in HR 6334 match our polynomial fit very well (the green profile in Figure 2.9 (right panel).

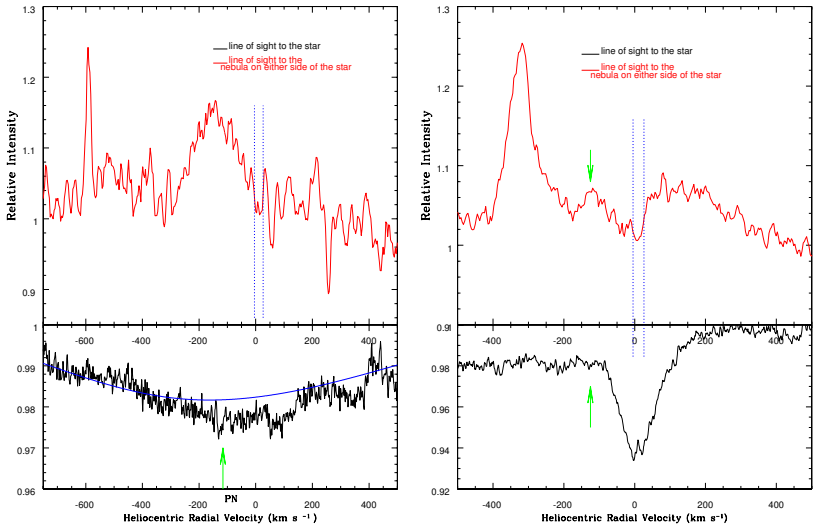

Figure 2.7: Profiles of the broad 4428 Å band (left panel) and of the 5780 Å feature (right panel) towards Tc 1 central star (black) and average of two sight lines to the nebular position on either side of the nebula (from Williams et al. 2008). In both panels, the dashed blue lines mark the interstellar components at -6.8 and $+25$ km s^{-1}. Note the coincidence in velocity (marked by green arrows) of the profile centre of the broad 4428 and of the weak 5780 Å circumstellar absorptions and the corresponding nebular emissions. The emission feature to the left of the 5780 Å nebular emission is unidentified.

shift of λ4428 absorption feature (see below), which cannot be identified with any nebular line (see, e.g., Sharpee et al. 2003 for a compilation of nebular lines in PN IC 418 that displays an effective temperature that is almost identical to Tc 1). Thus, it seems likely that the apparent blue shift of the 4428 Å feature is real, indicating a circumstellar (nebular) nature for the carrier(s). Also, the ISM contribution to the 4428 Å feature in Tc 1 is expected to be a minor one; even smaller than the one in HR 6334. This is owing to the fact that DIBs are absorption bands of interstellar origin and the interstellar reddening of Tc

1 (E(B-V)=0.23; Williams et al. 2008) is much lower than those of HR 6334 (E(B-V)=0.42; Wegner 2003) and HD 148937 (E(B-V)=0.67; Wegner 2003).

If the material in and around the nebula (plus central star) is giving rise to the circumstellar absorption components in the sight line towards the star (as seen in Na I D and some DIBs), then the same material is expected to be seen in emission in the sight lines of the nebula away from the central star. We have investigated the Tc 1 nebular spectra obtained by Williams et al. (2008) and their spectroscopic observations in lines of sight away from the central star indeed seem to confirm this expectation. The average spectrum of the nebula at two slit positions 2.7 arcsec away from the Tc 1 central star (Williams et al. 2008) - which samples the same *Spitzer* volume that revealed the fullerenes in Tc 1 - shows the Na I D lines in emission (also the Ca II K lines, but these are much weaker) at the radial velocity of the object (see Figure 2.1 and Table 2.2). The Na I D emission components have slightly more positive radial velocity ($\sim$10 $\mathrm{km\,s^{-1}}$ with respect to the absorption lines), suggesting a possible expansion velocity of -10 $\mathrm{km\,s^{-1}}$ for the Na I gas. Such a correspondence of emission feature occurs with λ4428 absorption. Similar emission corresponding to λ5780 also seems to be present in the Tc 1 nebular spectrum. The presence of 4428 and 5780 Å nebular emission (see Figure 2.7) at the radial velocity of Tc 1 furthermore suggests their circumstellar origin. The DCBs reported here are known to be among the strongest DIBs. The strong 4428 Å feature is known to correlate well with other DIBs like 5780 (e.g., van Loon et al. 2013). The 5780 Å DIB is also known to correlate with the broad 6284 Å feature in the ISM (see, e.g., Friedman et al. 2011) but might differ in circumstellar environments. Interestingly, the 6284 Å DIB is very strong in Tc 1 and might even be hiding a circumstellar absorption feature as well; in Figure 2.2, there is evidence of some asymmetry in the 6284 Å DIB profile at the Tc 1's radial velocity range (from -83 to -130 $\mathrm{km\,s^{-1}}$).

The PN IC 418 also shows circumstellar (nebular) absorption components (although much weaker than in Tc 1) in the Na I D lines (Dinerstein et al. 1995; see also Figure 2.4 and Table 2.7). Unfortunately, the 4428 Å feature is not seen in its (low reddening) comparison star HR 1890, and we could not properly check whether the profile minimum of this feature is red-shifted to the observed nebular velocity of IC 418. The comparison of the 4428 Å profile in IC 418 with the one in the O6.5 star HD 148937 displayed in Figure 2.10 tentatively

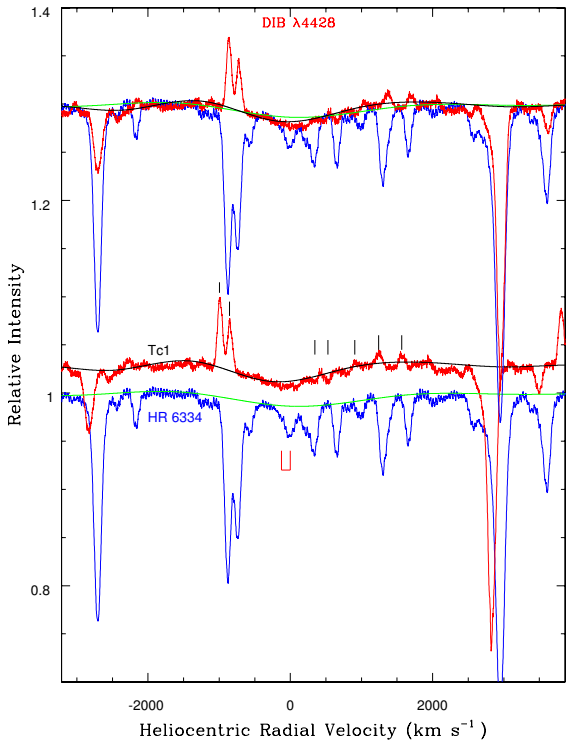

Figure 2.8: Profiles of the 4428 Å feature in Tc 1 (red) and in the comparison star HR 6334 (blue). The black and green profiles of the 4428 Å feature have been constructed by avoiding the stellar emission and absorption lines (marked by short black lines) and by fitting a high-degree polynomial. The minimum of the 4428 Å feature in HR 6334 occurs around 0.0 km s^{-1}, while it seems to be blue-shifted in Tc 1 (red line). At the top, the profile of Tc 1 has been shifted by 126 km s^{-1} redwards and superposed on the HR 6334 profile to illustrate the apparent non-coincidence of the minima of the profiles in both stars.

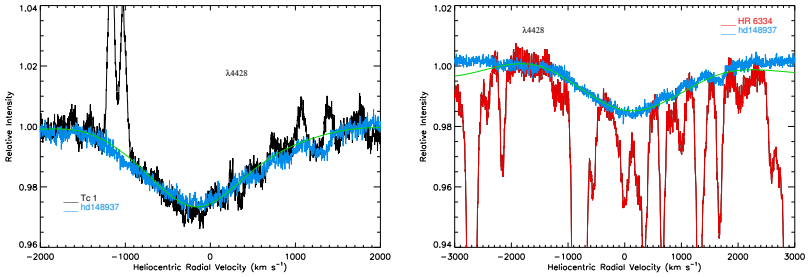

Figure 2.9: Profiles of the 4428 Å feature in Tc 1 (left panel) and in the comparison star HR 6334 (right panel) superposed on the profile of the O6.5 star HD 148937. The O6.5 star has been displaced (in velocity) in both panels to make the 4428 Å band coincide with the profile and the minima of the 4428 Å band towards Tc 1 and HR 6334. All spectra have been normalized on the EQW of the 4428 Å band. The minimum of the feature in HR 6334 occurs around 0.0 $\mathrm{km\,s^{-1}}$, while it seems to be blue-shifted in Tc 1. The green profiles of the 4428 Å feature in Tc 1 and HR 6334 are the polynomial fits shown in Figure 2.8. The superposed spectrum of an O6.5 star (in blue) support the non-coincidence of the profiles minima in Tc 1 and HR 6334.

suggests that this feature in IC 418 could be slightly red-shifted with respect to the expected interstellar wavelength. As in the case of Tc 1, this may explain the circumstellar (nebular) nature of the carrier, since the nebular radial velocity is $\sim$+58 $\mathrm{km\,s^{-1}}$. However, the 4428 Å profile in IC 418 is not fully reproduced by the one in HD 148937, and the central wavelength of this feature is uncertain (i.e., more uncertain than in the case of Tc 1 above).

As mentioned above, the S/N in the M 1-20 spectrum is probably too low for detecting DCBs in this object. The heliocentric radial velocity of the nebula has been measured by us as $\sim$61 $\mathrm{km\,s^{-1}}$ (from a few He I nebular emission lines). This radial velocity is shown in Figure 2.3. In our low S/N M 1-20 spectrum, there is no evidence of any DIB component close to this radial velocity.

Based on the EQW of the strong DIB at 5780 Å towards Tc 1 (EQW=112.1 mÅ) relative to the weak DCB around the same wavelength (EQW=6.8 mÅ),

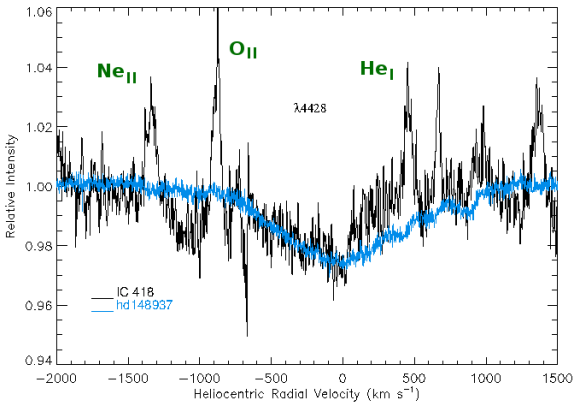

Figure 2.10: Profiles of the 4428 Å feature in IC 418 (in black) superposed on the profile of the O6.5 star HD 148937 (in blue). The O6.5 star has been displaced (in velocity) to try the 4428 Å band coincide with the profile and the minima of the 4428 Å band towards IC 418. Note that both spectra have been normalized on the EQW of the 4428 Å band. The 4428 Å profile in IC 418 is not fully reproduced by that in HD 148937 and its central wavelength is quite uncertain (see text).

we can estimate the S/N needed to detect this DCB in M 1-20 and IC 418. An EQW(DIB)/EQW(DCB) ratio of 16.5 is obtained for Tc 1. Adopting this value for the other PNe, one can estimate the expected EQW of the 5780 Å DCB; EQW(DCB) values of 20.1, and 6.1 mÅ are obtained for M 1-20 and IC 418, respectively. Then, when assuming the same FWHM (990 mÅ) as in Tc 1, the needed S/N for the DCB feature to be detected at three sigma can be obtained (EQW$\sim$ 3 x FWHM / (S/N); see Hobbs et al. 2008). We find that we would need S/N$\sim$143 and 491 for M 1-20 and IC 418, respectively. Thus, our non-detection of the DCBs in the latter PNe may be due to the lower S/N in our spectra for both objects (see Tables 2.3 and 2.4), or to their lower nebular radial velocities.

In summary, the present data show that DCBs might not be uncommon in

fullerene-containing PNe and suggest the first detection of two DCBs at 4428 and 5780 Å in the fullerene-rich circumstellar environment around the PN Tc 1. However, we prefer to be cautious until these posible DCB detections are confirmed in other PNe with fullerenes. The three fullerene-containing PNe in our sample display very weak circumstellar absorptions of Na I, and the intrinsic weakness of the DCBs (e.g., 5780 Å) is very likely related with the low column density of the gas (and dust) in their circumstellar envelopes. The strength of the 5780 Å circumstellar absorption in fullerene PNe is likely to be correlated with the circumstellar Na column density and the best PNe to unambiguously confirm that our detection of DCBs are those showing a strong Na I circumstellar absorption that is well separated (i.e., at a very different radial velocity) from the Na I interstellar components (e.g., IC 4997 and BD +30°3639; Dinerstein et al. 1995).

2.5 Electronic transitions of neutral C_{60}

The strongest allowed electronic transitions of neutral gas phase C_{60} molecules, as measured in laboratory experiments, are located at 3760, 3980, and 4024 Å with widths of 8, 6, and 4 Å, respectively (Sassara et al. 2001; see also García-Hernández et al. 2012a). García-Hernández & Díaz-Luis (2013) found no evidence of these strong neutral C_{60} optical bands in absorption (or emission) in the fullerene PN Tc 1.

The S/N in the M 1-20 optical spectrum is too low to search for neutral C_{60} features in its spectrum (García-Hernández & Díaz-Luis 2013), but here we have searched the higher S/N (∼100 in the continuum around 4000 Å) spectrum of the PN IC 418 for the strongest electronic transitions of neutral C_{60} mentioned above. As in the case of Tc 1, we can find no evidence of neutral C_{60} in absorption (or emission) around the expected wavelengths of ∼3760, 3980, and 4024 Å. This is shown in Figure 2.11 where we display the IC 418 velocity-corrected spectra around the most intense C_{60} transitions in comparison with those of Tc 1 and its comparison star HR 6334. We note that several strong O lines and He I 4026 Å very likely prevent identification of any broad and weak absorption feature around 3760 and 4024 Å, respectively. However, there is no evidence of the neutral C_{60} feature at 3980 Å, a wavelength region that is free of other spectral features.

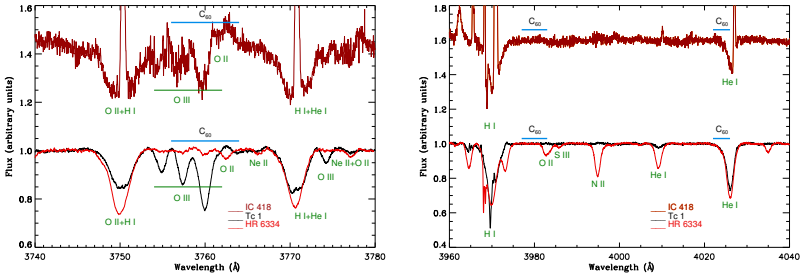

Figure 2.11: Velocity-corrected spectra of IC 418 (in brown), Tc 1 (in black) and HR 6334 (in red) around 3760 Å (left panel) and 4000 Å (right panel) where the atomic line identifications are indicated (in green). The expected positions (and FWHMs) of the C_{60} features are indicated on top of the spectra. There is no evidence (additional absorption and/or emission) in IC 418 and Tc 1 for the neutral C_{60} features at 3760, 3980, and 4024 Å.

The one-sigma detection limits on the EQWs derived from our IC 418 spectrum are 202, 75, and 44 mÅ for the 3760, 3980, and 4024 Å neutral C_{60} transitions, respectively. By using the Spitzer formula ($N \sim 10^{20} \times (EQW/(\lambda^2 \times f))$), where f[11] is the oscillator strength of each C_{60} transition (Sassara et al. 2001), this translates into column densities of $\sim 2 \times 10^{13}$, 4×10^{13}, and 2×10^{13} cm^{-2}. These column density limits are similar to those previously obtained in Tc 1 by García-Hernández & Díaz-Luis (2013) ($\sim 6 \times 10^{12}$, 1×10^{13}, and 6×10^{12} cm^{-2}). By following the latter work, we could in principle compare these column-density limits with estimates of the circumstellar density of C_{60} molecules as derived from the IR C_{60} emission bands.

Unfortunately, only two C_{60} IR bands (those at $\sim$17.4 and 18.9 μm) were covered by the IC 418 *Spitzer* spectrum, making the estimation of the number of C_{60} molecules ($N(C_{60})$) and excitation temperature ($T(C_{60})$) from the Boltzmann excitation diagram rather uncertain. Such column-density estimates are very sensitive to $T(C_{60})$, and this temperature is very poorly constrained in IC

[11]The oscillator strength of the $\sim$4024 and 3980 C_{60} bands is f=0.015, while the 3760 Å band has f=0.075 (Braga et al. 1991; Leach et al. 1992).

418 given that the short wavelength C_{60} bands are not available and that the C_{60} 17.4 μm band is blended with PAH emission. In addition, the derivation of the C_{60} column density based on the IR-emission spectrum relies on the assumption that C_{60} is at thermal equilibrium, and this is still an open question (see Chapter 4, Section 4.5 for more details; Bernard-Salas et al. 2012).

2.6 The fullerenes - DB connection

Most of the strongest and well-studied DIBs, as well as other weaker DIBs towards Tc 1, are found to be normal for its reddening. This indicates that the carriers of these "normal" DIBs are not particularly overabundant towards fullerene PNe. The exceptions are the DIBs at 4428, 5780, 6203, 6284, and 8621 Å, which are found to be unusually strong towards Tc 1. The radial velocities of the 5780, 6203, 6284, and 8621 Å features confirm their insterstellar origin, and the higher degree of ionization towards Tc 1 (in comparison with its comparison star) suggests that their carriers may be ionized species (see Section 2.3.2). The 4428 Å feature, however, seems to be centred at the Tc 1's radial velocity, suggesting a circumstellar origin (see Section 2.4). The situation is less clear for M 1-20 and IC 418 because their comparison stars seem to map slightly different ISM conditions (see Section 2.3.2), but at least the 4428 Å feature is also found to be unusually strong in the latter fullerene PNe.

The unusually strong 4428 Å feature towards Tc 1 and M 1-20 prompted the idea that the 4428 Å carrier may be related to fullerenes or fullerene-based molecules (García-Hernández & Díaz-Luis 2013). Our new finding of an unusually strong 4428 Å feature towards IC 418 suggests that this may be a common characteristic of fullerene PNe, reinforcing the speculation of a possible fullerene-DIB connection.

Our detection of DCBs at 4428 and 5780 Å in an environment rich in fullerenes and fullerene-related molecules would inevitably provide a link between fullerene compounds and the DIB carriers. Photo-absorption theoretical models of several large fullerenes (such as C_{80}, C_{240}, C_{320}, and C_{540}) and multi-shell fullerenes (carbon onions like $C_{60}@C_{240}$, $C_{60}@C_{240}@C_{540}$) predict their strongest optical (4000−7000 Å) transitions very close to 4428 and 5780 Å (Iglesias-Groth 2007), suggesting they are possible carriers.

We can estimate abundances of the carriers of the DCBs at 4428 and 5780 Å in PN Tc 1. For a Tc 1 carbon abundance of 4.7×10^{-4} (relative to H; e.g., García-Hernández et al. 2012b), the fraction of elemental carbon (f_C) that is locked in the carrier molecule M can be expressed as (see, e.g., Tielens 2005; Cami 2014)

$$f_C \sim 9.93 \times 10^{-3} \times \frac{W_\lambda}{E_{B-V}} \times \frac{N_C}{60} \times \frac{5000^2}{\lambda^2} \times \frac{10^{-2}}{f},$$

where W_λ/E_{B-V} is the equivalent width per reddening unit (in Å magnitude^{-1}), N_C is the number of carbon atoms, and λ and f are the transition wavelength (in Å) and oscillator strength, respectively.

Assuming f=0.01[12] (Watson 1994; Weisman et al. 2003) and $N_C \geq 60$ (as appropiate for large fullerenes and buckyonions), we find the well known result that the 4428 and 5780 Å carriers have to be very abundant or else they have larger oscillator strengths (Tielens 2005). For example, $f_C \sim 0.06$, 0.19, and 0.42 for C_{80}, C_{240}, and C_{540}, respectively, if these fullerene species are considered to be the only carrier of the 4428 Å feature[13]. In Tc 1, the fraction of elemental carbon that is locked in C_{60} is estimated to be $\sim 4 \times 10^{-4}$ (as estimated from the IR emission; e.g., García-Hernández et al. 2012b). However, most fullerenes bigger than C_{60} and multi-shell fullerenes (buckyonions) display strong transitions close to 4428 Å (Iglesias-Groth 2007). Thus, in the fullerene-DIB hypothesis, the broad 4428 Å feature would be the result of the superposition of the transitions of a series (family) of fullerenes bigger than C_{60} and buckyonions, and each fullerene compound would contribute to the total EQW observed. Unfortunately, at present the possible relative contribution (e.g., in terms of FWHM and EQW) of these fullerene compounds to the 4428 Å feature is not known.

More interesting is that only C_{540} and $C_{60}@C_{240}@C_{540}$ display a strong transition near 5780 Å (Iglesias-Groth 2007). By considering the latter fullerene species (and using f=0.01) as the only carrier of the 5780 Å feature, $f_C \sim 2\times10^{-3}$ and 3×10^{-3} are obtained for C_{540} and $C_{60}@C_{240}@C_{540}$, respectively. Thus, a greater oscillator strength (e.g., f=0.1) for the C_{540} and $C_{60}@C_{240}@C_{540}$ transitions at 5780 Å would decrease the latter estimates to levels similar to C_{60}.

[12] This is a typical oscillator strength for molecular electronic transitions.

[13] $f_C \sim 0.05$, 0.16, and 0.37 for M 1-20 and $\sim$0.07, 0.22, and 0.50 for IC 418, respectively.

On the other hand, it is to be noted here that the C_{60} abundance estimation in Tc 1 (e.g., García-Hernández et al. 2012b) assumes a uniform C_{60} spatial distribution in the circumstellar shell. Bernard-Salas et al. (2012) present evidence that the C_{60} emission in Tc 1 is extended and peaks far away from the central star. If the C_{60} molecules in Tc 1 are indeed distributed in a ring (or in clumps) around the central star (see Chapter 4), then the quoted C_{60} abundance of $\sim$4 $\times$ 10^{-4} (relative to C; e.g., García-Hernández et al. 2012b) should be considered as a lower limit. The distribution of fullerenes in a shell of R_{out}=9700 au and R_{in}=6400 au, may increase the C_{60} abundance estimate (from the IR emission) in Tc 1 to values higher than the 5780 Å carrier/s abundance estimated here. In addition, it may explain the lack of the strongest optical electronic transitions of the C_{60} molecule in Tc 1 (and IC 418; see Bernard-Salas et al. 2012 and García-Hernández & Díaz-Luis 2013 for more details).

From the previous paragraghs, we conclude that at present large fullerenes and buckyonions cannot be completely discarded as possible carriers of the 4428 and 5780 Å features. However, another fullerene-related species should be considered as possible diffuse band carriers (see below).

Recent experimental studies demonstrate that fullerenes (and metallofullerenes; see Chapter 1, Section 1.2) would react with polycyclic carbon, graphene-like structures, and PAHs, forming a rich family of fullerene-based molecules such as fullerene/PAH clusters and endohedral metallofullerenes (Dunk et al. 2013). These fullerene-related species may still be excited by the UV photons from the central star, emitting through the same IR vibrational modes as empty cages. Laboratory work shows that fullerene/PAH adducts (such as C_{60}/anthracene) can easily form via Diels-Alder cyclo-addition reactions, displaying mid-IR features strikingly coincident with those from neutral C_{60} and C_{70} (García-Hernández et al. 2013). In addition, gas-phase reactions between PAHs and C_{60} and C_{70} are experimentally proven to occur under circumstellar/interstellar conditions (Dunk et al. 2013), and the resulting reaction products (e.g., C_{70}-PAH cluster ions like $C_{70}C_{24}H_{10}{}^{+}$) are very stable. Metals such as Na (and Ca) are also quite abundant in the fullerene-rich circumstellar envelope of Tc 1 and metallofullerene (e.g., Na@C_{60}) formation is expected to be as efficient as empty fullerenes (Dunk et al. 2013). Indeed, theoretical spectra of Na@C_{60} (Dunk et al. 2013) show the same four vibrational modes as neutral C_{60} (but with much higher absorption intensities), together with a new IR-active

vibrational mode due to the metal encapsulation. Interestingly, the wavelength position of this new mode is quite close to the still unidentified $\sim$6.4 μm feature observed in Tc 1 and other fullerene-rich PNe (Bernard-Salas et al. 2012; Dunk et al. 2013; García-Hernández et al. 2011a, 2010, 2012b).

Certainly, metallofullerenes are better diffuse band carrier candidates than fullerene/PAH adducts because the latter species are less stable towards UV radiation (see, e.g., Kroto & Jura 1992). In particular, adducts of C_{60} with linearly condensed PAHs (acenes such as anthracene, tetracene, and pentacene; e.g., García-Hernández et al. 2013) are not as stable as those with pericondensed PAHs (e.g., coronene); under the action of strong UV radiation (e.g., from the central star), the C_{60}/acene adducts may be dissociated back to the starting molecules. However, if the C_{60}/acene adducts are formed in a circumstellar region shielded from the UV radiation (or they are absorbed by dust particles), then they could survive in PNe circumstellar shells.

In short, fullerenes in their multifarious manifestations - buckyonions, fullerene clusters, fullerenes-PAHs, metallofullerenes, fullerene-like fragments or buckybowl structures - may help solve the long-standing astrophysical problem of the identification of some of the DIB carriers. Our detection of DCBs at 5780 and 4428 Å in Tc 1 may thus help to identify the carrier molecule(s), so more theoretical/laboratory work on fullerene-related molecules is encouraged.

2.7 Conclusions

- We have searched DIBs in the optical spectra towards three fullerene-containing PNe (namely Tc 1, M 1-20, and IC 418). We have identified 20, 12, and 11 DIBs towards Tc 1, M 1-20, and IC 418, respectively. All of these absorption bands are known DIBs as previously reported in the literature.

- Towards Tc 1, the PN with the highest S/N spectrum and a proper comparison star, six of the strongest and well-studied DIBs (i.e., those at 5797, 5850, 6196, 6270, 6379, and 6614 Å), and nine other weaker interstellar features (i.e., those at 5776, 6250, 6376, 6597, 6661, 6792, 7828, 7833, and 8038 Å) are found to be normal for its reddening. This indicates that the carriers of these "normal" DIBs are not particularly overabundant towards

fullerene PNe. The five DIBs at 4428, 5780, 6203, 6284, and 8621 Å are found to be unusually strong in the Tc 1 line of sight. The radial velocities of the 5780, 6203, 6284, and 8621 Å features confirm their insterstellar origin, and the high ionization degree towards Tc 1 suggests that their carriers may be ionized species. The 4428 Å feature, however, seems to be centred at the Tc 1's radial velocity, suggesting a circumstellar origin.

- The situation is less clear for the fullerenes PNe M 1-20 and IC 418, because their spectra are of lower quality than in Tc 1, and their comparison stars seem to map slightly different ISM conditions. In spite of this, the same classification scheme ("normal" versus "unusually strong" DIBs) seems to be applicable towards M 1-20 and IC 418. At least the 4428 Å feature is found to be unusually strong in these objects, as a common characteristic to fullerene PNe.

- The Tc 1's high radial velocity permitted us to search its high-quality optical spectrum for DCBs. Interestingly, we report the first tentative detection of two DCBs at 4428 and 5780 Å in the fullerene-rich circumstellar environment around Tc 1. The presence of 4428 and 5780 Å nebular emission at the radial velocity of Tc 1 further suggests their circumstellar origin. The non-detection of DCBs in the other fullerene PNe is due to the low S/N in our optical spectra.

- Moreover, we can find no evidence of the strongest electronic transitions of neutral C_{60} in the IC 418 optical spectrum. The non-detection of neutral C_{60} optical absorptions in fullerene PNe could be explained if the C_{60} IR emission peaks far away from the central star. Mid-IR images at high spatial resolution and centred on the C_{60} features would be desirable to understand the lack of the C_{60} optical bands in fullerene-containing PNe (see Chapter 4).

- We have estimated the abundances of the carriers of the DCBs at 4428 and 5780 Å, and we conclude that at present large fullerenes and buckyonions cannot be completely discarded as possible carriers of the 4428 and 5780 Å features.

- On the basis of detecting DCBs at 4428 and 5780 Å in Tc 1, we suggest that laboratory and theoretical studies of fullerenes in their multifarious manifestations - buckyonions, fullerene clusters, fullerenes-PAHs,

metallofullerenes, fullerene-like fragments or buckybowl structures - may help solve the astronomical mistery of the identification of some of the DIB carriers.

3

A search for hydrogenated fullerenes in fullerene-containing planetary nebulae

Based on

J. J. Díaz-Luis et al. 2016, A&A, 589, A5

ABSTRACT - Detections of C_{60} and C_{70} fullerenes in planetary nebulae (PNe) of the Magellanic Clouds and of our own Galaxy have raised the idea that other forms of carbon, such as hydrogenated fullerenes (fulleranes like $C_{60}H_{36}$ and $C_{60}H_{18}$), buckyonions, and carbon nanotubes, may be widespread in the Universe. Here we present VLT/ISAAC spectra (R ∼600) in the 2.9-4.1 μm spectral region for the Galactic PNe Tc 1 and M 1-20, which have been used to search for fullerene-based molecules in their fullerene-rich circumstellar environments. We report the non-detection of the most intense infrared bands of several fulleranes around ∼3.4-3.6 μm in both PNe. We conclude that if fulleranes are present in the fullerene-containing circumstellar environments of these PNe, then they seem to be much less abundant than C_{60} and C_{70}. Our non-detections, together with the (tentative) fulleranes detection in the proto-PN IRAS 01005+7910, suggest that fulleranes may be formed in the short transition phase between AGB stars and PNe, but they are quickly destroyed by the UV radiation field from the central star.

3.1 Introduction

Duley & Williams (2011) predict the production of fullerenes via thermal heating of hydrogenated amorphous carbon (HAC) and this process may explain

the detection of fullerenes in H-rich circumstellar environments (e.g., García-Hernández et al. 2010). Interestingly, they also predict the formation of hydrogenated fullerenes (fulleranes). On the other hand, Iglesias-Groth et al. (2012) found that the 3.44 and 3.55 μm bands of several fulleranes display molar extinction coefficients[1] that are similar to those of the 17.4 and 18.8 μm bands of the isolated C_{60} molecule (Iglesias-Groth et al. 2011). Thus, it could be reasonable to find fulleranes with line intensities similar to the ones already measured with *Spitzer* at 17.4 and 18.8 μm in fullerene-containing PNe. Indeed, Zhang & Kwok (2013) have tentatively detected fulleranes in the Infrared Space Observatory (ISO) spectrum of the proto-PN IRAS 01005+7910, where three emission peaks at ∼3.48, 3.51, and 3.58 μm in the C-H stretching region seem to be present.

More recently, several fullerene-based molecules, like fullerene/PAH adducts, have been synthesized and characterized in the laboratory (e.g., García-Hernández et al. 2013; Cataldo et al. 2014, 2015). Remarkably, fullerene/PAH adducts such as C_{60}/anthracene display mid-IR ($\lambda > 5$ μm) spectral features that are strikingly coincident with those from C_{60} and C_{70} (García-Hernández et al. 2013) and it is still no clear if these species could contribute to the observed C_{60} (and C_{70}) features in fullerene-rich environments. Laboratory spectra of C_{60}/anthracene adducts display the typical aromatic bands around 3.3 μm, as well as aliphatic C−H bands at ∼3.39, 3.43, and 3.52 μm, which are not present in the C_{60} and C_{70} spectra. In principle, this could be used to elucidate the possible carrier (e.g., C_{60} versus C_{60}/PAH adducts) of the mid-IR features seen in fullerene PNe. However, the C−H stretching bands are intrinsically weaker than the other emission features at longer wavelengths and the presence of these C−H stretching bands (typical for CH_2 and CH_3 groups of several carbonaceous materials) is not yet completely understood (García-Hernández et al. 2013), which complicates the search of these fullerene-related species in space.

In this chapter we present VLT/ISAAC spectroscopy (the 2.9-4.1 μm spectral region) of two PNe with fullerenes (Tc 1 and M 1-20). An overview of the spectroscopic observations is presented in Section 3.2; together with a summary of the nebular emission lines observed. Section 3.3 presents a brief discussion of the detection of the 3.3 μm unidentified infrared emission (UIR) feature in

[1]The molar extinction coefficient is a measure of how strongly a substance absorbs light at a particular wavelength (see e.g., Iglesias-Groth et al. 2011).

our VLT/ISAAC spectrum of M 1-20 and its possible carriers. Section 3.4 discusses the non-detection of infrared emission bands (e.g., from fulleranes) in our spectra. The conclusions of our work are given in Section 3.5.

3.2 Mid-IR spectroscopic observations

We acquired 3-4 μm infrared (IR) spectra of the fullerene PNe Tc 1 (W1 $[3.35\mu\mathrm{m}]_{WISE}$=8.19, E(B-V)=0.23; Cutri et al. 2012; Williams et al. 2008) and M 1-20 (W1 $[3.35\mu\mathrm{m}]_{WISE}$=9.65, E(B-V)=0.80; Cutri et al. 2012; Wang & Liu 2007) with a S/N (at the continuum in the final IR spectra) of $\sim$26 and 11, respectively. Tc 1 displays a fullerene-dominated spectrum with no clear signs of PAHs, while M 1-20 also shows weak PAH-like features (see, e.g., García-Hernández et al. 2010). Table 3.1 lists some observational parameters such as Galactic coordinates, color excess and radial velocity for the corresponding telluric/flux stars for Tc 1 and M 1-20, respectively (Table 2.1 in Chapter 2 shows the observational parameters for the two PNe).

The observations of Tc 1, M 1-20, and their corresponding telluric/flux standards (HR 7446 and HIP 92519, respectively) were carried out at the ESO VLT (Paranal, Chile) with ISAAC in service mode between 14-23 July 2013. We used the LWS-LR/3550 nm set-up with the 0.6" slit oriented at a position angle of 0°. This configuration covers the spectral range 2.9-4.1 μm and gives a resolving power of $\sim$600, which is required to cleanly separate the 3-4 μm features of several fullerene-based molecules as seen in the laboratory. During the observations, the seeing was about 0.5-0.6 and 1.5-1.7 arcsec for Tc 1 and M 1-20 (and their corresponding standards), respectively.

Table 3.1: Observational parameters of fullerene PNe and their comparison stars.

Telluric/flux star	l	b	SpT	V_r	Ref [a]
HR 7446	31.7709	−13.2866	B0.5III	−19.4	1, 2
HIP 92519	351.7764	−18.6123	G0V	70.9	1, 3

[a] References. (1) de Bruijne & Eilers (2012); (2) Wegner (2003); (3) Soubiran et al. (2013).

The spectra were obtained combining the chopping technique (moving the secondary mirror of the telescope once every few seconds) with telescope nodding. We used a total integration time of 38 min for each observing block (OB). For Tc 1, we obtained three OBs of 26 individual exposures each, giving a total exposure time on target of ∼1.9 h, and for M 1-20, one OB of 26 individual exposures and ∼38 min on-target exposure time. Raw spectra were processed by the ISAAC data reduction pipeline[2] in conjunction with the data browsing tool GASGANO[3]. In short, i) flat-fields are combined to produce a master flat-field; ii) the wavelength calibration and ISAAC slit curvature distortion is computed using OH sky lines; and iii) the removal of the high degree of curvature of ISAAC spectra is performed by calculating the spectra curvature using a star moving across the slit. Thus, science frames were reduced using the products of the pipeline calibration recipes. The produced 2D image for each PN is then used to extract the one-dimensional spectrum across the defined apertures with IRAF. We note that the continuum emission is not extended in both PNe but, to cover the nebular hydrogen lines in the 2D images, we needed to define an aperture of 78 and 10 pixels for Tc 1 and M 1-20, which translate (scale of 0.15 arcsec/pixel) into nebular extensions of ∼11.5 and ∼1.5 arcsec, respectively. We also defined other apertures, but these were the best extractions for our goal. Finally, the extracted spectra were combined to produce a final, reduced science spectrum. This process was also done for the telluric stars, which are also used for flux calibration (see below).

We used the telluric stars to determine the sensitivity and extinction functions to flux calibrate our science spectra with standard tasks in IRAF. The *standard* task makes a comparison between the fitted continuum of the standard stars and the fluxes for a set of bandpasses. We assumed that the two stars behave approximately like black bodies. There are two parameters needed to scale the black body to the observation: the magnitude of the star in the same band as the observation (L band at 3.4 μm) and the effective temperature. We used the WISE magnitudes (W1 at 3.35 μm) of 5.030 and 6.239 mag (Cutri et al. 2013), and effective temperatures (T_{eff}) of 26654 and 6196 K (Delgado Mena et al. 2015; Huang & Gies 2008) for HR 7446 and HIP 92519, respectively. The output data are then used by the task *sensfunc* to determine the detector sensitivity and extinction functions, and the task *calibrate* applies them to our

[2]https://www.eso.org/sci/software/pipelines/isaac/isaac-pipe-recipes.html
[3]https://www.eso.org/sci/software/gasgano.html

science spectra. The estimated flux errors are approximately 30-40 %. Finally, telluric correction was made using the telluric star for each PN, which were observed very close in time and position to our science targets, and the task *imarith*. It is worth noting that the wavelength positions need to be carefully checked before dividing the images.

3.2.1 Nebular emission lines

In this section, we give an overview of the nebular emission lines that were observed in the 2.9 to 4.1 μm region. This spectral range is dominated by nebular emission lines of hydrogen.

Our list of features in Tc 1 and M 1-20 is shown in Table 3.2, where we give the measured central wavelength (λ_c), the full width at half maximum (FWHM), the equivalent width (EQW), and the integrated flux[4].

Table 3.2: Nebular emission lines identified in the 2.9-4.1 μm spectra of M 1-20 and Tc 1.

	M 1-20			Tc 1		
Element	λ_c (μm)	FWHM ($10^{-4}\,\mu$m)	FLUX [a] ($10^{-15}\,\mathrm{erg\,cm^{-2}\,s^{-1}}$)	λ_c (μm)	FWHM ($10^{-4}\,\mu$m)	FLUX [a] ($10^{-15}\,\mathrm{erg\,cm^{-2}\,s^{-1}}$)
H I (Pf_ϵ)	3.07	43.68	4.20			
UIR	3.31	536.10	17.20			
H I (Pf_δ)	3.32	41.05	6.49	3.30	37.88	0.28
H I (Pf_γ)	3.75	45.96	5.74	3.74	47.32	0.43
H I (6-17)	3.76	40.95	0.33	3.75	42.43	0.03
H I (6-15)	3.91	40.45	0.54	3.90	37.77	0.04
He I (4-5)	4.04	25.01	0.86	4.04	43.17	0.11
H I (Br_α)	4.05	47.59	46.70	4.05	48.48	3.49

[a] Estimated flux errors are of the order of ∼30%-40%.

The M 1-20 spectrum includes the atomic hydrogen lines Pf_ϵ at 3.07 μm, a blend of the UIR feature at 3.31 with Pf_δ at 3.32 μm, Pf_γ at 3.75 μm, and Br_α at 4.05 μm. It also includes the tentatively identified H I (6-17), H I (6-15), and He I (4-5) lines at 3.76, 3.91, and 4.04 μm, respectively. In Figure 3.1, we display the M 1-20 spectrum in the 2.9-4.1 μm range.

[4]The feature parameters were measured with IRAF by assuming a Gaussian profile.

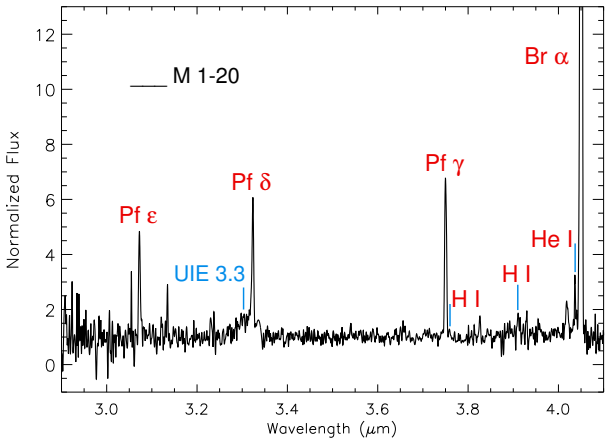

Figure 3.1: VLT/ISAAC spectrum of PN M 1-20. The atomic H lines of the Pfund series (Pf_ϵ, Pf_δ and Pf_γ), H I (6-17), H I (6-15), and Br_α, as well as the UIR feature at 3.3 μm and the line of He I (4-5), are indicated.

The Tc 1 spectrum includes the atomic hydrogen lines Pf_δ, Pf_γ, the tentatively identified H I (6-17) and H I (6-15) lines and Br_α. It also includes the tentative He I (4-5) line at 4.04 μm. In Figure 3.2, we display the Tc 1 2.9-4.1 μm spectrum.

3.3 The 3.3 μm UIR feature

We clearly detect the 3.3 μm UIR feature in M 1-20, while this feature is completely lacking in Tc 1. This is consistent with the *Spitzer* spectra; M 1-20 displays UIR features (PAH-like) at 6.2, 7.7, 8.6, and 11.3 μm, but these are absent in Tc 1 (e.g., García-Hernández et al. 2010). The detected UIR feature in the M 1-20 spectrum was fitted with a Gaussian to determine the feature's FWHM and central wavelength. Owing to the emission line of H I (Pf_δ) at 3.32 μm, it was necessary to deblend both features. The average central wavelength of the UIR feature was 3.31 μm, with a FWHM of 0.05 μm. This is consistent with the values measured by Tokunaga et al. (1991) and Smith & McLean

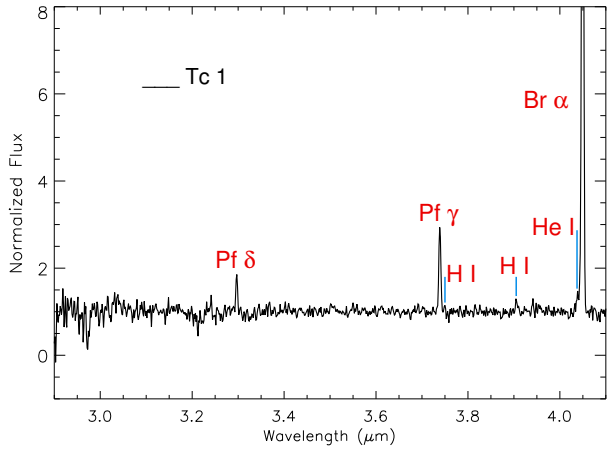

Figure 3.2: VLT/ISAAC spectrum of Tc 1. The atomic H lines of the Pfund series (Pf_{δ} and Pf_{γ}), H I (6-17), H I (6-15), and Br_{α}, as well as the line of He I (4-5), are indicated.

(2008) (average values of λ_c ~3.29 μm and FWHM ~0.04 μm) in extended objects such as PNe, (proto-) PNe, and H II regions. In Figures 3.1 and 3.3, we can see the 3.3 μm UIR feature in the M 1-20 spectrum blended with the Pf_{δ} hydrogen emission line at 3.32 μm.

3.3.1 Possible carriers

The 3.3 μm feature belongs to the group of UIR features or aromatic infrared bands (AIBs) at 3.3, 6.2, 7.7, 8.6, 11.3, and 12.7 μm. Moreover, the 11.3 μm UIR feature is found to be correlated with the 3.3 μm feature (Russell et al. 1977), which suggests a common origin for the two features. This correlation holds for fullerene PNe; we detect the weak UIR feature at 3.3 μm in our VLT/ISAAC spectrum and the M 1-20 *Spitzer* spectrum shows a very strong aromatic-like infrared band at 11.3 μm (García-Hernández et al. 2012b), while Tc 1 displays a very weak emission at 11.3 μm and it does not show the feature at 3.3 μm.

A wide variety of molecules have been proposed as possible carriers of these

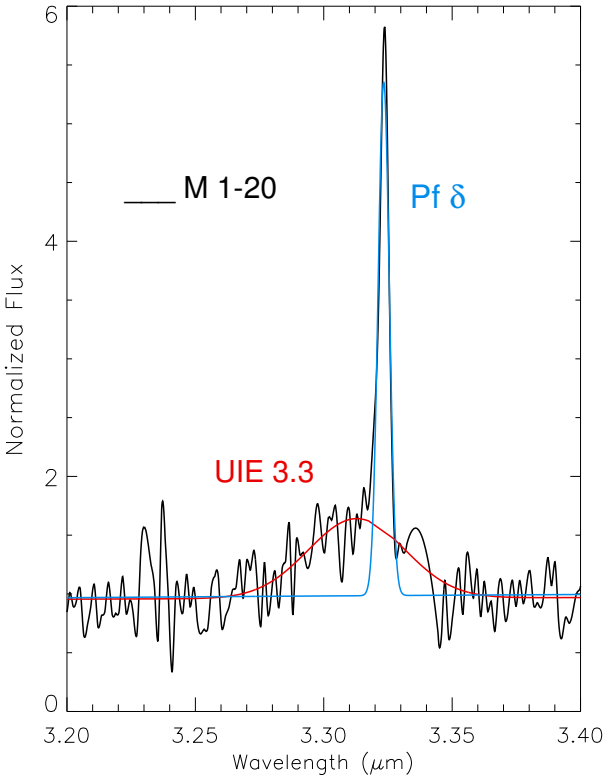

Figure 3.3: VLT/ISAAC spectrum of M 1-20 in the 3.2-3.4 μm range (in black) showing the weak UIR feature at 3.31 μm and the Pf$_\delta$ hydrogen line at 3.32 μm. The red and blue lines show the Gaussian fits to the UIR and Pf$_\delta$ features, respectively.

3.3 and 11.3 μm UIR bands. Currently, the most accepted idea is that they originate from the C-H vibration modes of aromatic compounds or PAHs (e.g., Allamandola et al. 1985; Duley & Williams 1981; Leger & Puget 1984). However, Sadjadi et al. (2015) calculated the out-of-plane (OOP) bending mode frequencies of 60 neutral PAH molecules and found that it is difficult to fit the

11.3 μm UIR feature. This feature cannot be fitted by superpositions of pure PAH molecules, and O- (and or Mg-) containing species are needed to achieve a good fit, suggesting that the PAHdb model (Bauschlicher et al. 2010; Boersma et al. 2014) has problems explaining the UIR phenomenon. On the other hand, they suggest that the MAON-like structures have consistent clusters of vibrational bands and are good candidates for being the carriers of the UIR bands (see Section 1.4 in Chapter 1 and Sadjadi et al. 2015 for more details). Maltseva et al. (2015) also found difficulties for predicting high-resolution experimental absorption spectra of PAHs in the 3 μm region with harmonic density functional theory (DFT[5]) calculations. However, their anharmonic DFT calculations work well for small PAHs in this spectral region, opening the way to predict the spectrum of larger PAHs (and other hydrocarbons). Finally, Gadallah et al. (2013) also found that the 3.3 μm and 6.2 μm AIBs are also clearly observed in the spectrum of heated HAC dust.

On the other hand, Duley & Williams (2011) suggest a model in which the astronomical emission at 3.3 μm can be explained by the heating of HAC dust via the release of stored chemical energy. This energy could be sufficient to heat dust grains (with sizes of ∼50-1000 Å) to temperatures at which they can emit at 3.3 μm. This alternative to the PAH hypothesis involves a solid material with a mix of aliphatic and aromatic structures (i.e., HACs), which may explain the broad emission features at ∼6-9, 9-13, 15-20, and 25-35 μm detected in PNe with fullerenes (García-Hernández et al. 2010, 2012b) and most C-rich proto-PNe. Moreover, laboratory experiments show that the products of destruction of HAC grains are PAHs and fullerenes (Scott et al. 1997), something that could explain the detection of both types of molecules in some fullerene PNe (García-Hernández et al. 2010). Unfortunately, our VLT/ISAAC observations do not add much information about the real carrier (e.g., PAHs vs. HACs) of the 3.3 μm emission. The non-detection of 3.3 μm emission in Tc 1 may suggest a different spatial distribution of the 3.3 μm carrier and the C_{60} (and C_{70}) fullerenes. Bernard-Salas et al. (2012) already found that the *Spitzer* C_{60} 8.5 μm and weak 11.2 μm emission (which likely share the same carrier with the 3.3 μm emission, see above) are extended, but they peak at opposite directions

[5]Density functional theory is often used to predict the vibrational spectra of molecules. Harmonic only allows the fundamental transitions, while anharmonic allows the fundamental transitions, as well as overtones and combinations.

from the Tc 1 central star[6]. The *Spitzer* observations (slit of ∼4" x 57" at a P.A. of 0 degrees) show extended emission up to ∼22" (Bernard-Salas et al. 2012), while our VLT/ISAAC spectra, taken with a smaller slit of 0.6 arcsec, show no extended emission at 3.3 μm. Thus, it could be possible that we are missing the weak 3.3 μm emission in the ISAAC observations (e.g., a small column density throughout the circumstellar envelope). In the case of the more compact (apparent size of ∼2 arcsec) PN M 1-20, we have no spatial information from the *Spitzer* spectra (which covered the entire nebula) and the 3.3 μm emission in the VLT/ISAAC spectra is not extended.

In short, it is still not clear if the emission bands at 3.3 and 11.3 μm seen in PNe with fullerenes are only due to pure aromatic compounds or to mixed aromatic/aliphatic structures, such as those of HAC-like dust.

3.4 Non-detection of the fullerane features

The IR laboratory spectra (R∼500) of several fulleranes, such as $C_{60}H_{18}$, $C_{60}H_{36}$, or $C_{70}H_{38}$ (Iglesias-Groth et al. 2012), show that the strongest features in the mid-IR (2-20 μm) are those at ∼3.44, 3.51, and 3.54 μm[7] (see Figure 3.4), being the best IR bands for searching these molecules in the circumstellar environments of fullerene-rich PNe. Thus, at the resolution (R∼600) of the VLT/ISAAC observations, it is possible to easily resolve these bands, as well as to distinguish them from the 3.3 μm emission (Iglesias-Groth et al. 2012). However, none of these three emission features is detected in our VLT/ISAAC spectra of Tc 1 and M 1-20. Figure 3.4 shows the non-detection of the fullerane features between 3.4 and 3.6 μm in our VLT/ISAAC spectra of Tc 1 and M 1-20. The laboratory spectra of the fulleranes $C_{60}H_{18}$, $C_{70}H_{38}$, and $C_{60}H_x$+$C_{70}H_y$ (see below) are also displayed and their corresponding 3.4-3.6 μm features are indicated.

We could estimate approximate upper limits to the fluxes of the hydrogenated fullerene features (see Table 3.3). To obtain 2σ upper limits (due to their weakness) to the expected emission line fluxes of the fullerane features at

[6]Sellgren et al. (2010) reported a similar separation in the spatial distribution of the fullerene and PAH emission seen in the fullerene-containing reflection nebula NGC 7023.

[7]Fulleranes do not emit at 3.3 μm because they lack sp^2-bonded CH groups (see Figure 3.4).

$\sim$3.5 μm, we measure the rms in our flux-calibrated VLT/ISAAC spectra; rms values of $\sim 4.28 \times 10^{-19}$ erg cm^{-2} s^{-1} Å^{-1} and $\sim 6.65 \times 10^{-18}$ erg cm^{-2} s^{-1} Å^{-1} for Tc 1 and M 1-20 are obtained, respectively. Then we multiply these values by the widths (FWHMs in the range 0.02-0.10 μm) of the fullerane bands, as measured in the infrared laboratory spectra[8]. We used the laboratory spectra of two $C_{60}H_{18}$ isomers (that were obtained using hydrogen iodide and direct hydrogenation with metal hydrides), two $C_{60}H_{36}$ spectra at +48°C and +250°C, two $C_{70}H_{38}$ spectra at +50°C and +160°C, and the fullerane mixture 77 % of $C_{60}H_x$ and 22 % $C_{70}H_y$ with x $\approx$ y $\geq$ 30 at +45°C (see Iglesias-Groth et al. 2012 for more details). Finally, we divided these fluxes by the area ($\sim$0.6 arcsec^2 for both PNe since it is not an extended emission) of the emission in the 3$-$4 μm range covered by our ISAAC observations.

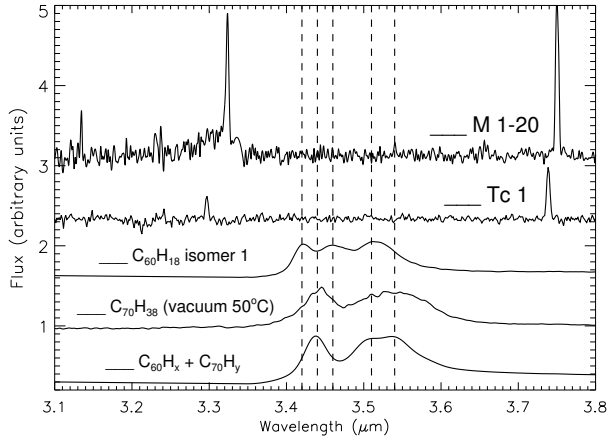

Figure 3.4: VLT/ISAAC spectra of M 1-20 and Tc 1, in comparison with the laboratory spectra of the fulleranes $C_{60}H_{18}$, $C_{70}H_{38}$, and $C_{60}H_x$+$C_{70}H_y$ in the 3.1-3.8 μm range. Note that the $C_{60}H_{18}$ fullerane bands at 3.42, 3.46, and 3.51 μm and the $C_{70}H_{38}$ fullerane bands at 3.44 and 3.54 μm are marked with dashed lines. The $C_{60}H_x$+$C_{70}H_y$ fullerane bands are those at 3.44, 3.51, and 3.54 μm.

[8]Note that Zhang & Kwok (2013) measured similar FWHMs (in the range $\sim$0.02-0.04 μm) for the posssible fullerane bands seen in the ISO spectrum of IRAS 01005+7910.

On the other hand, by using the molar absorptivity values for the fullerenes and fulleranes that have been reported by Iglesias-Groth et al. (2011, 2012), we can estimate the predicted fluxes for the fullerane features in Tc 1 and M 1-20[9] (see Table 3.3). By taking the molar absorptivity ratio (e.g., $\epsilon_{C60}/\epsilon_{fulleranes}$) of the fullerene and fullerane bands and the observed fluxes of the C_{60} and C_{70} infrared bands that were less contaminated by other species (García-Hernández et al. 2012), we estimate the expected flux of the fullerane features at ∼3.5 μm. We note that this is only an approximation and a complete model for the excitation/emission of both species is needed. The *Spitzer* integrated fluxes of the infrared bands at 8.5 and 17.4 μm (C_{60}), and 14.9 μm (C_{70}) are taken from García-Hernández et al. (2012) and converted to flux arcsec^{-2} by considering the area covered by the fullerenes emission in the *Spitzer* spectra of Tc 1 (∼80 arcsec^2 at 8.5 μm and ∼53 arcsec^2 at 14.9 and 17.4 μm) and M 1-20 (∼4 arcsec^2 at 8.5, 14.9, and 17.4 μm).

Table 3.3 shows some examples of the estimated 2σ upper limits and the predicted fluxes for the fullerane bands. For example, the molar absorptivity ratio of the $C_{60}H_{36}$ band at 3.44 μm and the C_{60} infrared band at 8.5 μm is $\epsilon_{8.5}/\epsilon_{3.44}$∼0.34. Thus, the expected flux of the $C_{60}H_{36}$ band at 3.44 μm in Tc 1 and M 1-20 would be $\sim 22.13 \times 10^{-14}$ erg cm^{-2} s^{-1} arcsec^{-2} and $\sim 5.58 \times 10^{-13}$ erg cm^{-2} s^{-1} arcsec^{-2}, respectively (see Table 3.3). Similar values are obtained for the fullerane $C_{60}H_{36}$ band at 3.54 μm, with expected fluxes of $\sim 16.23 \times 10^{-14}$ erg cm^{-2} s^{-1} arcsec^{-2}, and $\sim 4.11 \times 10^{-13}$ erg cm^{-2} s^{-1} arcsec^{-2} in Tc 1 and M 1-20, respectively. In summary, the expected fluxes for all fullerane bands of $C_{60}H_{18}$, $C_{60}H_{36}$, $C_{70}H_{38}$, and the mixture $C_{60}H_x$+$C_{70}H_y$ (by using the observed *Spitzer* fluxes of the C_{60} 8.5 and 17.4 μm and C_{70} 14.9 μm bands) are in the range of ∼1.7-30 $\times 10^{-14}$ and ∼1.4-5.6 $\times 10^{-13}$ erg cm^{-2} s^{-1} arcsec^{-2} in Tc 1 and M 1-20, respectively (see Table 3.3 for some representative examples).

By comparing the values of the predicted fluxes with our 2σ upper limits (Table 3.3), we find that the expected fluxes are a factor of ∼20−1000 and ∼10−100 higher than the 2σ upper limits for Tc 1 and M 1-20, respectively. From these estimations, we thus conclude that if fulleranes are present in Tc 1 and M 1-20, then they seem to be much less abundant than C_{60} and C_{70}.

[9]The molar absorptivities of fullerenes and fulleranes are determined with the same standard procedure (Iglesias-Groth et al. 2011, 2012) and we used them to estimate the predicted fluxes.

Table 3.3: Summary table showing examples of the expected fluxes for the fullerane features. Quoted values are the measured central wavelengths of the fullerane features, the full widths at half maximum (FWHM), the 2σ upper detection limits to the expected emission line fluxes in Tc 1 and M 1-20, and the predicted fluxes for the fullerane bands.

Fullerane	λ_c (μm)	FWHM (10^{-2} μm)	FLUX [a](Tc 1) (10^{-16} erg cm^{-2} s^{-1} arcsec^{-2})	Predicted fluxes (Tc 1) (10^{-14} erg cm^{-2} s^{-1} arcsec^{-2})	FLUX [a](M 1-20) (10^{-15} erg cm^{-2} s^{-1} arcsec^{-2})	Predicted fluxes (M 1-20) (10^{-13} erg cm^{-2} s^{-1} arcsec^{-2})
$C_{60}H_{18}$ (isomer 1)	3.42	2.1	$\leq$3.00	9.43 [b]	$\leq$4.65	2.39 [b]
	3.46	3.6	$\leq$5.13	10.20 [b]	$\leq$7.98	2.58 [b]
	3.51	5.1	$\leq$7.28	13.25 [b]	$\leq$11.30	3.36 [b]
$C_{60}H_{18}$ (isomer 2)	3.42	2.2	$\leq$3.13	12.74 [c]	$\leq$4.87	1.42 [c]
	3.45	3.4	$\leq$4.85	13.92 [c]	$\leq$7.53	1.56 [c]
	3.51	5.5	$\leq$7.85	18.21 [c]	$\leq$12.18	2.06 [c]
$C_{60}H_{36}$ (+48°C)	3.44	2.3	$\leq$3.33	22.13 [b]	$\leq$5.18	5.58 [b]
	3.54	7.7	$\leq$11.02	16.23 [b]	$\leq$17.10	4.11 [b]
$C_{60}H_{36}$ (+250°C)	3.44	2.2	$\leq$3.10	30.11 [c]	$\leq$4.80	3.39 [c]
	3.53	10.1	$\leq$14.38	22.08 [c]	$\leq$22.33	2.47 [c]
$C_{70}H_{38}$ (+50°C)	3.44	2.5	$\leq$3.62	18.13 [b]	$\leq$5.63	4.61 [b]
	3.54	7.0	$\leq$10.05	16.75 [b]	$\leq$15.62	4.22 [b]
$C_{70}H_{38}$ (+160°C)	3.44	2.5	$\leq$3.55	1.81 [d]	$\leq$5.52	2.72 [c]
	3.54	6.3	$\leq$8.97	1.68 [d]	$\leq$13.93	2.56 [c]
$C_{60}H_x$+$C_{70}H_y$ (+45°C)	3.44	2.2	$\leq$3.13	20.13 [b]	$\leq$4.87	5.08 [b]
	3.51	2.8	$\leq$4.00		$\leq$6.20	
	3.54	2.5	$\leq$3.57	18.71 [b]	$\leq$5.53	4.75 [b]

[a] Estimated flux errors are ~30%-40%.
[b] Flux prediction obtained by taking the observed flux of the C_{60} feature at ~8.5 μm.
[c] Flux prediction obtained by taking the observed flux of the C_{60} feature at ~17.4 μm.
[d] Flux prediction obtained by taking the observed flux of the C_{70} feature at ~14.9 μm.

As we mentioned above, thermal heating via chemical reactions internal to HAC dust may explain the detection of fullerenes in the H-rich circumstellar environments of PNe, which could potentially form fulleranes (Duley & Williams 2011). In addition, Duley & Hu (2012) reported that laboratory spectra of HAC nano-particles that contain fullerene precursors (or proto-fullerenes; PFs), but not C_{60}, display the same set of mid-IR features as the isolated C_{60} molecule. They suggest an evolutionary sequence for the conversion of HAC to fullerenes, in which initial HAC de-hydrogenation is followed by PF formation and subsequent conversion of PFs to closed cage structures such as C_{60}. Under the Duley & Hu (2012) scenario, Tc 1 would represent the last stage in the HAC de-hydrogenation process (i.e., only fullerenes are present), while the proto-PN IRAS 01005+7910 would represent an intermediate stage where the PFs are being converted to fullerenes. Of note, fulleranes may also be by-products of this conversion from HAC to fullerenes (Duley & Hu 2012).

Interestingly, Zhang & Kwok (2013) have (tentatively) detected fulleranes in the proto-PN IRAS 01005+7910; three strong C-H stretching bands at 3.48, 3.51, and 3.58 μm are apparently present in its ISO spectrum with fluxes that are comparable to the one of the 3.3 μm feature. By assuming that all features have the same oscillator strength, they conclude that the calculated relative strengths indicate that the m value (degree of hydrogenation of the fulleranes $C_{60}H_m$) may lie within the range from 25-40, which is consistent with the production of $C_{60}H_{36}$ (the dominant product of the hydrogenation reaction of C_{60}; e.g., Cataldo & Iglesias-Groth 2009)[10]. In addition, the observed fluxes of the C_{60} and fullerane bands suggest that about 50 percent of fullerenes have been hydrogenated. Curiously, IRAS 01005+7910 displays exceptionally strong C_{60}^+ DIBs (Iglesias-Groth & Esposito 2013).

Our non-detection of fulleranes in more evolved PNe (such as Tc 1 and M 1-20 with $T_{eff}>$ 30,000 K) together with their possible detection in less evolved sources (like IRAS 01005+7910 with $T_{eff}\sim$21,500 K) thus suggest that fulleranes may be formed in the short transition phase between AGB stars and PNe but they are quickly destroyed; e.g., they are photochemically processed by the rapidly changing UV radiation from the central star. The rapid increase of the UV radiation towards the PN stage will easily break the C−H bonds of the previously formed fullerane molecules, forming fulleranes at lower

[10]Zhang & Kwok (2013) suggest that $C_{60}H_{18}$ might be also present.

hydrogenation degree or reforming - more resistant - C_{60} and C_{70} fullerenes and molecular hydrogen (Cataldo & Iglesias-Groth 2009). Recent DFT calculations (Sadjadi 2017), have shown that the strength of fullerane bands in the 3-4 μm range depends on the number of active C−H bonds, thus highly hydrogenated fullerenes should have stronger bands. Therefore, we cannot discard the presence of fulleranes at lower hydrogenation (e.g., $C_{60}H_2$ or $C_{60}H_4$) in our VLT/ISAAC observations. However, it is still not clear what the origin of fulleranes is. Fulleranes could be formed via the Duley & Hu (2012) HAC de-hydrogenation process, mentioned above, in which fulleranes may be by-products from the conversion from PFs to C_{60}, or they could be formed by the reaction of pre-existing fullerenes (e.g., formed by the photochemical processing of HACs; Scott et al. 1997) with atomic hydrogen. During the short ($\sim 10^2$-10^4 years) transition phase, AGB-PN, H_2[11] may be photodissociated into atomic H owing to the gradual increase of the UV radiation field with the evolution of the central star and/or by shocks (H_2 dissociated through collisions) as a result of the fast post-AGB stellar winds. By reacting with atomic hydrogen, fullerenes form fulleranes at various degrees of hydrogenation. Thus, the post-AGB phase could make the reaction between fullerenes and atomic H more favorable (Cataldo & Iglesias-Groth 2009) and it seems to provide the right conditions for the formation and detection of fulleranes.

3.5 Conclusions

- We have presented VLT/ISAAC 2.9-4.1 μm spectroscopy of two fullerene PNe in our Galaxy. The spectrum of Tc 1 shows a continuum with no signs of UIR features and only H (and He) nebular lines. This indicates that the IR bands seen in the Tc 1 *Spitzer* spectrum are very likely due to C_{60} and C_{70} alone, and not other kinds of molecules, such as fulleranes or fullerene/PAH adducts. The M 1-20 VLT/ISAAC spectrum shows H and He nebular lines in conjunction with the UIR feature at 3.3 μm.

- The VLT/ISAAC and *Spitzer* spectra of these fullerene PNe confirm a correlation between the 3.3 and 11.3 μm UIR features, as previously reported in the literature, which suggests a common carrier for the two features.

[11] The HAC chemical energy model of Duley & Williams (2011) also predicts the release of warm H_2 molecules trapped inside the HAC solid.

Unfortunately, the VLT/ISAAC observations, presented here, cannot reveal the nature of the real carrier (e.g., PAHs vs. HACs) of the 3.3 μm emission.

- Interestingly, we have reported the non-detection of the strongest bands of hydrogenated fullerenes (fulleranes such as $C_{60}H_{18}$, $C_{60}H_{36}$, $C_{70}H_{38}$, and a fullerane mixture) at $\sim$3.44, 3.51 and 3.54 μm in the 3$-$4 μm spectra of the fullerene-containing PNe Tc 1 and M 1-20. From a comparison of the predicted fluxes of the fullerane bands with our 2σ upper limits, we conclude that, if fulleranes are present in both objects, then they seem to be much less abundant than isolated fullerene molecules. Moreover, we cannot discard the presence of fulleranes at lower hydrogenation (e.g., $C_{60}H_2$ or $C_{60}H_4$).

- Our non-detection of fulleranes in two fullerene PNe, together with their possible detection (if real) in the fullerene proto-PN IRAS 01005+7910, suggests that these fullerene-related species may be formed in the short transition phase AGB$-$PN, but they are rapidly destroyed; e.g., by the quick increase of UV radiation from the central star towards the PN stage. The transition between AGB stars and PNe seems to be the best evolutionary stellar phase for finding fulleranes in space and 3$-$4 μm spectroscopy in a larger sample of C-rich proto-PNe is encouraged.

4

Mid-IR imaging of the fullerene-rich planetary nebula IC 418

This chapter will be submitted for publication in ApJ
J. J. Díaz-Luis et al. 2017

ABSTRACT - The C_{60} and C_{70} fullerenes are now known to be efficiently formed only in H-rich circumstellar envelopes. The formation process(es) of fullerenes in space is still uncertain and several mechanisms have been proposed in the literature. Here we present seeing-limited narrow-band mid-IR GTC/CanariCam images of the extended fullerene-containing planetary nebula (PN) IC 418. The narrow-band images cover the C_{60} fullerene band at 17.4 μm, the polycyclic aromatic hydrocarbon (PAH-like) feature at 11.3 μm, and the broad 9-13 μm feature (and their adjacent continua) in this extended PN. We study the relative spatial distribution of these complex species, all detected in the *Spitzer* and *Infrared Space Observatory* spectra of IC 418, with the aim of getting observational constraints to the formation process of fullerenes in H-rich circumstellar environments. A similar ring-like extended structure is seen at all wavelengths, with the exception of the dust continuum emission at 9.8 μm, which peaks closer the central star. The very similar spatial distribution of the IR emission at 17.4 μm (C_{60}; Q1 filter) and the dust continuum emission at 20.5 μm (Q4 filter) already suggests that both Q1 and Q4 filters are likely dominated by the dust continuum emission; which is consistent with the very low C_{60}-to-continuum ratio of IC 418. The continuum-subtracted images display a clear ring-like extended structure for the carrier of the broad 9-13 μm emission, while the spatial distribution of the PAH-like 11.3 μm emission seems to be less well defined. However, only a residual C_{60} 17.4 μm emission (at about 4-σ from the sky background) is seen when subtracting the dust continuum emission at 20.5 μm. This residual C_{60} emission might have several interpretations; the most exciting being perhaps that other

fullerene-based species like hydrogenated fullerenes may contribute to the observed 17.4 μm emission. We conclude that higher sensitivity mid-IR images and spatially resolved spectroscopic observations (e.g., by using the upcoming James Webb Space Telescope) are necessary to get definitive clues about fullerene formation in PNe; especially in the Q-band where the water vapour severely limits the ground-based observations.

4.1 Introduction

The formation process of fullerenes in space is still uncertain and several mechanisms have been proposed in the literature as the most suitable ones: i) the formation in H-poor environments (Goeres & Sedlmayr 1992); ii) high-temperature formation in C-rich environments (Jäger et al. 2009); iii) photochemical processing of hydrogenated amorphous carbon grains (HACs; García-Hernández et al. 2010); and iv) photochemical processing of large PAHs (Berné & Tielens 2012). Hydrogenated species cannot be produced by the first two mechanisms, which is very difficult to reconcile with the astronomical evidence. The two last formation scenarios, involving the photochemical processing of HACs (or similar materials with a mixed aromatic/aliphatic composition; e.g., García-Hernández et al. 2012b) and large PAHs, are based on top-down chemical models toward the most stable C_{60} and C_{70} fullerenes.

The large PAHs top-down formation model to explain the formation of C_{60} in the ISM was proposed by Berné & Tielens (2012). In this model, large PAHs are converted into fullerenes via graphene under UV irradiation from massive stars. A potential problem of the large PAHs scenario above is that, yet to date, no specific gas-phase PAH has been detected in space (see e.g., Tielens 2011 for a review). Zhen et al. (2014) have experimentally studied the photo-fragmentation behaviour of the large PAH cations $C_{60}H_{22}{}^{+}$, showing that the PAH fragments isomerize (among other species) to C_{60}. However, they could not determine the relevant fragmentation energies and if photons with these energies are available in the ISM. Also, Micelotta et al. (2012) argue, on theoretical grounds, that the direct formation of C_{60} through the dissociation-induced curvature of dehydrogenated PAHs requires a very specific fine tuning of the dissociation parameters, and thus appears unlikely to happen in space (this is indeed a debated issue; Berné et al. 2015). It is not possible to adjust the number of carbons removed from the graphene flake in order to get the right size required for cage closure. To form fullerenes during the lifetime of the

reflection nebula NGC 7023, this mechanism needs a particular tuning of the parameters involved and PAHs with 70 carbon atoms require longer than this time to fragment. Thus, this mechanism seems not to work in the circumstellar environments around evolved stars and these molecules cannot be the precursors of the C_{60} observed at the present epoch (see Micelotta et al. 2012 for more details).

Contrary to the large PAHs fullerene formation scenario, the presence of HAC-like materials in space has been firmly established; e.g., from the sp^3 CH_3 and CH_2 stretching features contributing to the 3.4 μm absorption detected in very different astronomical environments (e.g., Alata et al. 2014 and references therein) or the aliphatic discrete emission features (e.g., at 3.4, 3.5, 6.0, 6.9, and 7.3 μm) and broad emission plateaus (e.g., at 6-9 and 9-13 μm) (e.g., Kwok & Zhang 2011 and references therein). Thus, at present, the most likely explanation for the simultaneous presence of fullerenes and PAH-like species in H-containing circumstellar environments is that they may be formed by the decomposition (e.g., by the UV radiation from the central star) of a carbonaceous compound with a mixture of aromatic and aliphatic structures (HAC-like; García-Hernández et al. 2011a, 2010, 2012b, 2011b; Micelotta et al. 2012), which should be a major constituent in the circumstellar envelope of C-rich evolved stars. This fullerene formation scenario (the HAC's scenario) is suggested by the coexistence of a complex mix of aliphatic and aromatic species such as HACs, PAH clusters, fullerenes, and small dehydrogenated carbon clusters (possibly planar C_{24} or a small fragment of a graphene sheet) in PNe of the Magellanic Clouds and our own Galaxy (García-Hernández et al. 2012b, 2011b). The coexistence of these molecular species in PNe with fullerenes supports the laboratory experiments carried out by Scott et al. (1997), which showed that the decomposition of HACs is sequential; small dehydrogenated PAH molecules are released first, followed by fullerenes and large PAH clusters. This formation process is also supported by the unique spectral variations seen in the IR spectrum of the fullerene-containing RCB star V854 Cen, which indicate that HACs have evolved into complex species such as PAH- and fullerene-like molecules in a timescale of only 10 years (García-Hernández et al. 2011a).

What is the prevalent formation process of fullerenes in circumstellar/interstellar environments? The relative spatial distribution of fullerenes, PAHs, and the 9-13 μm feature carrier provides the ideal test for answering this question

and for understanding the chemistry of large organic molecules in circumstellar/interstellar environments. The *Spitzer* observations of fullerene-containing PNe only offer a marginal amount of spatial information at a resolution of 3.6" (spatial information is only possible for low-resolution, R∼100, spectroscopy) and it is not possible to know the exact relative spatial distribution of these species. However, seeing-limited Gran Telescopio de Canarias (GTC)/CanariCam observations can improve the spatial resolution in a factor of about 10 with respect to *Spitzer*.

In this chapter we present GTC/CanariCam mid-IR imaging of the extended fullerene-containing PN IC 418. An overview of the observations (and data reduction) and the dust continuum-subtraction applied to our images are presented in Section 4.2 and 4.3, respectively. In Section 4.4 we study the relative spatial distribution of the fullerene-, PAH-like, and 9-13 μm emission. Section 4.5 discusses these results, while the main conclusions of our work are given in Section 4.6.

4.2 Mid-IR GTC/CanariCam observations

IC 418 is an elliptical PN, with a major axis of 14 arcsec and a minor axis of 11 arcsec (Ramos-Larios et al. 2012), which is surrounded by a more extended low-level ionized halo, and, in turn, by a neutral envelope with an angular size of about 2 (Taylor et al. 1989; Taylor & Pottasch 1987). This PN displays fullerene- and PAH-like (e.g., at 11.3 μm) features, together with a strong and broad 9-13 μm feature (see Figure 4.1). Moreover, we selected IC 418 (with an estimated distance of 1.26 kpc; Morisset & Georgiev 2009) for the GTC/Canaricam observations because it is the brightest and most spatially extended source from the known list of Northern fullerene-containing PNe (e.g., García-Hernández et al. 2012b; Otsuka et al. 2014).

IC 418 was observed by GTC with CanariCam (see Telesco et al. 2003). CanariCam can make mid-infrared (7.5 - 25 μm) imaging using a set of narrow, medium and broad-band filters. Our seeing-limited (FWHM ∼0.66 and 1.20" for the N and Q bands, respectively)[1] mid-IR images were obtained by using

[1]The seeing, in the V band, during the observations was 0.9" and 1.7" for the N and Q images, respectively. This corresponds to a FWHM of 0.66" and 1.2" for the N and Q bands, respectively. Therefore the images are seeing limited.

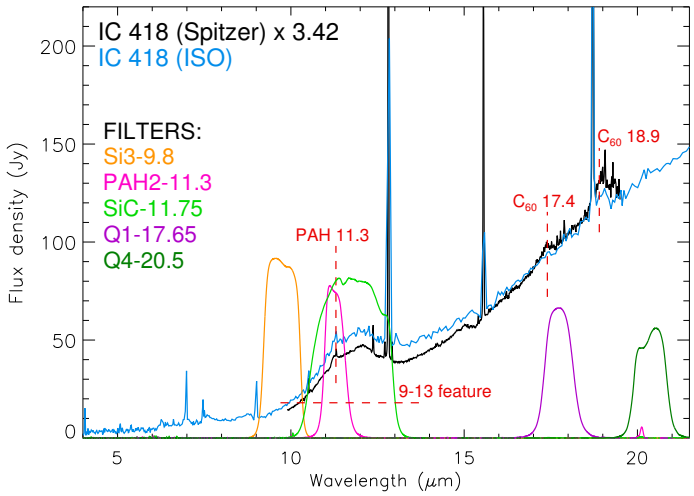

Figure 4.1: *ISO* (in blue) and *Spitzer* (in black) IR spectra of the PN IC 418 plotted together with the profiles of the five CanariCam filters used in the observations. The positions of the C_{60} bands at 17.4 and 18.9 μm, and the PAH-like feature at 11.3 μm (red dashed vertical lines) are marked. The broad 9-13 μm feature (red dashed horizontal line) is also marked.

narrow-band filters centered around the position of the features of our interest: PAHs, 9-13 μm, and C_{60} (see Figure 4.1) at 11.3 μm (PAH2, $\Delta\lambda$ = 0.6 μm), 11.75 μm (SiC, $\Delta\lambda$ = 2.5 μm), and 17.65 μm (Q1, $\Delta\lambda$ = 0.9 μm), as well as their adjacent continua at 9.8 μm (Si3, $\Delta\lambda$ = 1.0 μm), and 20.5 μm (Q4, $\Delta\lambda$ = 1.0 μm).

The observations were carried out in service mode in January and December 2013. The total available field of view for imaging is 26 arcsec x 19 arcsec, thus, in order to map the inner regions (<20"), we have done the off-chip chopping and nodding. Chopping and nodding techniques consist of introducing small offsets in multiple images to remove most of the background emission, the thermal emission from the telescope, and the detector 1/f noise, where f is the frequency of the noise component. Moreover, the off-chip mode means that the negative

images (from the off-source chop beam) are not seen in the detector image. The chop and nod position angles were 75° and −105°, respectively, with throws of 40 arcsec. We got one final summed image of IC 418 in the Si3, PAH2, and SiC filters, while we averaged 2 and 3 summed images in the Q1 and Q4 filters, respectively, in order to get a final image for each Q-band filter.

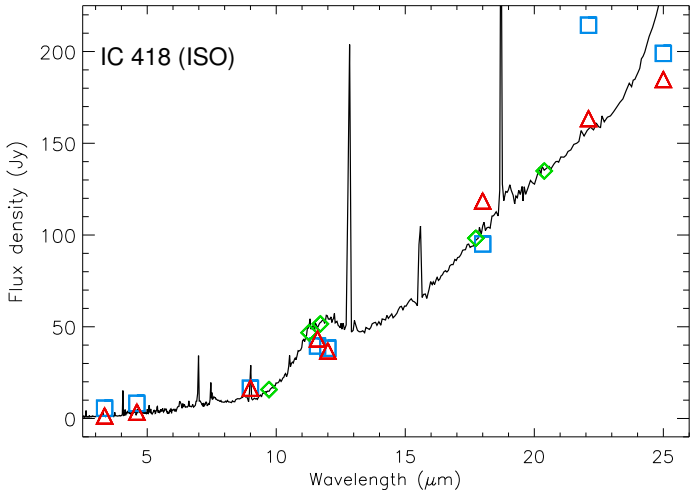

Figure 4.2: *ISO* spectrum of the PN IC 418 in comparison to observed (squares) and synthetic (triangles) *AKARI*, *WISE*, and *IRAS* photometry. The GTC/CanariCam (diamonds) synthetic photometry is also displayed for comparison.

Because we did not observe standard stars for flux calibration on the same nights as PN IC 418, we have followed two different procedures for flux calibration: i) using the observations of standard stars (HD 70272 and HD197989; available from the GTC data archive) that were observed at observational conditions as similar as possible to those of IC 418 but on different dates; and ii) using the *Infrared Space Observatory* (*ISO*) spectrum that covers the full nebula and assuming no significant IC 418 IR spectral variability in the last ∼30 years (see below). In the first case, the final images were processed us-

ing the pipeline RedCan (González-Martín et al. 2013), which produces final flux-calibrated (in Jy) images from the GTC/CanariCam raw data. Since the observations of the standard stars were made on different dates, in principle, the flux calibration may be quite uncertain; although we get ∼10−30% (depending on the filter) relative flux differences between GTC/Canaricam and *ISO*. In the second case, we first calculated the synthetic photometry (in Jy) through all Canaricam filters from the *ISO* spectrum using the SMART[2] software and we then calibrated our mid-IR images in order to get a total summed flux (in Jy) that coincides with the synthetic photometry. In Figure 4.2, we show the *ISO* spectrum of IC 418 in comparison to the observed WISE, AKARI, and IRAS photometry (Cutri et al. 2013; Helou & Walker 1988; Ishihara et al. 2010) as well as the corresponding synthetic photometry (again obtained from the *ISO* spectrum using SMART) in each one of the WISE (at ∼3.35, 4.6, 11.6, and 22.1 μm), AKARI (at ∼9 and 18 μm), and IRAS (at ∼12 and 25 μm) filters. There is no significant flux variation in the last ∼30 years; the only exception is the WISE W4 flux density at ∼22.1 μm, which seems to deviate from the *ISO* spectrum likely due to known saturation issues. The IRAS flux density at ∼25 μm also seems to deviate a little from the spectrum (for both observed and synthetic photometries). Table 4.1 gives the filter names, λ_c, bandwidth, total on-source exposure times, signal-to-noise ratio (S/N), observational dates, integrated fluxes, synthetic photometry, and the PN size in each mid-IR filter.

Figures 4.4 and 4.3 show the final flux-calibrated mid-IR GTC/CanariCam images of IC 418 using the synthetic photometry (case ii above). The PAH2 and SiC filters (with different widths) cover the PAH-like feature at 11.3 μm, the broad 9−13 μm feature, and dust continuum emission, while the Q1 filter covers the C_{60} emission band at 17.4 μm and dust continuum emission. The Si3 and Q4 filters cover the dust continuum emission at 9.8 and 20.5 μm, respectively (see Figure 4.1). In short, a similar ring-like extended structure is seen in all GTC/CanariCam filters, with the exception of the Si3 filter that shows that the dust continuum emission at 9.8 μm peaks closer the central star. Note that we excluded the contribution from the intense emission line of Ne II at 12.81 μm to the SiC filter. This line has only a contribution of ∼8.2% to the synthetic photometry in that filter. Moreover, the similar distribution of the PAH2 and

[2]The Spectroscopic Modeling Analysis and Reduction Tool (SMART), is a software package to reduce and analyze data from the Infrared Spectrograph (IRS) on the *Spitzer Space Telescope*.

Table 4.1: Summary of observational data.

Filter	λ_c (μm)	Bandwidth (μm)	Time (s) [a]	S/N [b]	Date	Flux (Jy) [c]	Synthetic photometry (Jy) [d]	Size [e]
Si3	9.8	1.0	661	13	2013 Jan 20	4.52	15.76	13.6" x 15.5"
PAH2	11.3	0.6	626	15	2013 Jan 20	36.76	46.78	14.3" x 17.4"
SiC	11.75	2.5	413	13	2013 Jan 2	42.39	51.56	13.8" x 16.0"
Q1	17.65	0.9	1274	10	2013 Dec 29	93.93	98.28	14.2" x 16.0"
Q4	20.5	1.0	1911	12	2013 Dec 29-30	112.69	134.91	14.6" x 17.1"

[a] Total on-source exposure time.
[b] S/N is an average of several measurements in each image.
[c] Integrated fluxes when calibrating with the standard stars HD70272 and HD197989 (see text for more details). The fluxes were measured defining the PN size in each mid-IR filter at the 3σ level (from the mean sky background) using the Graphical Astronomy and Image Analysis Tool (GAIA; http://star-www.dur.ac.uk/~pdraper/gaia/gaia.html). Flux errors are estimated to be in the range 10-30% (depending on the filter).
[d] Synthetic photometry through all CanariCam filters from the *ISO* spectrum using SMART (see text for details).
[e] Sizes measured at the 3σ level (from the mean sky background) in each mid-IR filter with standard tasks in IRAF.

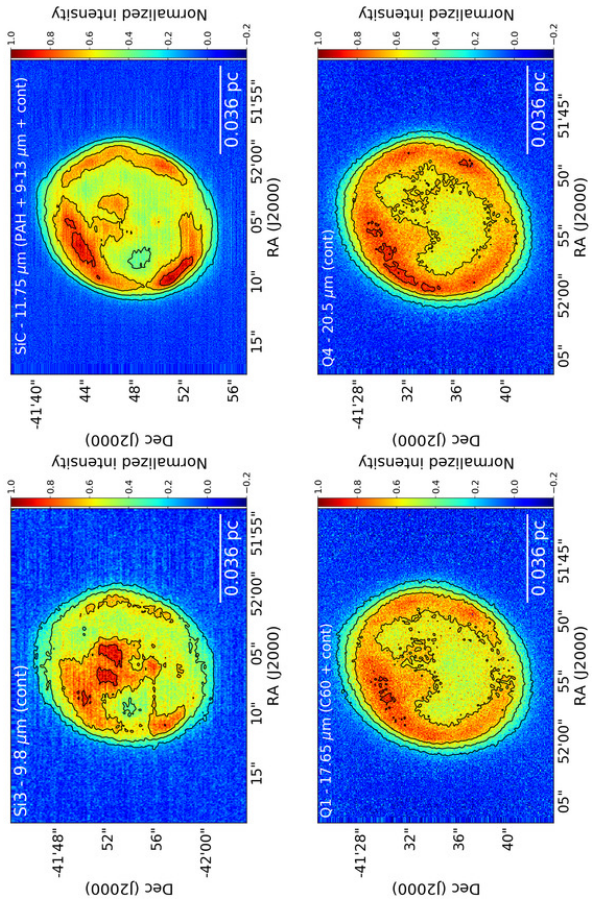

Figure 4.3: Contour maps of the flux-calibrated mid-IR GTC/CanariCam images of the C_{60}-PN IC 418 in the Si3, SiC, Q1, and Q4 filters. All contour maps have been normalized to the peak flux in the image. North is up, east is left. The bar in the lower right corner illustrates 0.036 pc at the distance to IC 418 (1.26 kpc; Morisset & Georgiev 2009). Contours range from 0.2 to 0.8 with 3 steps of 0.2 each.

SiC images suggests that we are not seeing this emission.

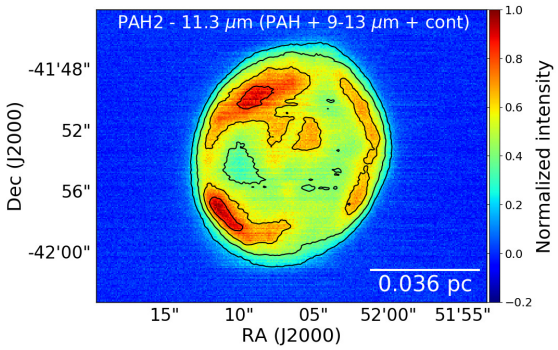

Figure 4.4: Contour map of the flux-calibrated mid-IR GTC/CanariCam image of the C_{60}-PN IC 418 in the PAH2 filter. The notation is the same as in Figure 4.4.

4.3 Dust continuum-subtraction

In order to study the relative spatial distribution of C_{60} fullerenes, PAH-like molecules, and the 9-13 μm feature carrier, we have to subtract the dust continuum contribution by using the Si3 (9.8 μm) and Q4 (20.5 μm) images.

The continuum subtraction from our images is complicated because the central star of PN IC 418 (nor any field star) is detected in our mid-IR images. Due to the flux units (Jy) of our flux-calibrated images, we have then only taken into account the slope of the *Spitzer* and *ISO* spectra of IC 418; i.e., the relative differences between the measured fluxes in the continuum at the central wavelength of all filters are used to scale the continuum images and subtract the dust continuum contribution[3]. In order to estimate the dust continuum

[3]The relative flux differences are very similar in the *Spitzer* and *ISO* spectra (see Figure 4.1).

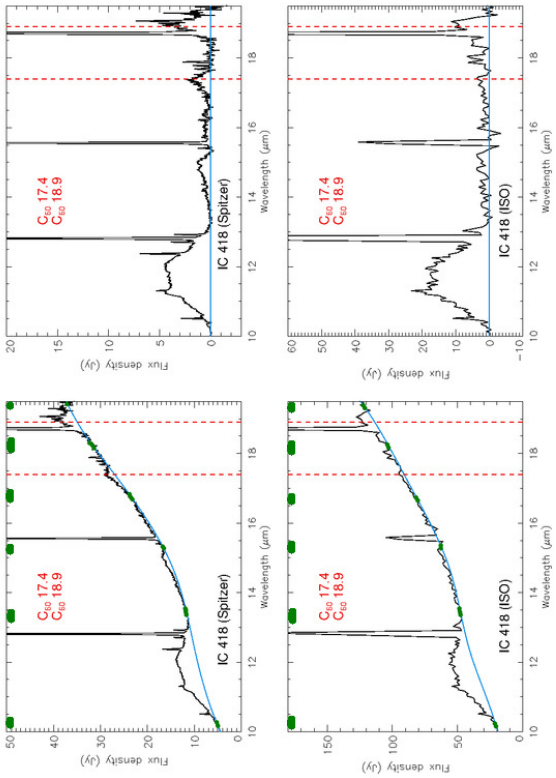

Figure 4.5: Polynomial fits made to the dust continuum of the *Spitzer*/IRS and *ISO* spectra (left panels) and the corresponding residual spectra (right panels) for the fullerene PN IC 418. Both left panels display the observed IR spectra (in black) together with a polynomial fit (in blue) to continuum points (in green) free from any gas and dust feature. The corresponding residual or dust continuum subtracted spectra (in black) are shown in right panels. The band positions of the C_{60} features at 17.4 and 18.9 μm (red dashed vertical lines) are indicated.

contribution for each filter, we have fitted a polynomial spline of order 4 to the continuum (free from any gas/dust feature) in the *Spitzer* and *ISO* spectra by using standard tasks in IRAF (see Figure 4.5).

By assuming that the continuum flux ratios (or relative differences) between the wavelengths of our interest are similar in both *Spitzer/ISO* spectra and GTC/CanariCam images (see above about the non IR variability of IC 418 during the last ∼30 years; Figure 4.2), we find that we have to scale the Q4 image by a factor of ∼0.70 for the case of the Q1−Q4 continuum-subtraction, while the Si3 images have to be scaled by factors of ∼1.90 and 2.17 for the PAH2−Si3 and SiC−Si3 continuum-subtractions, respectively. Moreover, in order to extract the PAH-like 11.3 μm emission from the PAH2 image (PAH2−SiC), we have to scale the SiC image (assumed to be dominated by the broad 9-13 μm emission; see Figure 4.1) by a factor of ∼0.87. The final continuum-subtracted images have been boxcar smoothed with a 2x2 window to increase the S/N. Figures 4.6 and 4.7 show the resulting PAH2−Si3, SiC−Si3, and Q1−Q4 continuum-subtracted images as well as the PAH2−SiC subtracted image, which were flux-calibrated using the synthetic photometry (case ii) and the standard stars (case i), respectively.

The continuum-subtracted images obtained with the case i flux calibration (using the standard stars; Figure 4.7) seem to be worst than those obtained with the case ii one (using the synthetic photometry; Figure 4.6). This is due to the use of standard stars observed on different dates (at slightly different weather conditions), which produces non-systematic flux uncertainties that ramdonly vary among the GTC/CanariCam filters; the relative flux differences between GTC/CanariCam and *ISO* vary between ∼10 and 30% (depending on the filter; see Table 4.1). This is clearly evidenced by the resulting PAH2−Si3 and SiC−Si3 images (case i; Figure 4.7) that show a strong excess emission closer to the central star. This excess of emission in the inner regions of the nebula is an artifact due to a bad removal of the dust continuum emission at 9.8 μm (Si3 filter; see Figure 4.4). The resulting PAH2−Si3 and SiC−Si3 images obtained with the case ii flux calibration (Figure 4.6) do not display such excess emission, indicating that the Si3 dust continuum contribution is subtracted correctly. Taking into account this and the non-IR variability of IC 418 (Figure 4.2), in the following we thus make use of the continuum-subtracted images obtained using the synthetic photometry (case ii flux calibration).

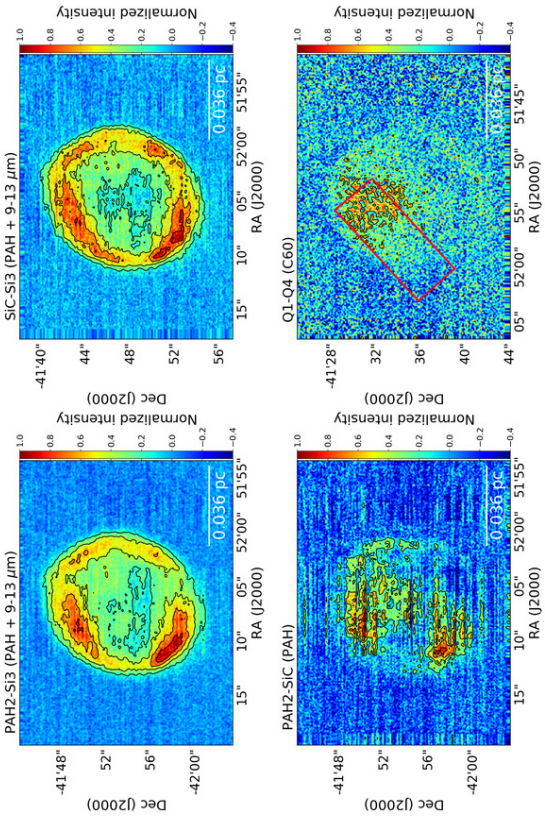

Figure 4.6: Contour maps of the mid-IR GTC/CanariCam PAH2−Si3, SiC−Si3, PAH2−SiC, and Q1−Q4 images of IC 418. The flux calibration was performed using the synthetic photometry (case ii in the text) and all contour maps have been normalized to the peak flux in the image. In the PAH2−Si3, SiC−Si3, and PAH2−SiC images, contours range from 0.2 to 0.8 with 3 steps of 0.2 each. In the Q1−Q4 image only one contour at 0.4 is displayed. Note that the position and the size of *Spitzer*/IRS SH slit is indicated by the black box (dimension: 4.7" x 11.3") superimposed to the Q1−Q4 image.

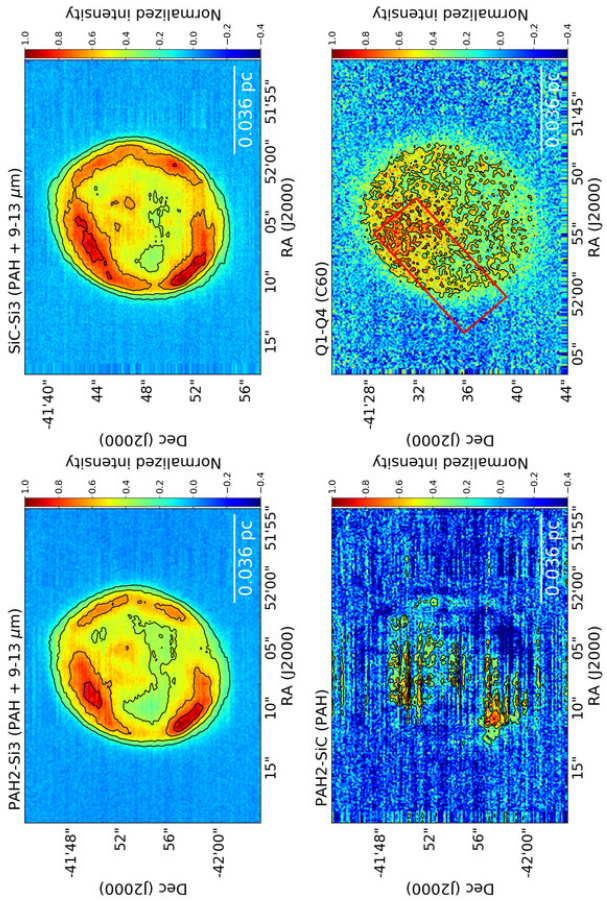

Figure 4.7: Contour maps of the mid-IR GTC/CanariCam PAH2−Si3, SiC−Si3, PAH2−SiC, and Q1−Q4 images of IC 418 when calibrating with the standard stars (case i in the text). The notation is the same as in Figure 4.6 but the contours are slightly different. In particular, only two contours at 0.4 and 0.6 are displayed in the Q1−Q4 image.

4.4 Results

4.4.1 Fullerene emission

The Q1 and Q4 images (see Figure 4.4) show a similar ring-like structure, which indicates that fullerenes may be co-spatial with the dust continuum emission (e.g., they could be attached to the dust grains) or that both images are dominated by the dust continuum emission. IC 418 displays a very low C_{60}-to-continuum ratio (e.g., $F_{17.4}/F_{cont} \sim 0.06$, see below) and the similar spatial distribution seen in the Q1 and Q4 images already suggests that both images are likely dominated by the strong dust continuum emission. The continuum-subtracted fullerene-like emission (the Q1−Q4 image in Figure 4.6) is very weak (at $\sim 4\sigma$ from the mean background level) and mainly located at the northeast, extending from the inner (even near the central star) to the outer regions of the nebula. Due to the low C_{60}-to-continuum ratio we cannot discard additional weaker fullerene emission from rest of the ring-like structure seen in the Q1 image. Indeed, changing by ∼5-20% the factor used to subtract the Q4 continuum contribution, one can recover the ring-like structure in the resulting Q1−Q4 image (with a value of 0.56). Figure 4.8 shows a sequence of Q1−Q4 images that are obtained by applying different factors to the subtraction. This can be applied to both calibrations.

We note that the *Spitzer*/IRS SH slit only covers part of the nebula, while the ISO SWS diaphragm covers the entire nebula (see Pottasch et al. 2004 and Otsuka et al. 2014 for more details). In Figure 4.6, we display the Q1−Q4 continuum-subtracted image of IC 418 overlaid with the *Spitzer*/IRS SH slit. Interestingly, the *Spitzer* slit just covers the northeast region of the nebula, where the residual fullerene emission seems to be located. This could explain why *Spitzer* clearly detected the fullerene IR features in IC 418 and it would suggest that the residual fullerene emission observed could be real. We have measured the integrated fluxes of the C_{60} bands at 17.4 and 18.9 μm[4] (with SMART) in the *Spitzer* and *ISO* spectra (see Figure 4.5). In Table 4.2, we list the central wavelengths and integrated fluxes for these two C_{60} fullerene bands in both *Spitzer* and *ISO* spectra. The integrated fluxes of both C_{60} bands

[4]We have not considered the weak emissions in the red wing of the fullerene band due to a P III line at 17.88 μm (and other species). In any case, the contribution of these weak emissions is very small (Bernard-Salas et al. 2012).

in the *ISO* spectrum are higher than those of the *Spitzer* one, as expected because of the larger *ISO* aperture and the fact that weaker fullerene emission could be distributed along the nebula (Figures 4.6 and 4.7). We measure C_{60} F(17.4)/F(18.9) flux ratios of 0.50±0.12 and 0.39±0.24 in the *Spitzer* and *ISO* spectra, respectively[5]; both ratios are similar within the errors. The feature-to-continuum ratios of the C_{60} 17.4 and 18.9 μm bands, however, are slightly higher in the *Spitzer* spectrum (0.063±0.004 and 0.113±0.007, respectively) than in the *ISO* (0.037±0.008 and 0.089±0.009, respectively) spectrum, which again might indicate that the excess of fullerene 17.4 μm emission is real, but more important it suggests that the strength of the fullerene emission could have slightly increased from the *ISO* (1998) to the *Spitzer* (2004) observations in a timescale of only 6 years[6]. Indeed, the integrated fluxes measured in the Q1−Q4 and SiC−Si3 images, along the *Spitzer* SH slit, are $\sim 2.09\times10^{-18}$ and 3.07×10^{-17} W cm^{-2}, which are ∼3.5 and 1.2 times higher than the C_{60} 17.4 μm and 9−13[7] μm integrated fluxes measured in the *Spitzer* spectrum (Table 4.2).

Table 4.2: Mid-IR C_{60} features in the PN IC 418.

Spitzer spectrum		*ISO* spectrum	
λ (μm)	Flux (W cm^{-2})	λ (μm)	Flux (W cm^{-2})
17.35	6.05e-19(±0.72)	17.32	1.31e-18(±0.52)
18.97	1.20e-18(±0.15)	18.97	3.35e-18(±0.75)

Estimated flux errors (between brackets) are always less than ∼30%-40% (estimated by SMART).

[5]We note that Otsuka et al. (2014) measured a C_{60} F(17.4)/F(18.9) flux ratio of 0.46±0.03 in the IC 418 *Spitzer* spectrum, which agrees well, within the errors, with the one derived here.

[6]García-Hernández et al. (2011a) found even more extreme IR spectral changes in the fullerene-containing RCB star DY Cen, where the IR spectrum dramatically changed in a timescale of about ten years, evolving from from HAC-like (*ISO*) to PAH- and C_{60}-like features (*Spitzer*).

[7]The integrated flux of the 9−13 μm feature in the *Spitzer* spectrum is $\sim 2.56\times10^{-17}$ W cm^{-2}.

The synthetic photometry through the GTC/Canaricam filters PAH2, SiC, and Q1 from the *Spitzer* spectrum gives values of 11.42, 13.17, and 29.55 Jy, respectively, while by summing the flux in our GTC/Canaricam images, in these three filters along the *Spitzer* aperture (see Figure 4.6), we get integrated fluxes of 15.90, 17.56, and 31.61 Jy, respectively. The fluxes measured in our GTC/Canaricam images in the filters covering the C_{60} 17.4 μm (Q1) and the broad 9-13 μm (SiC) emissions are thus about 7% and 25% higher than those from the *Spitzer* spectrum; 28% higher for the narrower PAH2 filter.

Even thinking that the flux calibration errors in our GTC/Canaricam data are difficult to estimate, this also suggests a 17.4 μm excess emission in our GTC/Canaricam observations compared with the *ISO* ones, which is in line with the apparent 17.4 μm excess emission in the *Spitzer* spectrum. The observed spatial distribution of C_{60}, if real, may have several interpretations and higher sensitivity mid-IR observations would be desirable (see Section 4.5).

4.4.2 11.3 μm PAH-like + 9-13 μm carrier emission

The Si3 image displays the strongest emission near the IC 418 central star and weaker emission (mainly at the northeast and southeast of the nebula) from the outer ring-like structure. The PAH2 and SiC images, however, show the strongest emission from the outer ring-like structure with the weaker emission near the central star, where the Si3 emission is maximum (see Figures 4.4 and 4.3). The 11.3 μm PAH-like + 9-13 μm carrier emission is obtained by doing the PAH2−Si3 and SiC−Si3 subtractions (see Figure 4.6). The PAH2−Si3 and SiC−Si3 continuum-subtracted images display an identical spatial distribution. The similar morphology together with the very weak PAH-like 11.3 μm feature (see Figure 4.1) suggest that the emission is dominated by the 9−13 μm carrier in both filters. The latter is confirmed by the PAH2-SiC subtraction (see below). The 9−13 μm carrier emission is distributed around the outer ring-like structure, with the strongest emission (at more than 13σ from the mean background level in Figure 4.6) at the northeast (and southeast) sides of the nebula.

The spatial distribution of the 9-13 μm carrier emission is very similar to the dust continuum emission at 20.5 μm (Q4), which suggests that the 9−13 μm carrier is co-spatial with the dust grains emitting at 20.5 μm. On the other hand, by comparing the Si3 image with the IC 418 Hubble Space Telescope

images in several optical nebular emission lines (see Figure 4.10), we find that the dust continuum emission at 9.8 μm is very similar to the [O III] nebular emission, indicating that dust grains may coexist with ionized material.

Interestingly, we could separate the PAH-like emission at 11.3 μm from the PAH2 image by doing the PAH2−SiC subtraction (see Figure 4.6). The PAH2−SiC image displays a less extended residual emission with intensity peaks (at $\sim 5\sigma$ from the mean background level in Figure 4.6) at the northeast and southeast sides of the nebula. This suggests that the ring-like structure seen in the PAH2−Si3 and SiC−Si3 continuum-subtracted images is mostly due to the 9−13 μm carrier emission and that the aromatic-like component coexist with the 9−13 μm carrier.

4.4.3 Intensity profiles

Normalized intensity profiles through the individual images (Si3, PAH2, SiC, Q1, and Q4 filters) and subtracted images (PAH2−Si3, SiC−Si3, PAH2−SiC, and Q1−Q4) at position angles (P.A.) of 70° and 110° from east in a clockwise direction are shown in Figure 4.9. These P.A. were selected to trace the residual fullerene emission (P.A.=70°) as well as the ring-like structure along the major nebular axis (P.A.=110°). The profiles are made by doing a cross-cut through the x-axis and a block average of 50 lines through the y-axis. We have chosen a number of lines that corresponds to 4 arcsec.

The intensity profiles along the Q1 and Q4 images have the same shape (independently of the P.A.) because the continuum contribution is likely dominating the emission in both filters, while the intensity profile along the Q1−Q4 show the location and extension of the residual fullerene emission (upper panels in Figure 4.9). The same behaviour is seen for the PAH2 and SiC filters and their intensity profiles are very similar (they mainly trace the outer ring-like structure) because both filters just cover the same features but with different filter width. However, both PAH2 and SiC intensity profiles are different to the Si3 intensity profile (covering the continuum at 9.8 μm), which shows the maximum intensities at $\sim$1.2" from the central star ($\sim$1512 AU at 1.26 kpc; Morisset & Georgiev 2009; see Figure 4.9). It is notable that the outer ring-like structure is clearly seen in the SiC−Si3 and PAH2−Si3 profiles, where the continuum contribution has been greatly subtracted from the SiC and PAH2

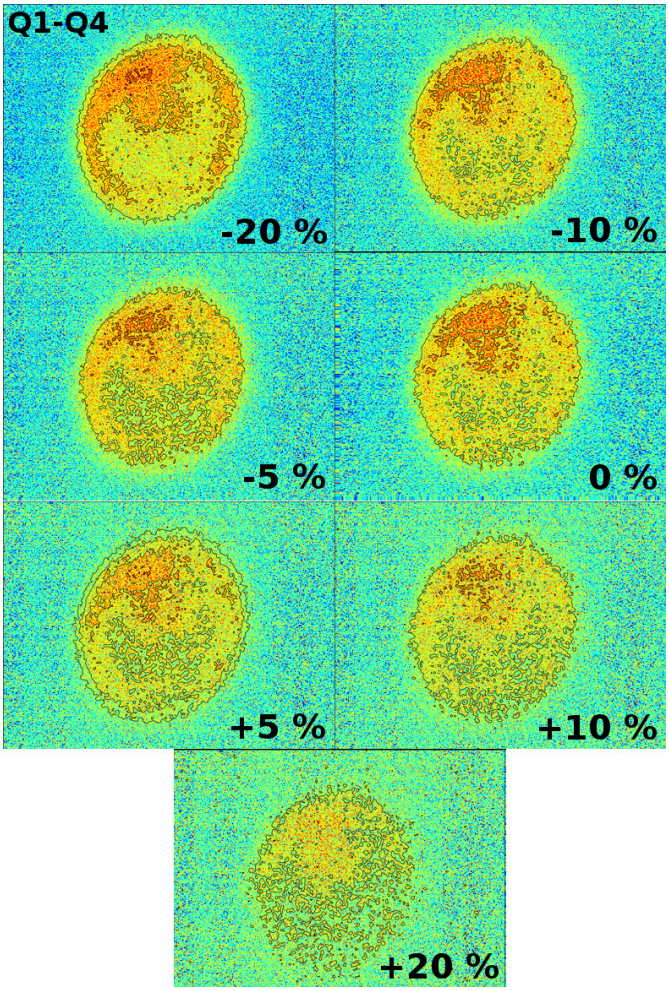

Figure 4.8: Sequence of images showing the changes of the Q1−Q4 subtraction (calibrated using the standard stars) by using different factors (within ±20% of the original value). With a value of 0.56 (-20%), we recover the ring-like structure seen in the original images.

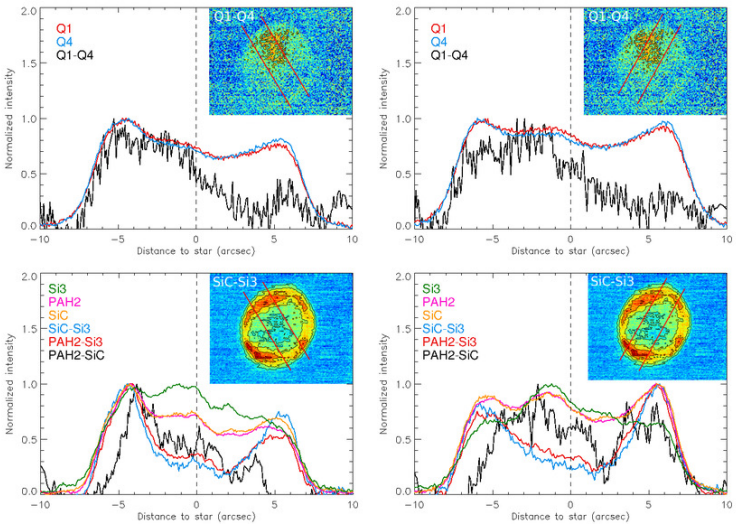

Figure 4.9: Normalized intensity profiles along the IC 418 nebula at P.A. of 70° (left panels) and 110° (right panels) from east as a function of the distance to the central star. The P.A. and the 4 arcsec width are indicated in the inset panels. The top panels show the intensity profiles in the Q1 (C_{60} + continuum at 17.65 μm; in red), Q4 (continuum at 20.5 μm; in blue), and continuum-subtracted Q1−Q4 (C_{60}; in black) images. The lower panels show the intensity profiles in the Si3 (continuum at 9.8 μm; in strong green), SiC and PAH2 (both containing 9-13 μm carrier + 11.3 μm PAH-like emission + continuum; in brown and pink, respectively), PAH2−SiC (11.3 μm PAH-like emission; in black), and continuum-subtracted SiC−Si3 and PAH2−Si3 (9-13 μm carrier + 11.3 μm PAH-like emission; in blue and red, respectively) images, which were calibrated using the synthetic photometry. The vertical dashed line mark the nebula center (or central star position).

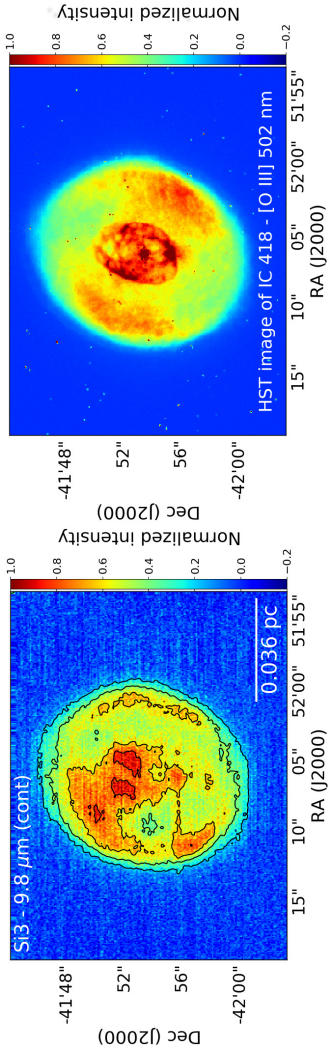

Figure 4.10: Images of the C_{60}-PN IC 418 in the mid-IR GTC/CanariCam Si3 filter at 9.8 μm (left panel) and the optical HST F502N filter at 502 nm (right panel). Both maps have been normalized to the peak flux in the image. Note the similarity between the maxima of continuum emission at 9.8 μm and [O III] nebular emission at 502 nm.

profiles. Finally, the PAH2−SiC profiles show the residual excess emission towards the northeast of the nebula (P.A.=70°) as well as the even weaker (and more homogenous) emission along the major nebular axis (P.A.=110°).

The residual fullerene emission (see Figure 4.9) mainly extends (almost uniformly) from the central star to ∼7" at the northeast side of the nebula (∼8820 AU), peaking at ∼4.5-5.5" (∼5670-6930 AU); a secondary much weaker (and tentative) peak is also present at the opposite side of the nebula at ∼5.5-6" (∼6930-7560 AU). The 9-13 μm carrier (+ weak 11.3 μm PAH-like) emission is distributed along the ring-like structure with emission peaks at similar distances from the central star position (at ∼4.5" and ∼5.5" at the northeast and southwest sides of the nebula) with extremely weak emission in the inner regions. The weak 11.3 μm PAH-like emission, on the contrary, seems to be located in a more internal region than the 9-13 μm carrier, peaking at ∼4" (∼5040 AU) at the northeast side of the nebula (see the bottom-left panel in Figure 4.9); another peak emission of similar strenght (which is not traced by the intensitiy profiles at P.A.=110° displayed in the bottom-right panel in Figure 4.9) is seen at a similar distance towards the southeast.

4.5 Discussion

The present mid-IR images provide further information about the spatial distribution of the fullerene- and PAH-like features as well as the 9-13 μm feature carrier in a fullerene-rich PN such as IC 418.

Fullerene emission at 17.4 μm extends from the central star to ∼8820 AU at the northeast side of the nebula (the maximum intensity is around 6300 AU). This is comparable to the case of the other known fullerene-rich extended PN Tc 1, where lower spatial resolution *Spitzer* observations suggest that the 8.5 μm fullerene emission peaks at 6400-9700 AU from the central star (Bernard-Salas et al. 2012)[8]. Furthermore, Bernard-Salas et al. (2012) found that fullerene emission at 8.5 μm and PAH-like emission at 11.2 μm seem to be displaced from the central star and peak at opposite directions, while the IR emission at 9 μm (dust continuum) and 12 μm (the 9-13 μm carrier) are less extended

[8] A complete ring-like structure of the C_{60} 8.5μm emission, at a similar distance of ∼8000 AU, seems to be confirmed by preliminary (non-continuum subtracted) higher spatial resolution images of Tc 1 from Gemini-S/Trecs (Golriz et al., in prep.).

and centered on the Tc 1's central star. In the case of PN IC 418, however, it seems that fullerene-like 17.4 μm and PAH-like 11.3 μm are not necessarily co-spatial but both emissions have peaks towards the northeast of the nebula; although at sligthly different distances from the central star (at $\sim$6300 and $\sim$5040 AU, respectively). However, the emission may originate in an ellipsoid around the central star and we see such distribution due to projection effects (see e.g., Manchado 2004). In IC 418, the dust continuum emission at 9.8 μm is also extended and peaking near the central star (at $\sim$1512 AU), but the 9-13 μm carrier is mainly distributed in the outer ring-like structure. Thus, it is not actually clear if the 12 μm emission in Tc 1 might be dominated by the dust continuum or by the 9-13 μm carrier. In our mid-IR images of IC 418, it seems clear that the 9-13 μm carrier emission dominates over the adjacent dust continuum emission.

As we have mentioned in the introduction of this chapter, there are actually two different top-down fullerene formation models, starting from the photochemical processing of large PAHs (Berné & Tielens 2012) or HAC-like grains (García-Hernández et al. 2010), to explain the formation of fullerenes in space. The C_{60}-rich astronomical environments can be characterized by strong aromatic-like emission features (e.g., in the ISM around reflection nebulae such as NGC 7023,) or by broad $\sim$6$-$9, 9$-$13, and 25$-$35 μm aliphatic-like emission features (e.g., in the circumstellar environment around PNe like IC 418 and Tc 1). Thus, the large PAHs model assumes that the set of aromatic-like features is due to PAH molecules, while the carrier of the aliphatic-like features (or at least for some of them) is supposed to be somekind of mixed aromatic/aliphatic HAC-like material in the HAC model. Both sets of IR features (aromatic- and aliphatic-like), however, still wait for a definitive identification of their carriers (see Chapter 3 for more details); so it is more appropiate to talk about undidentified IR emission features (UIR).

There are several pieces of evidence that favour the large PAHs route in the ISM (e.g., Berné & Tielens 2012; Castellanos et al. 2014; Zhen et al. 2014) and the HAC-like one in the circumstellar medium (e.g., García-Hernández et al. 2011a, 2010, 2012b, 2011b; Micelotta et al. 2012; Scott et al. 1997). In particular, the fact that C_{60} emission is found near the illuminating star of the reflection nebula NGC 7023, where the PAH-like emission is weakest[9] has been

[9]The PAH-like emission in NGC 7023 peaks farther away from the illuminating star than the C_{60} emission.

used to argue that fullerenes are likely a photochemical product of PAHs (Berné & Tielens 2012; Castellanos et al. 2014).

The interpretation of our IC 418 GTC/Canaricam mid-IR images regarding the dominant fullerene formation process in PNe is somewhat contradictory. The presence of fullerene emission near the central star, where the 9-13 μm emission is much weaker, would suggest that C_{60} may be a photo-product of the 9-13 μm carrier. However, fullerenes seem to coexist with the 9-13 μm carrier at the northeast outer regions of the nebula; something that could indicate that fullerenes may be attached to dust grains or well mixed with the 9-13 μm carrier. An alternative interpretation may be that fullerenes are not directly linked to the 9-13 μm carrier. Finally, another exciting interpretation (perhaps more consistent with the fullerene-like emission observed) is that other fullerene-based species are contributing to the observed 17.4 μm emission; with ionized and/or more resistant fullerene-based species located in the inner regions near the central star and neutral (and/or more resistant) fullerenes distributed in the outer ring-like structure. More complex fullerene-based species can emit at this wavelength. For example, laboratory IR spectra of fullerene-based species like fullerene-PAHs adducts display spectral features strikingly similar to those from C_{60} (and C_{70}) fullerenes (e.g., Cataldo et al. 2014, 2015; García-Hernández et al. 2013; Garcia-Hernandez et al. 2016). Furthermore, a recent theoretical study of the vibrational modes of hydrogenated fullerenes (fulleranes; $C_{60}H_m$, m=2-36) shows that the four mid-IR bands (at ∼7.0, 8.5, 17.4, and 18.9 μm) of the C_{60}-skeletal vibrations are stronger in fullerenes at low hydrogenation (m=2-8) and the astronomically observed IR bands assigned to C_{60} could be due to fullerenes/fulleranes mixtures (Zhang et al. 2017). Note that we saw in Chapter 3 that the intensity of fullerane bands in the 3-4 μm region is higher for highly hydrogenated fullerenes (Sadjadi 2017). Interestingly, most of $C_{60}H_m$ display stronger emission features at 17.4 μm (i.e., higher 17.4 μm/18.9 μm band ratios) than C_{60} and fulleranes could potentially explain the intriguing spatial distribution of the residual 17.4 μm emission seen in IC 418.

We note that our mid-IR images do not provide definitive proof about the dominant excitation mechanism of the fullerene-like emission (e.g., thermal or fluorescence emission); as it is also found in the literature (e.g., Bernard-Salas et al. 2012; Brieva et al. 2016; García-Hernández et al. 2012b; Otsuka et al. 2014). Our observations may suggest that fullerenes could be attached to dust

grains due to the considerable similarity between the spatial distribution of the IR emission in the Q1 and Q4 filters. In thermal excitation, fullerenes should closely follow the dust distribution and show a similar behaviour with respect to the distance to the central star. If dust grains are in radiative equilibrium with the radiation field in IC 418 (d=1.26 kpc), we obtain that the temperature of the dust grains at 6300 AU from the central star (adopting log $(L_*/L_\odot)$ = 3.88 for IC 418; e.g., Otsuka et al. 2014) would be of only 33 K (Equation (3) in García-Hernández et al. 2012a). However, the temperature of thermally excited fullerene molecules in PNe range from ∼200 to 600 K (e.g., García-Hernández et al. 2012b). Thus, the spatial distribution of fullerenes in IC 418 (as well as in Tc 1) could favor fluorescence excitation; in this case the fullerene emission should show little dependence with respect to the distance to the central star, as it seems to be observed. However, fluorescence models cannot fully reproduce the emission of the fullerene IR bands in PNe and contamination of the C_{60} band strengths from UIR or other species like fullerene-clusters has been suggested (e.g., Bernard-Salas et al. 2012, 2013; Brieva et al. 2016). Very recently, Zhang et al. (2017) show that the inconsistency between the thermal/fluorescence models and the C_{60} IR band ratios observed in PNe can be solved by hydrogenation effects (see above) and that hydrogenated fullerenes might be present in these objects, contributing to the observed IR emission. This would be consistent with the idea of other fullerene-based species like fulleranes with low H-content emitting at 17.4 μm, as tentatively suggested by the IC 418 mid-IR observations presented here.

In short, our GTC/Canaricam observations of IC 418 thus show that higher sensitivity mid-IR images as well as spatially resolved mid-IR spectra along the nebula (e.g., using the upcoming James Webb Space Telescope, JWST) are needed in order to confirm the spatial distribution of the fullerene-, aromatic-, and aliphatic-like species and to learn about fullerene formation and excitation in the complex circumstellar environments around PNe.

4.6 Conclusions

- We have presented for the first time high spatial resolution mid-IR images of a C_{60}-containing PN, IC 418. Seeing-limited narrow-band mid-IR observations were carried out with Canaricam at the GTC 10.4m using a set of N- and Q-band filters covering the fullerene-like band at 17.4 μm, the

PAH-like feature at 11.3 μm, and the broad 9-13 μm aliphatic-like feature as well as their adjacent continua. The main aim is to get some observational constraints on the formation process of fullerenes in the H-rich circumstellar environments around PNe by studying the relative spatial distribution of these complex species; all of them seen in the IC 418 *Spitzer* and *ISO* spectra.

- A ring-like extended structure (at a distance of about 7" or ∼6300 AU at the IC 418's distance of 1.26 kpc) is seen at all IR wavelengths. The only exception is the dust continuum emission at 9.8 μm, which peaks much closer the central star. The spatial distribution of the IR emission in the Q1 (C_{60}; 17.4 μm) and Q4 filters (dust continuum; 20.5 μm) is very similar, suggesting that both wavelengths are probably dominated by the dust continuum emission (in agreement with the very low IC 418 C_{60}-to-continuum ratio).

- In spite of the difficulties found to subtract the dust continuum contribution from our images, the non-signicant IC 418 IR spectral variability in the last ∼30 years has permitted us to perform the dust continuum subtraction making use of synthetic photometry (i.e., through all Canaricam filters from the *ISO* spectrum). The resulting continuum-subtracted mid-IR images show a clear ring-like extended emission structure for the broad 9-13 μm carrier, which indicates that the dust grains emitting at 20.5 μm are co-spatial with the carrier of the 9-13 μm emission feature. Only weak residual emission (at $\sim 4-5\sigma$ from the mean background level) is recovered for the PAH- and fullerene-like emission at 11.3 and 17.4 μm, respectively. The 11.3 μm PAH-like emission seems to partially follow the ring-like structure seen at other wavelengths, while the 17.4 μm C_{60}-like emission is mainly located at the northeast, extending from the central star to the outer regions of the nebula (i.e., the ring-like structure clearly seen at 20.5 μm). Moreover, we may be seeing a part of the emission of an ellipsoid due to projection effects.

- Our IC 418 GTC/Canaricam mid-IR images might have several interpretations regarding the dominant fullerene formation process in PNe. Perhaps, the more exciting - but consistent with the observed spatial distribution of the C_{60}-like emission - interpretation is that other more complex fullerene compounds are contributing to the observed 17.4 μm emission. In this

context, hydrogenated fullerenes with very low H-content seem to be potential candidates for the possible contaminants, which otherwise could explain the present inconsistency between the fullerene-like IR band ratios observed in PNe and the prediction of thermal/fluorescence excitation models.

- In summary, we conclude that higher sensitivity mid-IR images and spatially resolved spectroscopic observations (e.g., by using the upcoming JWST) are necessary to confirm the spatial distribution of the fullerene-, aromatic-, and aliphatic-like species in fullerene-rich PNe. This is especially important around the long-wavelength C_{60}-like emission features (the Q-band) where the water vapour severely limits the IR observations from ground-based telescopes. The JWST is thus the ideal astronomical facility to understand the formation and excitation of fullerenes in circumstellar environments.

5

Conclusions

We summarize here the main findings of the thesis.

5.1 Diffuse bands in fullerene planetary nebulae

We have searched diffuse interstellar bands (DIBs) in the optical spectra of three planetary nebulae (PNe) with fullerenes. We have identified 20, 12, and 11 absorption bands towards Tc 1, M 1-20, and IC 418, respectively, that are previously reported DIBs in the literature.

The PN Tc 1, with the highest S/N spectrum and a proper comparison star, shows six of the strongest and well-studied DIBs (i.e., those at 5797, 5850, 6196, 6270, 6379, and 6614 Å), and nine other weaker interstellar features (i.e., those at 5776, 6250, 6376, 6597, 6661, 6792, 7828, 7833, and 8038 Å) that are normal for its reddening. However, the five DIBs at 4428, 5780, 6203, 6284, and 8621 Å are found to be unusually strong towards Tc 1. The radial velocities of four of these DIBs (i.e., those at 5780, 6203, 6284, and 8621 Å) confirm their interstellar origin. The carriers of the "normal" DIBs may not be particularly overabundant towards fullerene PNe, but the high ionization degree towards Tc 1 suggests that the carriers of the unusually strong DIBs may be ionized species. The 4428 Å feature, on the contrary, seems to be centred at the Tc 1's radial velocity, suggesting a circumstellar origin.

For the two PNe M 1-20 and IC 418, the situation is worse than in Tc

1, since their spectra are of lower quality and their comparison stars seem to map slightly different ISM conditions. Anyway, we used the same classification scheme ("normal" versus "unusually strong" DIBs). The 4428 Å feature is found to be unusually strong in these objects, a characteristic that seems to be common to fullerene PNe.

Due to the high radial velocity of Tc 1, we were able to search for diffuse circumstellar bands (DCBs) in its optical spectrum. Interestingly, we report the first tentative detection of two DCBs at 4428 and 5780 Å in the fullerene-rich circumstellar environment around Tc 1. The presence of 4428 and 5780 Å nebular emission at the radial velocity of Tc 1 further suggests their circumstellar origin. Moreover, we have estimated the abundances of the carriers of the DCBs at 4428 and 5780 Å, and we conclude that at present large fullerenes and buckyonions cannot be completely discarded as possible carriers of the 4428 and 5780 Å features. The low S/N in the optical spectra of M 1-20 and IC 418 has not permitted us to detect DCBs.

Similarly to Tc 1, we could not find evidence of the strongest electronic transitions of neutral C_{60} in the IC 418 optical spectrum. The non-detection of neutral C_{60} optical absorptions in fullerene PNe could be explained if the C_{60} IR emission peaks far away from the central star.

5.2 Non-detection of hydrogenated fullerenes (fulleranes) in fullerene planetary nebulae

We have presented VLT/ISAAC 2.9-4.1 μm spectroscopy of the two fullerene PNe Tc 1 and M 1-20. The spectrum of Tc 1 shows a continuum with no signs of UIR features and only H (and He) nebular lines. This indicates that the IR bands seen in the Tc 1 *Spitzer* spectrum are very likely due to C_{60} and C_{70} alone, and not other kinds of molecules, such as fulleranes with high H-content or fullerene/PAH adducts. The M 1-20 VLT/ISAAC spectrum shows H and He nebular lines in conjunction with the UIR feature at 3.3 μm.

The VLT/ISAAC and *Spitzer* spectra of these fullerene PNe confirm a correlation between the 3.3 and 11.3 μm UIE features, as previously reported in the literature, which suggests a common carrier for the two features. Unfortunately,

the VLT/ISAAC observations, presented here, cannot reveal the nature of the real carrier.

Interestingly, we have reported the non-detection of the strongest bands of hydrogenated fullerenes (fulleranes with high H-content such as $C_{60}H_{18}$, $C_{60}H_{36}$, $C_{70}H_{38}$, and a fullerane mixture) at ∼3.44, 3.51 and 3.54 μm in the 3−4 μm spectra of the fullerene-containing PNe Tc 1 and M 1-20. From a comparison of the predicted fluxes of the fullerane bands with our 2σ upper limits, we conclude that, if fulleranes are present in both objects, then they seem to be much less abundant than isolated fullerene molecules. In fact, we cannot discard the presence of fulleranes with low levels of hydrogenation (e.g., $C_{60}H_2$ or $C_{60}H_4$). Moreover, our non-detection of fulleranes in two fullerene PNe, together with their possible detection (if real) in the fullerene proto-PN IRAS 01005+7910, suggests that these fullerene-related species may be formed in the short transition phase AGB−PN, but they are rapidly destroyed; e.g., by the quick increase of UV radiation from the central star towards the PN stage.

5.3 Mid-IR imaging of the fullerene planetary nebula IC 418

We have reported, for the first time, high spatial resolution narrow-band mid-IR GTC/CanariCam images of the fullerene-containing PN IC 418. These images cover the fullerene-like band at 17.4 μm, the PAH-like feature at 11.3 μm, and the broad 9-13 μm aliphatic-like feature, as well as their adjacent continua. Our main goal was to get some observational constraints on the formation process of fullerenes in the H-rich circumstellar environments around PNe by studying the relative spatial distribution of these complex species.

We detect a ring-like extended structure at all IR wavelengths (at a distance of ∼6300 AU from the central star at the IC 418's distance of 1.26 kpc). The dust continuum emission at 9.8 μm, on the contrary, seems to peak much closer to the central star. The spatial distributions of the emission in the Q1 and Q4 filters (C_{60} at 17.4 μm and the dust continuum at 20.5 μm, respectively) are very similar, which means that both wavelengths are probably dominated by the dust continuum emission (as also indicated by the very low IC 418 C_{60}-to-continuum ratio).

With respect to the dust continuum contribution, we have subtracted it by making use of synthetic photometry (i.e., through all Canaricam filters from the *ISO* spectrum). The resulting images show a clear ring-like extended emission structure for the broad 9-13 μm carrier. This indicates that the dust grains emitting at 20.5 μm are co-spatial with the carrier of the 9-13 μm emission feature. The situation is different for the PAH- and fullerene-like emissions at 11.3 and 17.4 μm, respectively, which have very weak residuals (at $\sim 4-5\sigma$ from the mean background level). The 11.3 μm PAH-like emission seems to follow the structure seen at other wavelengths, while the 17.4 μm C_{60}-like emission is mainly located at the northeast, extending from the central star to the outer regions of the nebula.

Regarding the fullerene formation process in PNe, these results might have several interpretations. The most exciting interpretation is, perhaps, that other fullerene-related species may contribute to the observed 17.4 μm emission. Hydrogenated fullerenes with very low H-content may be the possible contaminants, which could also explain the present inconsistency between the fullerene-like IR band ratios observed in PNe and the predictions of thermal/fluorescence excitation models.

6

Future work

As a natural extension of the work presented in this thesis, new research directions have emerged. Some of them are enumerated below.

Regarding the analysis of diffuse bands (both interstellar and circumstellar) in C_{60}-PNe, it will be very useful to obtain high-resolution, high S/N optical spectra of additional fullerene-containing PNe; especially for fullerene PNe with high radial velocities where circumstellar (nebular) absorptions (e.g., in the Na I D lines) have already been detected. This will permit us to search for more diffuse bands of circumstellar origin around PNe, and thus confirm/discard our possible detection of two diffuse circumstellar bands (DCBs) at 4428 and 5780 Å around PN Tc 1. With the recent identification of C_{60}^+ as a DIB carrier, we now know that there is a firm connection between C_{60} (and related species) and the DIB phenomenon. More laboratory and theoretical studies of fullerene-based molecular nanostructures may provide more DIB's identifications, helping to solve the long-standing astronomical mistery of the DIB's carriers.

The non-detection of fulleranes with high H-content in evolved fullerene-containing PNe together with the (tentative) fulleranes detection in the proto-PN IRAS 01005+7910 indicate that the proto-PN phase may provide the right conditions for the formation and detection of fulleranes in space. In this context, high-resolution and high-quality 3-5 μm spectra on a larger sample of Galactic proto-PNe (e.g., spectroscopic twins of IRAS 01005+7910) would be desirable. This can be easily done (at least for the brightest sources) with the

airborne IR observatory SOFIA, which permits high-resolution (R∼1300) 3-5 μm spectroscopy. Such observations could provide the first firm detection of highly hydrogenated fullerenes in space.

Finally, the upcoming James Webb Space Telescope (JWST; planned to launch in October 2018) will permit us to carry out key observational tests of the top-down fullerene formation models and new astronomical searches of fullerene-based species. The JWST, working from the near- to the mid-IR (∼0.6-28 μm), will be 50 times more sensitive than Spitzer (1000 times more sensitive than any ground-based mid-IR instrument on 10m-class telescopes) and it will improve the spectral and spatial resolution at mid-IR wavelengths by an order of magnitude with respect to Spitzer. For example, sub-arcsecond near- and mid-IR imaging, combined with spatially resolved spectroscopic observations, of the brighter and extended (>10") fullerene sources (Tc 1 and IC 418) will give us essential information to know if fullerenes are a photo-product of the UIR carriers (i.e., fullerenes are closer to the central star than UIR emitters) or if the fullerenes are attached to dust grains or well mixed with the UIR carriers (i.e., fullerenes are co-spatial with the UIR emitters). Indeed, the high JWST spectral resolution (>2000) may permit us to cleanly resolve the C_{60} (and C_{70}) IR bands from other potential contaminants (e.g., fulleranes with low H-content).

Bibliography

Abell, G. O., & Goldreich, P. 1966, PASP, 78, 232

Alata, I., Cruz-Diaz, G. A., Muñoz Caro, G. M., & Dartois, E. 2014, A&A, 569, A119

Allamandola, L. J., Tielens, A. G. G. M., & Barker, J. R. 1985, ApJ, 290, L25

Amari, S., Anders, A., Virag, A., & Zinner, E. 1990, Nature, 345, 238

Ballester, P., Modigliani, A., Boitquin, O., et al. 2000, The Messenger, 101, 31

Bauschlicher, Jr., C. W., Boersma, C., Ricca, A., et al. 2010, ApJS, 189, 341

Beaulieu, S. F., Dopita, M. A., & Freeman, K. C. 1999, ApJ, 515, 610

Bernard-Salas, J., Cami, J., Peeters, E., et al. 2012, ApJ, 757, 41

Bernard-Salas, J., Cami, J., Jones, A., et al. 2013, in Proceedings of The Life Cycle of Dust in the Universe: Observations, Theory, and Laboratory Experiments (LCDU2013). 18-22 November, 2013, 32

Berné, O., Montillaud, J., & Joblin, C. 2015, A&A, 577, A133

Berné, O., & Tielens, A. G. G. M. 2012, Proceedings of the National Academy of Science, 109, 401

Boersma, C., Bauschlicher, Jr., C. W., Ricca, A., et al. 2014, ApJS, 211, 8

Braga, M., Larsson, S., Rosen, A., & Volosov, A. 1991, A&A, 245, 232

Brieva, A. C., Gredel, R., Jäger, C., Huisken, F., & Henning, T. 2016, ApJ, 826, 122

Bussoletti, E., Colangeli, L., & Orofino, V. 1987, ApJ, 321, L87

Cami, J. 2014, in IAU Symposium, Vol. 297, The Diffuse Interstellar Bands, ed. J. Cami & N. L. J. Cox, 370–374

Cami, J., Bernard-Salas, J., Peeters, E., & Malek, S. E. 2010, Science, 329, 1180

Campbell, E. K., Holz, M., Gerlich, D., & Maier, J. P. 2015, Nature, 523, 322

Campbell, E. K., Holz, M., Maier, J. P., et al. 2016, ApJ, 822, 17

Castellanos, P., Berné, O., Sheffer, Y., Wolfire, M. G., & Tielens, A. G. G. M. 2014, ApJ, 794, 83

Cataldo, F. 2005, Astrobiology: Future Perspectives, 97

Cataldo, F., García-Hernández, D. A., & Manchado, A. 2014, European Chemical Bulletin, 3, 740

—. 2015, Fullerene Nanotubes and Carbon Nanostructures, 23, 818

Cataldo, F., & Iglesias-Groth, S. 2009, MNRAS, 400, 291

Chiar, J. E., Tielens, A. G. G. M., Whittet, D. C. B., et al. 2000, ApJ, 537, 749

Cox, N., Ehrenfreund, P., Kaper, L., Spaans, M., & Foing, B. 2005, in IAU Symposium, Vol. 235, IAU Symposium, 267

Cox, N. L. J. 2011, in EAS Publications Series, Vol. 46, EAS Publications Series, ed. C. Joblin & A. G. G. M. Tielens, 349–354

Cox, N. L. J. 2015, ArXiv e-prints, arXiv:1504.03281

Cox, N. L. J., & Cami, J. 2014, in IAU Symposium, Vol. 297, The Diffuse Interstellar Bands, ed. J. Cami & N. L. J. Cox, 412–415

Cox, N. L. J., & Cordiner, M. A. 2008, in IAU Symposium, Vol. 251, Organic Matter in Space, ed. S. Kwok & S. Sanford, 237–240

Crawford, M. K., Tielens, A. G. G. M., & Allamandola, L. J. 1985, ApJ, 293, L45

Curtis, H. D. 1918, Publications of Lick Observatory, 13, 55

Cutri et al., R. M. 2012, VizieR Online Data Catalog, 2311

—. 2013, VizieR Online Data Catalog, 2328

de Bruijne, J. H. J., & Eilers, A.-C. 2012, A&A, 546, A61

de Vries, M. S., Reihs, K., Wendt, H. R., et al. 1993, Geochim. Cosmochim. Acta, 57, 933

Delgado Mena, E., Bertrán de Lis, S., Adibekyan, V. Z., et al. 2015, A&A, 576, A69

Dinerstein, H. L., Sneden, C., & Uglum, J. 1995, ApJ, 447, 262

D'Odorico, S., Cristiani, S., Dekker, H., et al. 2000, in Proc. SPIE, Vol. 4005, Discoveries and Research Prospects from 8- to 10-Meter-Class Telescopes, ed. J. Bergeron, 121–130

Duley, W. W., & Hu, A. 2012, ApJ, 745, L11

Duley, W. W., & Williams, D. A. 1981, MNRAS, 196, 269

—. 2011, ApJ, 737, L44

Dunk, P. W., Adjizian, J.-J., Kaiser, N. K., et al. 2013, Proceedings of the National Academy of Science, 110, 18081

Ehrenfreund, P., & Foing, B. H. 2010, Science, 329, 1159

Foing, B. H., & Ehrenfreund, P. 1994, Nature, 369, 296

Frew, D. J., Bojičić, I. S., & Parker, Q. A. 2013, MNRAS, 431, 2

Friedman, S. D., York, D. G., McCall, B. J., et al. 2011, ApJ, 727, 33

Gadallah, K. A. K., Mutschke, H., & Jäger, C. 2013, A&A, 554, A12

Galazutdinov, G. A., LoCurto, G., & Krełowski, J. 2008, ApJ, 682, 1076

García-Hernández, D. A., Cataldo, F., & Manchado, A. 2013, MNRAS, 434, 415

Garcia-Hernandez, D. A., Cataldo, F., & Manchado, A. 2016, Fullerene Nanotubes and Carbon Nanostructures, 24, 679

García-Hernández, D. A., & Díaz-Luis, J. J. 2013, A&A, 550, L6

García-Hernández, D. A., Kameswara Rao, N., & Lambert, D. L. 2011a, ApJ, 729, 126

—. 2012a, ApJ, 759, L21

García-Hernández, D. A., Manchado, A., García-Lario, P., et al. 2010, ApJ, 724, L39

García-Hernández, D. A., Villaver, E., García-Lario, P., et al. 2012b, ApJ, 760, 107

García-Hernández, D. A., Iglesias-Groth, S., Acosta-Pulido, J. A., et al. 2011b, ApJ, 737, L30

García-Lario, P., & Perea Calderón, J. V. 2003, in ESA Special Publication, Vol. 511, Exploiting the ISO Data Archive. Infrared Astronomy in the Internet Age, ed. C. Gry, S. Peschke, J. Matagne, P. Garcia-Lario, R. Lorente, & A. Salama, 97

Geballe, T. R., Najarro, F., Figer, D. F., Schlegelmilch, B. W., & de La Fuente, D. 2011, Nature, 479, 200

Gillett, F. C., Forrest, W. J., & Merrill, K. M. 1973, ApJ, 183, 87

Goeres, A., & Sedlmayr, E. 1992, A&A, 265, 216

González-Martín, O., Díaz-Santos, T., Rodríguez-Espinosa, J. M., et al. 2013, in Revista Mexicana de Astronomia y Astrofisica Conference Series, Vol. 42, Revista Mexicana de Astronomia y Astrofisica Conference Series, 118–118

Heger, M. L. 1922, Lick Observatory Bulletin, 10, 141

Helou, G., & Walker, D. W., eds. 1988, Infrared astronomical satellite (IRAS) catalogs and atlases. Volume 7: The small scale structure catalog, Vol. 7, 1–265

Herbig, G. H. 1993, ApJ, 407, 142

—. 2000, ApJ, 542, 334

Herwig, F. 2005, ARA&A, 43, 435

Hobbs, L. M., York, D. G., Snow, T. P., et al. 2008, ApJ, 680, 1256

Huang, W., & Gies, D. R. 2008, ApJ, 683, 1045

Iglesias Groth, S. 2004, Lecture Notes and Essays in Astrophysics, 1, 105

Iglesias-Groth, S. 2007, ApJ, 661, L167

Iglesias-Groth, S., Cataldo, F., & Manchado, A. 2011, MNRAS, 413, 213

Iglesias-Groth, S., & Esposito, M. 2013, ApJ, 776, L2

Iglesias-Groth, S., García-Hernández, D. A., Cataldo, F., & Manchado, A. 2012, MNRAS, 423, 2868

Ishihara, D., Onaka, T., Kataza, H., et al. 2010, A&A, 514, A1

Jäger, C., Huisken, F., Mutschke, H., Jansa, I. L., & Henning, T. 2009, ApJ, 696, 706

Jourdain de Muizon, M., D'Hendecourt, L. B., & Geballe, T. R. 1990, A&A, 227, 526

Kameswara-Rao, N., & Lambert, D. L. 1993, MNRAS, 263, L27

Kharchenko, N. V., Scholz, R.-D., Piskunov, A. E., Röser, S., & Schilbach, E. 2007, Astronomische Nachrichten, 328, 889

Kroto, H. W., Heath, J. R., Obrien, S. C., Curl, R. F., & Smalley, R. E. 1985, Nature, 318, 162

Kroto, H. W., & Jura, M. 1992, A&A, 263, 275

Kwok, S. 2000, Cambridge Astrophysics Series, 33

—. 2004, Nature, 430, 985

Kwok, S. 2013, in Proceedings of The Life Cycle of Dust in the Universe: Observations, Theory, and Laboratory Experiments (LCDU2013). 18-22 November, 2013, 31

—. 2016, A&A Rev., 24, 8

Kwok, S., Volk, K., & Bernath, P. 2001, ApJ, 554, L87

Kwok, S., Volk, K., & Hrivnak, B. J. 1999, A&A, 350, L35

Kwok, S., & Zhang, Y. 2011, Nature, 479, 80

Leach, S., Vervloet, M., Desprès, A., et al. 1992, Chemical Physics, 160, 451

Leger, A., & D'Hendecourt, L. 1985, A&A, 146, 81

Leger, A., & Puget, J. L. 1984, A&A, 137, L5

Lewis, R. S., Ming, T., Wacker, J. F., Anders, E., & Steel, E. 1987, Nature, 326, 160

Luna, R., Cox, N. L. J., Satorre, M. A., et al. 2008, A&A, 480, 133

Maier, J. P., Walker, G. A. H., Bohlender, D. A., et al. 2011, ApJ, 726, 41

Maltseva, E., Petrignani, A., Candian, A., et al. 2015, ApJ, 814, 23

Manchado, A. 2004, in Astronomical Society of the Pacific Conference Series, Vol. 313, Asymmetrical Planetary Nebulae III: Winds, Structure and the Thunderbird, ed. M. Meixner, J. H. Kastner, B. Balick, & N. Soker, 3

McKellar, A. 1940, PASP, 52, 187

McNabb, I. A., Fang, X., Liu, X.-W., Bastin, R. J., & Storey, P. J. 2013, MNRAS, 428, 3443

Meixner, M., Skinner, C. J., Keto, E., et al. 1996, A&A, 313, 234

Merrill, P. W., & Wilson, O. C. 1936, in Publications of the American Astronomical Society, Vol. 8, Publications of the American Astronomical Society, 249

Micelotta, E. R., Jones, A. P., Cami, J., et al. 2012, ApJ, 761, 35

Morisset, C., & Georgiev, L. 2009, A&A, 507, 1517

Morisset, C., Szczerba, R., Anibal García-Hernández, D., & García-Lario, P. 2012, in IAU Symposium, Vol. 283, IAU Symposium, 452–453

Novoselov, K. S., Geim, A. K., Morozov, S. V., et al. 2004, eprint arXiv:cond-mat/0410631, cond-mat/0410631

Otsuka, M., Kemper, F., Cami, J., Peeters, E., & Bernard-Salas, J. 2014, MNRAS, 437, 2577

Peeters, E., Hony, S., Van Kerckhoven, C., et al. 2002, A&A, 390, 1089

Petrie, R. M., & Pearce, J. A. 1961, Publications of the Dominion Astrophysical Observatory Victoria, 12, 1

Porceddu, I., Benvenuti, P., & Krelowski, J. 1991, A&A, 248, 188

Pottasch, S. R., Bernard-Salas, J., Beintema, D. A., & Feibelman, W. A. 2004, A&A, 423, 593

Pourbaix, D., Tokovinin, A. A., Batten, A. H., et al. 2004, A&A, 424, 727

Ramos-Larios, G., Vázquez, R., Guerrero, M. A., et al. 2012, MNRAS, 423, 3753

Russell, R. W., Soifer, B. T., & Merrill, K. M. 1977, ApJ, 213, 66

Sadjadi, S. 2017, private communication

Sadjadi, S., Zhang, Y., & Kwok, S. 2015, ApJ, 807, 95

Salama, F., Galazutdinov, G. A., Krełowski, J., Allamandola, L. J., & Musaev, F. A. 1999, ApJ, 526, 265

Sassara, A., Zerza, G., Chergui, M., & Leach, S. 2001, ApJS, 135, 263

Scarrott, S. M., Watkin, S., Miles, J. R., & Sarre, P. J. 1992, MNRAS, 255, 11P

Scott, A., Duley, W. W., & Pinho, G. P. 1997, ApJ, 489, L193

Seab, C. 1995, in Astrophysics and Space Science Library, Vol. 202, The Diffuse Interstellar Bands, ed. A. G. G. M. Tielens & T. P. Snow, 129

Sellgren, K. 1984, ApJ, 277, 623

Sellgren, K., Uchida, K. I., & Werner, M. W. 2007, ApJ, 659, 1338

Sellgren, K., Werner, M. W., Ingalls, J. G., et al. 2010, ApJ, 722, L54

Sharpee, B., Williams, R., Baldwin, J. A., & van Hoof, P. A. M. 2003, ApJS, 149, 157

Shklovskii, I. S. 1956, Kosmicheskoe radiolzluchenie.

Smith, E. C. D., & McLean, I. S. 2008, ApJ, 676, 408

Snow, T. P. 2014, in IAU Symposium, Vol. 297, The Diffuse Interstellar Bands, ed. J. Cami & N. L. J. Cox, 3–12

Snow, T. P., & Destree, J. D. 2011, in EAS Publications Series, Vol. 46, EAS Publications Series, ed. C. Joblin & A. G. G. M. Tielens, 341–347

Snow, T. P., & McCall, B. J. 2006, ARA&A, 44, 367

Snow, T. P., Zukowski, D., & Massey, P. 2002, ApJ, 578, 877

Soubiran, C., Jasniewicz, G., Chemin, L., et al. 2013, A&A, 552, A64

Sturm, E., Lutz, D., Tran, D., et al. 2000, A&A, 358, 481

Taylor, A. R., Gussie, G. T., & Goss, W. M. 1989, ApJ, 340, 932

Taylor, A. R., & Pottasch, S. R. 1987, A&A, 176, L5

Telesco, C. M., Ciardi, D., French, J., et al. 2003, in Proc. SPIE, Vol. 4841, Instrument Design and Performance for Optical/Infrared Ground-based Telescopes, ed. M. Iye & A. F. M. Moorwood, 913–922

Tielens, A. G. G. M. 2005, The Physics and Chemistry of the Interstellar Medium

—. 2008, ARA&A, 46, 289

Tielens, A. G. G. M. 2011, in EAS Publications Series, Vol. 46, EAS Publications Series, ed. C. Joblin & A. G. G. M. Tielens, 3–10

Tokunaga, A. T., Sellgren, K., Smith, R. G., et al. 1991, ApJ, 380, 452

Turner, B. E. 1971, ApJ, 163, L35

van der Zwet, G. P., & Allamandola, L. J. 1985, A&A, 146, 76

van Diedenhoven, B., Peeters, E., Van Kerckhoven, C., et al. 2004, ApJ, 611, 928

van Loon, J. T., Bailey, M., Tatton, B. L., et al. 2013, A&A, 550, A108

Walker, G. A. H., Bohlender, D. A., Maier, J. P., & Campbell, E. K. 2015, ApJ, 812, L8

Wang, W., & Liu, X.-W. 2007, MNRAS, 381, 669

Watson, J. K. G. 1994, ApJ, 437, 678

Wegner, W. 2003, Astronomische Nachrichten, 324, 219

Weisman, J. L., Lee, T. J., Salama, F., & Head-Gordon, M. 2003, ApJ, 587, 256

Williams, R., Jenkins, E. B., Baldwin, J. A., et al. 2008, ApJ, 677, 1100

Wilson, O. C. 1953, ApJ, 117, 264

Zhang, Y., & Kwok, S. 2011, ApJ, 730, 126

—. 2013, Earth, Planets, and Space, 65, 1069

Zhang, Y., Kwok, S., & Hrivnak, B. J. 2010, ApJ, 725, 990

Zhang, Y., Sadjadi, S., Hsia, C.-H., & Kwok, S. 2017, ArXiv e-prints, arXiv:1705.01807

Zhen, J., Castellanos, P., Paardekooper, D. M., Linnartz, H., & Tielens, A. G. G. M. 2014, ApJ, 797, L30